ON EMERGENT BEHAVIOUR DURING THE OSCILLATORY ELECTRODISSOLUTION OF SILICON

MAXIMILIAN PATZAUER

PHD THESIS

NONEQUILIBRIUM CHEMICAL PHYSICS – DEPARTMENT OF PHYSICS
TECHNICAL UNIVERSITY OF MUNICH

SUPERVISOR:
Prof. Dr. Katharina Krischer

Technische Universität München
Fakultät für Physik

ON EMERGENT BEHAVIOUR DURING THE OSCILLATORY ELECTRODISSOLUTION OF SILICON

MARKUS EMIL MAXIMILIAN PATZAUER

Vollständiger Abdruck der von der Fakultät für Physik der Technischen Universität München zur Erlangung des akademischen Grades eines

Doktors der Naturwissenschaften (Dr. rer. nat)

genehmigten Dissertation.

Vorsitzende: Prof. Dr. Karen Alim

Prüfende/-r der Dissertation:

1. Prof. Dr. Katharina Krischer

2. Prof. Dr. Carsten Beta

Die Dissertation wurde am 12.11.2021 bei der Technischen Universität München eingereicht und durch die Fakultät für Physik am 10.12.2022 angenommen.

"...a real scientific mystery is worth pursuing to the ends of the Earth for its own sake, independently of any obvious practical importance or intellectual glamour."

— Philip W. Anderson [4]

ABSTRACT

We investigate the multifaceted dynamics of the oscillatory electrodissolution of silicon in a fluoride-containing electrolyte under anodic potentials using spatially resolved *in situ* ellipsometric imaging.

The system is approached from two sides: on the one hand we study physicochemical properties of the system, specifically the dissolution valency and the role of the hole dynamics for pattern formation, and on the other hand we investigate the observed phenomena from a nonlinear dynamics perspective.

We show that a self-organised adaptive coupling emerges from the interplay of the hole dynamics and an external resistor. This constitutes an example where an adaptive coupling was observed in a nonliving system. Our experimental data shows that this coupling can lead to the transition from a uniform state to multifrequency clusters, i.e. clusters with different frequencies.

Furthermore, we provide experimental evidence that the system possesses inherent birhythmicity and thus at least two distinct feedback loops. We demonstrate several types of interaction between the coexisting limit cycles and find that an asymmetry in their sensitivities can lead to both intrinsic entrainment of the limit cycles in phase space and unidirectional coupling between two identical electrodes initialized on the different limit cycles. Due to the unidirectional coupling the electrodes adopt states of different complexity rendering them an experimental example of a smallest chimera state in a minimal network configuration.

ACKNOWLEDGEMENTS

As my predecessors before me, also I would like to thank Katharina Krischer for her inspiring creativity and nonpareil enthusiasm. Also, for her giving also me the opportunity to work in her group. The group without which, as in most endeavours, this thesis would not have emerged. Emerging is indeed a fitting term seeing as the work going into both the research and the resulting papers is not the fruit of one persons lone work but rather the synergetic outcome of cooperation, collaboration, and joint efforts.

As is often the case, it is hard to sort the importance of these exchanges but it would be remiss of me if I at this point did not mention the fruitful collaboration with Anton Tosolini and with Juliane Wiehl who have been integral to this project, both as master's students and later as fellow PhD students. Not to mention all the conversations we have had about things both more and less important than science.

On that note, I would also like to specifically thank Felix Kemeth, Munir Salman, and Sindre Haugland for providing support both as scientists and as friends. Felix for his immense patience when explaining and his contagious motivation. Munir for the fruitful scientific cooperation and the moral support, especially during the writing phase. Sindre for his sense of style and the many fun discussions both as office colleagues and, especially, as neighbours during the later part of this thesis project.

Likewise, I would like to express my sincerest gratitude to Konrad Schönleber for introducing me to the fascinating world of experimental nonlinear dynamics. His encouraging curiosity was after all what lead me down the path resulting in this thesis.

My thanks go out to all current and former group members, especially André Dourado, Daniel Heger, Seungjae Lee, Thomas Maier, Siegfried Schreier, and Werner Schindler, for the wonderful working environment. Also, a special thanks to Simon Filser and Qi Li for, besides the open and welcoming atmosphere, also providing experimental support during my early days in the group.

Not only I but all who are interested in the completion of this text should be thankful to Johan Sahlström, for without him I would still be writing the initial chapter.

I would also like to thank Martin Björnmalm without whom it would not have been possible to complete the undergraduate years.

To my wonderful siblings, especially my sister Rebecka, thank you for keeping me sane and providing me with perspective.

I am in an infinite debt to my parents for their complete and total support throughout.

Lastly, thank you Karolina for all the joy and happiness, for your patience, and for your unconditional support.

Thank you all.

CONTENTS

APPENDIX

ACRONYMS

1

INTRODUCTION

The world is full of complex and nonlinear phenomena [45, 111, 136, 137]. Many of these arise in complicated and involved systems that are inherently hard to experiment on. Thankfully, a great number of this kind of phenomena can be captured in simpler tabletop experiments and mathematical models. The reason this works is that the underlying dynamical principle can be the same in the original, more involved system as in the tabletop experiment.

Take for example the simultaneous flashing of fireflies on the riverbanks of Borneo [21], the tidal locking of moons to planets [97], the peculiar behaviour of how occasionally people can end up walking in step when crossing a bridge [138] or how we sometimes, all of a sudden, start to applaud in unison. All these behaviours can in a sense be captured by an experiment consisting of metronomes on a freely moving board [13, 104] or theoretically in the Kuramoto model of coupled oscillators [64, 135]. The underlying principle here being synchrony.

Another general principle is found in the dynamics of populations. It is inherently hard to experiment on a population in the wild but a simple experiments in a lab with for example bacteria or yeast in a Petri dish [59] can tell us surprisingly much about the original system. Even the perhaps simplest difference equation, the logistic equation, can further our understanding of how populations change with time [82, 83]. Here, we are relying on the generality of standard bifurcations such as the period doubling bifurcation or the Hopf bifurcation to name but a few.

Another example of the essence of complex dynamics being modelled by a simple tabletop experiment is when the sometimes erratic behaviour of the weather or of turbulent fluids is captured by a so-called Malkus–Lorenz waterwheel [77]. This construction is inspired by the simplified theoretical model of atmospheric convection rolls known as the Lorenz model [76] and gives rise to chaotic dynamics that lives on the Lorenz attractor with its characteristic butterfly shape. Here, the underlying principle is deterministic chaos and the related bifurcation sequences leading to it.

In this thesis we will continue in the tradition of tabletop experiments with robust and reproducible dynamics and their use in our

pursuit to broaden our understanding of complex universal phenomena through the study of specific, simpler systems.

We should of course be wary when reducing the world to simple equations and experiments and be aware that there is a limit to the extent to which they describe the original phenomena—the map is not the territory. However, nor is the territory the map for then it would be a rather useless map. A useful map, or in our case tabletop experiment, would be an experiment that is practical in its implementation and can result in universal dynamics that can be observed outside of the laboratory as well. Such an experiment has the twofold benefit that it enables us not only to understand general phenomena but also to anchor theoretical models in the real and complex world around us.

One such experiment that meets our requirements is the one mentioned in the title of this thesis: the electrodissolution of silicon in a fluoride containing electrolyte under anodic potentials. This system is known to exhibit a multitude of dynamical phenomena. It can, for example, oscillate uniformly in a self-sustained state, both periodically and chaotically, and can even exhibit different types of spatial patterns such as subclustering, turbulence, and so-called chimeras. We will embark on an explorative study of this system and extend this library of dynamical phenomena. We will present self-organised multifrequency patterns that arise due to what we identify to be a nonlinear, nonlocal coupling, and also show that the system has bistable oscillatory states. In relation to the bistability we discuss, among other things, both intrinsic entrainment, and minimal chimera states. We will interpret our findings and discuss them in the context of the pre-existing results which mainly revolved around coexistence patterns, the most prominent of which being the chimera state.

In the following sections we will give a short overview of some of the main phenomena that we will discuss in the rest of the thesis.

1.1 CHIMERAS

The chimera state, a state emerging from identical oscillators splitting into two domains, a coherent one and a desynchronised one [1], is typically said to have been reported for the first time in 2002 [65]. It received its name in 2004 [1] and just as its namesake, the mythical fire breathing Greek monster, its main feature is the coexistence of incongruous parts. This curious coexistence of chaos and order is in a sense the link connecting the two apparent opposites [100].

As with a lot of fundamental research, chimera states initially received most of its attention due to this fascinating and intriguing double nature. Early findings regarding chimeras were mainly theoretical [14, 99, 103, 126], but subsequently chimeras were also linked to real world phenomena. Most notably they have been discussed in connection with ventricular fibrillation related to sudden cardiac arrest

[103], neural activity in the brain [145], specifically regarding epileptic seizure [117], and in the context of electrical grids [92]. A theoretical study of interacting social agents have even linked chimeras to the behaviour of social systems [39].

There are also a few laboratory experiments that have been shown to exhibit chimera states but these remain rare. The first of these were experiments involving a version of the Belousov-Zhabotinsky reaction where the oscillators were photosensitive [96, 131, 144] and experiments with optical oscillators [44]. Chimeras were also found in a system of coupled metronomes [79, 155], in optoelectronic networks [46], and there are experiments with networked oscillatory chemical processes on metal electrodes that exhibit chimeras as well [150, 151]. However, so far the only truly self-organised chimera in an experiment was found during the above mentioned silicon electrodissolution [124, 125, 130]. Truly self-organised is here taken to mean that the system arranges itself spontaneously without any externally controlled feedback. Nothing is imposed onto the system to induce a splitting but instead, for a range of given uniform external parameters, the chimera state emerges from the intrinsic dynamics.

1.2 BISTABILITY

As mentioned above, the electrodissolution of silicon proceeds in an oscillatory fashion for certain parameters. This, more fundamental phenomenon, has been known since the late 1950s [148]. More recently, indications have been found that point to the fact that there is not only one possible type of oscillatory behaviour. Schönleber et al. presented three main types: sinusoidal low amplitude oscillations, chaotic oscillations, and relaxational high amplitude oscillations, and identified two main feedback loops [128]. Later, before the work on this thesis, we reported in Ref. [147] that the chaotic oscillations can be further distinguished into chaotic oscillations emerging from so-called low amplitude oscillations via a quasiperiodic scenario and chaotic oscillations emerging from another type of oscillations, referred to as high amplitude oscillations, via a period doubling scenario. These findings further supported the existence of two different feedback loops and indicate that there exists a bistability in the system.

Generally speaking, bistability is both an interesting and a common phenomenon in dynamical systems [112]. The most common type of bistability is the coexistence of two stable stationary states. However, its meaning is more general and includes the coexistence of any two attractors in phase space, such as of a stationary state and a limit cycle, of two limit cycles, and so on. Even bichaoticity, as found in Ref. [147], the coexistence of two chaotic attractors, can occur.

The discovery of birhythmicity in physical systems dates back to at least 1976, when it was reported to exist in a model of a continuous

stirred tank reactor with consecutive exothermic reactions [29]. To our knowledge, the first experimental finding of birhythmicity, then called generalised multistability by the authors, was reported in 1982 in a Q-switched gas laser [6]. Later that year, Decroly and Goldbeter introduced the term birhythmicity in their theoretical study of a sequence of enzymatic reactions in a system with two positive feedback loops in series [31]. This was one of the first attempts to characterise birhythmicity in more detail. Their approach was later used in an experimental study in which two chemical oscillators with a common intermediate were combined and the resulting system was found to exhibit birhythmicity [2, 3]. Other examples of experimental chemical systems exhibiting birhythmicity include electronic oscillators [17], the Belousov–Zhabotinsky reaction in a stirred flow reactor [66, 80, 118], acetaldehyde oxidation in a continuously stirred tank reactor [40] and the gas-phase H_2+O_2 reaction in a continuously stirred tank reactor [12, 51]. Furthermore, birhythmicity proved to be important in diverse biological contexts, most notably neural activities, where examples for experimental evidences can be found e.g. in Ref. [48, 50, 67], or circadian oscillators, where an experimental demonstration is reported in Ref. [109]. More recently, an experimental electrochemical example of birhythmicity has been found in the oscillatory electrodissolution of Cu when using a delay feedback [94].

Compared to the relatively small number of experimental studies, the number of theoretical investigations on birhythmicity is much larger (see e.g. references in Ref. [112]). Besides models of ordinary differential equations describing specific systems, also generic properties of spatially extended birhythmic systems or coupled birhythmic oscillators have been studied with normal form type equations. These include wave phenomena in spatially extended reaction-diffusion models and ensembles of coupled birhythmic (phase) oscillators [8, 11, 18, 114, 133, 134, 156, 157]. The latter were also found to promote the occurrence of chimera states, an interesting prediction which awaits experimental validation.

In Chapter 5 we will present evidence of a direct bistability between the two oscillation types found in the Si-system. What then sets the Si-system apart from the above mentioned experiments is that the initial conditions can be easily controlled, both in time and space, allowing us to set each location—or coupled electrode—in the chosen oscillation type. This property will help us to not only show explicit birhythmicity but also allow us to investigate the qualitative differences between the two oscillation types and exploit the different sensitivity towards specific perturbations in order to find chimera states in a minimal system consisting of only two electrodes.

1.3 COUPLING

With that said, there is not yet a mechanistic model explaining the silicon electrodissolution. Especially the oscillatory behaviour and why it arises has been the subject of intense research (see Ref. [160] for an overview until 2003). Attempts have been made to answer these questions by focusing on the more fundamental behaviour of the system, trying to understand how the current voltage characteristics comes about [22, 24, 25, 27]. But even here there are still open questions, e.g. how does the characteristic Negative Differential Resistance (NDR) emerge? Alas, we do not have a satisfactory explanation as for why the system oscillates, not to mention an explanation for the spatiotemporal patterns such as the chimera state.

However, a mathematical model inspired by the findings during the electrodissolution of silicon was developed in order to capture chimeras in a spatially extended oscillatory media. The model is a modification of the Complex Ginzburg-Landau Equation (CGLE) [62, 63]:

$$\partial_t W = W + (1 + ic_1)\,\nabla^2 W - (1 + ic_2)\,|W|^2 W\,. \tag{1.1}$$

Here, $W(\mathbf{r}, t)$ is a complex valued oscillator describing the dynamical state at each point $\mathbf{r}$ at the time t, and c_1 and c_2 are real-valued parameters. The CGLE is a general description of all reaction-diffusion systems in the vicinity of a Hopf bifurcation. It thus provides the appropriate normal form since the oscillations in the Si-system have been shown to arise from just such a bifurcation [88, 129]. The main motivation for modifying the CGLE was to reproduce the fact that for the early findings of patterns in the Si-system the spatially average signal oscillated nearly harmonically. This was not only the case for the two-phase clusters that were found first [87] but also for the chimera states [124, 125, 130]. Generally, the CGLE does not produce dynamics where the homogeneous mode is preserved. Hence, in order to reproduce the experimental findings a global coupling was added to the diffusion in the CGLE and the so-called Modified Complex Ginzburg-Landau Equation (MCGLE) [125] was proposed:

$$\begin{aligned}\partial_t W = {} & W + (1 + ic_1)\,\nabla^2 W - (1 + ic_2)\,|W|^2 W \\ & - (1 + i\nu)\,\langle W\rangle + (1 + ic_2)\,\langle |W|^2 W\rangle\,.\end{aligned} \tag{1.2}$$

Again, $W(\mathbf{r}, t)$ is a complex valued oscillator describing the dynamical state at each point $\mathbf{r}$ at the time t. c_1, c_2, and ν are real-valued parameters and $\langle \ldots \rangle$ denotes the spatial average. This specific global coupling results in conserved harmonic oscillations of the uniform mode, or equivalently, of the spatial average. This can be seen when taking the spatial average of Eq. (1.2) which results in the spatial average of the MCGLE simply being given by $\partial_t \langle W\rangle = -i\nu\langle W\rangle$ which has the solution $\langle W\rangle = \eta e^{-i\nu t}$ for some amplitude η, i.e. a harmonic

oscillation. The global coupling terms are composed of a linear part and a nonlinear part and theoretical studies have even show that the nonlinear part is decisive for the formation of this type of chimera in ensembles of discrete individual oscillators, i.e. ensembles of Stuart-Landau oscillators [125]. The addition of the nonlinear global coupling term revealed a new route to chimera states where the synchronous oscillation is unstable.

Having recognised this, the next challenge was to identify the physical processes in the experiment related to the different coupling terms in the MCGLE. First considerations in this direction have suggested that the linear and nonlinear parts of the global coupling actually have two physically independent origins: oscillations were thought to only occur when an ohmic resistor was placed in series to the Si electrode [26]. Such an external resistor acts as a global linear coupling by linking the potential drop across the electrode φ_{el}, to the total current I. Any change in the local current changes the total current which in turn changes the potential drop across the resistor and thus the potential drop across the electrode:

$$U_{app} = \varphi_{el} + R_{ext} I \tag{1.3}$$

where U_{app} is the applied voltage and R_{ext} is the resistance of the external resistor in series with the electrode. The linear global coupling was thus identified as emerging from the external resistor.

The nonlinear global coupling term in Eq.(1.2) has been linked to the behaviour under reduced illumination. The oxidation of silicon requires at least one valence band hole and hence n-doped silicon has to be illuminated for the oxidation to take place [84]. If the illumination intensity is high enough, there will always be a sufficient amount of holes available and the behaviour will be identical to the one of p-doped silicon in the dark [105]. However, if the illumination intensity is lowered and the generation rate of holes decreases, the number of available holes also decrease and starts to determine the reaction rate. The lower illumination leads to a limited current during part of the oscillation, yielding a plateau in the current. This limitation of the current is nonlinear and has global characteristics since it acts on the total current. Thus, it has been connected to the nonlinear global coupling in the MCGLE. It was shown that oscillations could be stabilised under these conditions even without the presence of an external resistor [125]. It is also at these lower illuminations and with no, or a small external resistance that patterns are observed, inter alia, the chimera states [88, 124, 125, 130]. This finding matches the prediction that the nonlinear global coupling in the MCGLE can be decisive for the formation of chimeras and thus corroborates the fact that this is the searched for nonlinear global coupling. However, it should be noted that although there are similarities between the coupling introduced in the experiment and the one in the MCGLE, it is

still unclear under which experimental conditions it is a good approximation. In particular, the assumption that the nonlinear coupling is truly global seems to be questionable in some parameter ranges. Is the nature of the nonlinear coupling in the experiment truly global or does the diffusion dynamics of the holes leading to a nonlocal coupling also play a role in the formation of the patterns?

1.4 OUTLINE

We start this thesis by tackling questions specific to the Si-system in order to establish a solid background for the following chapters where the dynamics is investigated in more detail.

In particular, we start by looking at the physicochemical properties of the system without an external coupling.

First, we confirm that the characteristic part of the voltage scans that show a NDR is a steady state and not an effect of the finite scan rate. Knowing that the system is stable at these parameters helped us to develop the model presented in Ref. [120]. This model aims to explain, among other features, the NDR behaviour and is based on the idea that the etch rate depends on the degree of oxidation. As a consequence of this assumption, the model predicts that the valency increases with increasing potential along the NDR-branch. We are here able to confirm experimentally that the degree of oxidation, or the dissolution valency, does indeed increase.

Second, at slightly higher potentials, we find that there is a potential window in which the most fundamental behaviour of the system is to oscillate, even if there is no external coupling. Having established that these oscillations are stable then allows us to investigate how lowering the illumination changes the spatial dynamics without having to cut off the current or introduce an external resistor.

Upon this groundwork, we investigate the dynamics in the later chapters.

The chapters are structured as follows:

We first take a closer look at the experimental set-up in Chapter 2, focusing on the three main parts of the set-up, i.e. the electrochemical set-up, the ellipsometric imaging system, and the illumination set-up. In addition an overview of the data analysis tools that we most commonly use is given and the measurement protocol for determining the etch depth is presented.

In Chapter 3 we investigate system specific properties of the Si-system and thus contribute to the understanding of the underlying physicochemical mechanism of the electrodissolution of silicon. We first present measurements regarding the steady state and the dissol-

ution valency before presenting the stable self-sustained oscillations. Then, we present and discuss data showing the effects that reducing the illumination intensity has on these oscillations.

In Chapter 4 we study the emergence of self-organised multifrequency clusters due to what we show to be an adaptive coupling, and how these states are related to chimeras.

In Chapter 5 we present experimental evidence that the electrodissolution of silicon exhibits birhythmicity. Both the interaction between the oscillation types in phase space, giving rise to an intrinsic entrainment, and the interaction in real space, yielding a smallest chimera, are discussed in detail.

Lastly, Chapter 6 contains a summary of the main findings and concluding remarks.

2

THE EXPERIMENTAL SYSTEM AND SET-UP

The main experiment in this thesis is the electrochemical dissolution of silicon in a fluoride containing electrolyte under constant anodic potentials. This is a type of corrosion experiment where we simultaneously create oxide electrochemically and etch it chemically.

In this chapter we will take a closer look at the general experimental set-up used to investigate this process. We will start with the electrochemical set-up and then look closer at the ellipsometric imaging set-up used to monitor lateral uniformity of the electrode/electrolyte interface *in-situ*. Next, we discuss the data evaluation, specifically the spatially resolved ellipsometric data, before describing the laser illumination needed for generating holes needed for experiments using n-doped silicon. Specific details regarding measurement protocols can be found in connection to the respective results in later chapters.

The experimental design and the custom build instrumentation was inherited from Iljana Miethe who designed and set up the first version of the experiment during her PhD thesis [86] (also described in Ref. [88]). Later Konrad Schönleber adjusted it slightly during his PhD thesis [127], see also Ref. [128, 130]. During the cause of the work for this thesis several optical parts have been replaced and/or upgraded, notably the set-up is now located on an optical table for enhanced reproducibility of the illumination and a Spatial Light Modulator (SLM) has been added allowing us to control the spatial intensity distribution of the laser light on the electrode. These main modifications were made in collaboration with Anton Tosolini. He and Yukiteru Murakami are the unsung heroes behind getting the SLM up and running. The new sample holder with two separate electrodes was designed together with Juliane Wiehl and built by Thomas Gänsheimer. The data acquisition software was inherited from Andreas Heinrich who wrote it during his Master's thesis [47].

2.1 ELECTROCHEMICAL SYSTEM

As mentioned above the electrodissolution of silicon in fluoride containing electrolyte under anodic potentials consists of two main processes: electrochemical oxidation of silicon and chemical etching of

silicon oxide. The oxidation can proceed either through a divalent, Eq. (2.1), or a tetravalent, Eq. (2.2), oxidation process [84, 148, 149]:

$$\begin{aligned} \mathrm{Si} + 2\mathrm{H_2O} + \kappa_{\mathrm{VB}} h^+ &\rightarrow \mathrm{Si(OH)_2} + 2\mathrm{H}^+ + (2 - \kappa_{\mathrm{VB}}) e^- \\ \mathrm{Si(OH)_2} &\rightarrow \mathrm{SiO_2} + \mathrm{H_2}, \end{aligned} \tag{2.1}$$

$$\mathrm{Si} + 2\mathrm{H_2O} + \kappa_{\mathrm{VB}} h^+ \rightarrow \mathrm{SiO_2} + 4\mathrm{H}^+ + (4 - \kappa_{\mathrm{VB}}) e^- \tag{2.2}$$

Here κ_{VB} denotes the number of charge carriers that come from the valence band of the silicon. Note that the first step in reaction (2.1) is electrochemical and the second step is purely chemical.

The chemical etching of the silicon oxide electrolyte can proceed through the following three reactions [22]:

$$\mathrm{SiO_2} + 6\mathrm{HF} \rightarrow \mathrm{SiF_6^{2-}} + 2\mathrm{H_2O} + 2\mathrm{H}^+ , \tag{2.3}$$

$$\mathrm{SiO_2} + 3\mathrm{HF_2^-} + \mathrm{H}^+ \rightarrow \mathrm{SiF_6^{2-}} + 2\mathrm{H_2O} , \tag{2.4}$$

$$\mathrm{SiO_2} + 2\mathrm{HF} + 2\mathrm{HF_2^-} \rightarrow \mathrm{SiF_6^{2-}} + 2\mathrm{H_2O}. \tag{2.5}$$

The total etch rate of the electrolyte depends on the fluoride concentration as well as the type of fluoride species at hand [52]. The type of species, in turn, depends on the pH value [132]and if we use the model presented in Ref. [22] we find that in our electrolyte reaction (2.3) is dominating while reaction (2.4) and (2.5) only come into play for higher pH values.

2.2 ELECTROCHEMICAL SET-UP

We investigated the interaction between the oxidation and the etching in a standard electrochemical three-electrode set-up with the silicon sample as the Working Electrode (WE). We used either n-doped (1-10 Ωcm) or p-doped (5-25 Ωcm) single crystalline (111) silicon. Before the experiments, the silicon sample was equipped with an ohmic back contact. To do this we first cleaned the sample by sequentially immersing it in acetone, isopropanol, and ultrapure water (18.2 MΩcm) for 5 min each in an ultrasonic bath, blowing it dry with with argon in-between the steps. Next, we dropped a buffered 1 : 6 $\mathrm{HF}(40\,\%) : \mathrm{NH_4F}(40\,\%)$ solution on the back of the electrode until the surface becomes H-terminated. The H-termination can be seen by the fact that the surface becomes hydrophobic and the HF-solution forms a droplet. Second, we thermally evaporated approx. 200 nm aluminium onto the back of the electrode. It was then annealed in a low pressure annealing oven ($5{\cdot}10^{-5}$ bar) at 250° C for 15 min in the case of n-doped samples and at 400° C for 30 min in the case of p-doped samples. The back contact ensures that the potential distribution in the bulk of the electrode is spatially uniform. For p-doped silicon this is accomplished

by the aluminium diffusing into the silicon. This results in a gradually increasing doping level towards the contact and hence a barrier free connection between the metal and the semiconductor. For n-doped silicon on the other hand the barrier is already comparably small and the annealing mainly serves the purpose of increasing the area of the interface.

Once the electrode had been equipped with a back contact the front side of the electrode was treated with an oxygen plasma in order to rid it of any organic contamination and to realise a defined, initial surface oxide. Next, the sample was mounted on a custom-made sample holder made out of polytetrafluorethylen (PTFE). The sample was mounted using a conductive silver paste and sealed using red silicone rubber (Scrintex 901, Ralicks GmbH); 10 - 20 mm^2 of the Si sample were left exposed, forming the active area of the WE. The exposed electrode area was determined using an optical microscope with a precision of approx. 0.1 mm^2. The active area was cleaned by wiping the electrode with acetone-drenched precision wipes and sequentially immersing it in acetone, ethanol, methanol, and ultrapure water (18.2 MΩcm) for 10 min each.

The mounted electrode was then placed in the centre of the cell with the $Hg|Hg_2SO_4$ reference electrode placed behind it. For the counter electrode, we bent a Pt wire (99.99 % Chempur) into a circular shape and placed it symmetrically in front of the WE.

In order to control the voltage between working and reference electrode, we used a FHI-2740 potentiostat (electronics laboratory of the Fritz-Haber-Institut, Berlin, Germany) or a Biologic SP-200, depending on the experimental requirements. Generally, the FHI potentiostat was used when the potential had to be changed manually during the experiment and the SP-200 whenever we performed slow potential scans. In addition to the applied potential the illumination intensity and an adjustable ohmic resistance placed in series with the WE were used as control parameters. For measurements with two electrodes, cf. Chapter 5.4, a new sample holder was constructed with two electrically separated wires. This allowed us to connect the two electrodes separately to the two respective wires and then short-circuit the wires at the external resistance.

The aqueous electrolyte used throughout this thesis contained 0.06 M NH_4F and 142 mM H_2SO_4, yielding a pH of 1 in accordance with the dissociation constants found in Ref. [22]. We have calculated the amount of H_2SO_4 necessary to attain a pH of 1 and a fluoride concentration of 0.06 M instead of measuring it since most pH-meters are made of glass and are hence damaged by our fluoride containing solution.

The electrolyte was purged with argon for 30 min before the experiment and an argon overpressure was kept throughout all measurements via a gas inlet above the electrolyte. The electrolyte was stirred

using a magnetic stirrer at 1200 RPM throughout all measurements and had a total volume of 500 ml.

All glassware was cleaned in HNO_3 and subsequently in a 1 M aqueous KOH solution and stored in ultrapure water. Platinum and PTFE parts were cleaned in Piranha solution. All organic cleaning solvents were AnalaR NORMAPUR grade (VWR Chemicals). All electrolyte components were Suprapur grade (Merck).

2.3 ELLIPSOMETRIC IMAGING

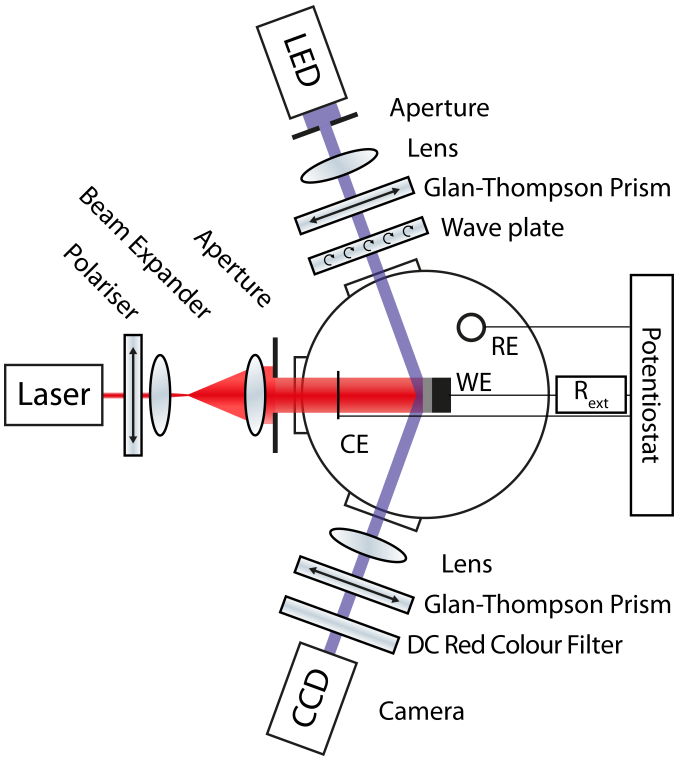

Figure 2.1: Sketch of the three electrode electrochemical cell showing the position of the WE, the reference electrode (RE), and the counter electrode (CE) as well the electrical control and the external resistance R_{ext}. Also shown are the ellipsometric imaging set-up and the laser illumination set-up for uniformly illuminated electrodes. The spatially resolved ellipsometric imaging allows us to monitor the electrode surface *in situ*. The light from the LED (blue) is first elliptically polarised and then reflected off the WE, resulting in a change in polarisation, depending on the optical path length through the oxide. Relative changes in polarisation are then converted into an intensity signal which is recorded by the CCD camera. The intensity of the laser-light used for illumination of the WE can be controlled with the polariser.

We used the ellipsometric imaging set-up sketched in Fig. 2.1 to monitor the lateral uniformity and relative change of the optical path

through the oxide layer *in situ*. The non-polarised light coming from the LED (Linos, HiLED, 470 nm) becomes elliptically polarised once it passes through the Glan-Thompson prism and the zero-order $\lambda/4$ plate. The beam is then reflected off the WE at an angle close to the Brewster angle of water and Si $\alpha = 70^\circ$ for optimal contrast [86]. Depending on the length of the optical path at the electrochemical interface, the ratio between the s- and the p-polarised components of the light changes. The polarisation is then converted into an intensity signal by letting the light pass through a second Glan-Thompson filter. The intensity was measured using a CCD camera (JAI CV-A50) and digitized using a frame grabber card (PCI-1405, National Instruments).

The CCD camera has a frame rate of ≈30 fps. The spatially averaged signal ξ was calculated from single frames and was sampled at 10 Hz. The spatially resolved images were averaged over 30 frames and saved every second. The CCD gives a linear response to the intensity of the incoming illumination, up to a saturation threshold; we present the ellipsometric intensity as a percentage of this threshold. The oscillation amplitude of the ellipsometric intensity signal is generally small compared to its absolute value and thus shows an approximately linear dependence on the optical path length through the oxide layer during the oscillations.

2.3.1 *Image Correction*

In general, the light intensity from the LED varies slightly across the electrode. This leads to a variation of the raw ellipsometric intensity $\xi(\mathbf{x}, t)_{\text{raw}}$ depending on the position $\mathbf{x}$ on the electrode. To adjust for this variation, a background correction was applied by subtracting the temporal average of the raw data $\overline{\xi(\mathbf{x}, t)}_{\text{raw}}$ individually at every point. In addition to this background variation of the intensity, the contrast positively correlates with the absolute value of the LED illumination intensity. Hence, a point on the sample that is illuminated with a high background intensity will have a higher contrast. To counter this, we correct each individual pixel by dividing its value by its temporal average. This correction factor is then normalised by multiplying by the spatial average of the temporal average of the entire image stack in order to keep the unit comparable to the spatially averaged signal ξ.

In total, the correction suppresses the signal from pixels with high temporal average and enhances the signal from pixels with low temporal average. The complete background correction is summarised in Eq. (2.6):

$$\xi(\mathbf{x}, t) = \left(\xi(\mathbf{x}, t)_{\text{raw}} - \overline{\xi(\mathbf{x}, t)}_{\text{raw}}\right) \frac{\langle \overline{\xi(\mathbf{x}, t)}_{\text{raw}} \rangle}{\overline{\xi(\mathbf{x}, t)}_{\text{raw}}}, \tag{2.6}$$

with $\xi(\mathbf{x},t)$ being the corrected local time series and $\langle\overline{\xi(\mathbf{x},t)}_{\text{raw}}\rangle$ the spatial average of the temporal average of the raw data. Note that this correction is only valid as long as the temporal average of the raw data does not change significantly. In the cases where it does change, for example when measuring a transition from one state to another we instead applied the following correction to the recorded images for the spatially resolved figures:

$$\xi(\mathbf{x},t) = \xi(\mathbf{x},t)_{\text{raw}} \frac{\langle\overline{\xi(\mathbf{x},t)}_{\text{ref}}\rangle}{\overline{\xi(\mathbf{x},t)}_{\text{ref}}}, \tag{2.7}$$

with $\xi(\mathbf{x},t)$ being the corrected local time series, $\xi(\mathbf{x},t)_{\text{raw}}$ the uncorrected image, $\overline{\xi(\mathbf{x},t)}_{\text{ref}}$ the temporal average of the local time series of 10 consecutive reference images taken at an instance when the electrode is spatially homogeneous, and $\langle\overline{\xi(\mathbf{x},t)}_{\text{ref}}\rangle$ the spatial average of the temporal average of said reference images.

2.3.2 *Data Analysis*

In order to characterise the dynamics of our system in more detail, we define the amplitude $A(\mathbf{x},t)$ and phase $\phi(\mathbf{x},t)$ of the ellipsometric intensity signal $\xi(\mathbf{x},t)$ at each pixel by calculating the analytic signal $\zeta(\mathbf{x},t)$ via the Hilbert transform $H\left(\xi(\mathbf{x},t)\right)$ [36, 111]:

$$\zeta(\mathbf{x},t) = \xi(\mathbf{x},t) + iH\left(\xi(\mathbf{x},t)\right) = A(\mathbf{x},t)\, e^{i\phi(\mathbf{x},t)}. \tag{2.8}$$

The analytic signal is constructed by taking the original signal at each point as the real part and the Hilbert transform of the original signal as the imaginary part. We take the Hilbert transform of the ellipsometric intensity signal as:

$$H(\xi(\mathbf{x},t)) = \frac{1}{\pi}\ \text{p.v.} \int_{-\infty}^{+\infty} \frac{\xi(\mathbf{x},\tau)}{t-\tau}\, d\tau\,, \tag{2.9}$$

where p.v means that we take the Cauchy principal value of the integral. The Hilbert transform is equivalent to constructing a new dimension in phase space by adding a phase lag of $\pi/2$ to each spectral component. Note that the temporal average of $\xi(\mathbf{x},t)$ has typically already been subtracted in Eq. (2.6), ensuring that the analytic signal will revolve around the origin. This means that we get an intuitive definition of the amplitude of the oscillation as the deviation from the mean and that one oscillation will correspond to one revolution around the origin.

As an example a local time series of ξ is plotted together with the amplitude A in Fig. 2.2(a). As can be seen, the amplitude envelopes the original time series and has an additional modulation with the

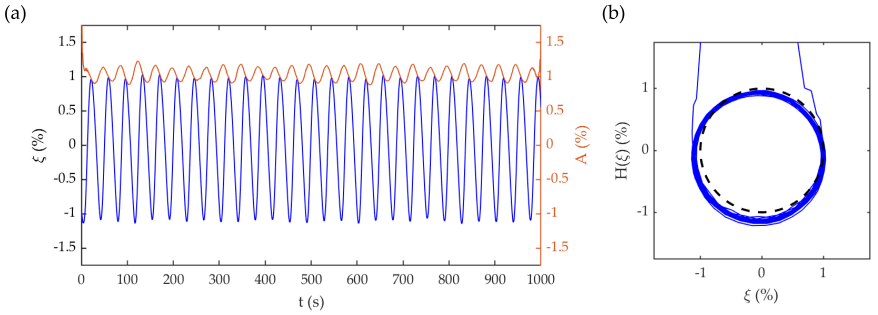

Figure 2.2: Exemplary local dynamics (same as in Fig. 4.2(a)). (a) Local time series of the ellipsometric intensity ξ (blue) and of the amplitude of the analytic signal A (red). (b) Analytic signal in the complex plane (blue) together with the unit circle (dashed).

same frequency as the original time series. The modulation stems from the slight relaxational character of the original signal, i.e., it stems from the oscillation not being a perfect circle centred at the origin. Or in other words, the original local time series does not spend the same amount of time at each phase and hence the amplitude becomes time dependent. The slight offset of the oscillation from the origin can be seen in Fig. 2.2 (b) where the same local time series is plotted against its Hilbert transform together with the unit circle.

When needed we reduced the noise by smoothing the data in the temporal direction by using a Savitzky-Golay filter with a 2nd degree polynomial and a 15 point window. In addition, the data was binned into 5x5 pixels bins when needed to further suppress noise. The data analysis described here was done using libraries and functions from MATLAB [81].

2.4 ILLUMINATION

During the electrooxidation of Si, Si mainly interacts with the electrolyte through valence-band processes. Hence, n-type Si samples have to be illuminated to allow for anodic oxidation. For this purpose we use two different optical configurations, both with a linearly polarised He-Ne laser (HNL150L-EC, Thorlabs) as the light source.

The first configuration was used for measurement series where the electrode was spatially uniformly illuminated and relied on the fact that the laser was linearly polarised. This allowed us to adjust the illumination intensity with a polarisation filter (GTH5M-A, Thorlabs) mounted on a motorised rotation mount (KPRM1E/M, Thorlabs) and placed directly after the laser. The resulting illumination intensity is then given by Malus's law. After the polariser, the beam was widened using a beam expander and then passed through an iris diaphragm. The beam widening and the diaphragm allowed for the illumination of

the entire sample with the central, more uniform part of the beam. A sketch of this illumination set-up configuration can be seen in Fig. 2.1.

However, for some measurements (e.g. in Chapter 5) we needed more control over the spatial distribution of the illumination intensity at the electrode surface. For this a second optical configuration was used, this time combining the laser with a SLM (X10468-06, LOCOS-SLM, Hamamatsu), permitting us to generate an arbitrary intensity image at the sample surface. In this way, we could both ensure an even more uniform illumination intensity and for the case with multiple electrodes, control the illumination intensity of each electrode separately, allowing for different initialization protocols. For this illumination configuration, which can be seen in Fig. 2.3, the SLM is placed after the polarisation filter and the laser light is reflected off it onto the sample.

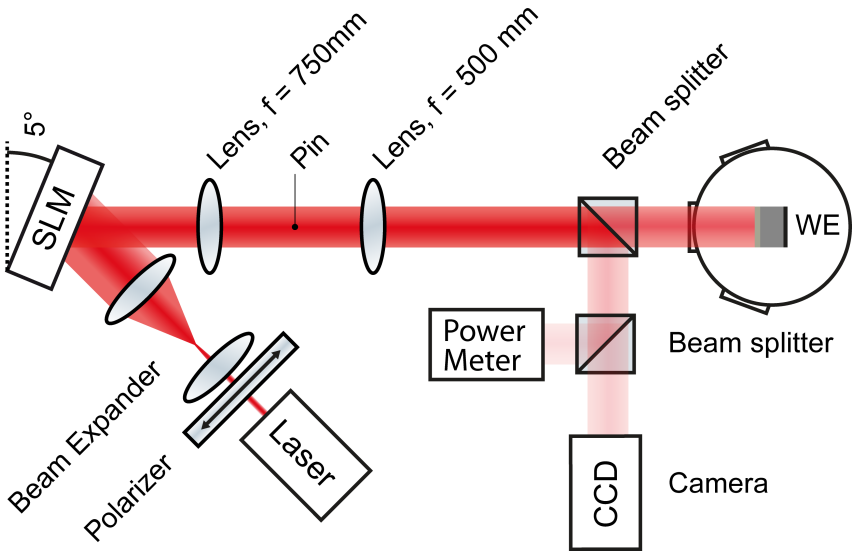

Figure 2.3: Sketch of the illumination configuration using the SLM. In this configuration the spatial distribution of the illumination intensity at the WE can be controlled.

The SLM makes use of the anisotropic electrical and optical properties of liquid crystals allowing for pure phase manipulation of light. By individually addressing each pixel via an active-matrix circuit the liquid crystals in each pixel can be tilted, changing its refractive index which in turn yields a change in optical path. This change in the optical path results in a phase delay upon reflection which in turn yields different intensity images once the light has passed through the succeeding relay lenses. The lenses are placed so that the zeroth order beam can be filtered out using a partial beam blocker and in such a way that, when combined with a digital Fresnel lens on the SLM, we produce a sharp image on the electrode.

In order to monitor the illumination intensity image in situ, we placed a beam splitter in front of the WE directing the beam onto

a CCD (DCC3260-M, Thorlabs) and, using a second beam splitter, onto a power meter (PM16-121, Thorlabs). Note that the optical path from the first beam splitter to the CCD, to the power meter, and to the WE are the same, respectively, in order to accurately determine the properties of the projected image. For more details regarding the specific SLM set-up used here, see Ref. [158]. Note that the intensity of the laser at the WE was much higher than the intensity of the LED used for the ellipsometric imaging. This means that there is no significant contribution from the LED light to the hole generation. Also note that we prevent the light from the laser to reach the CCD camera of the ellipsometric imaging set-up by placing a red colour filter in front of the camera (Fig. 2.1), hence we can exclude any cross talk between the laser illumination and the ellipsometric intensity signal.

2.5 ETCH DEPTH

For some measurements in the following chapters it will be instructive to measure the etch depth. We will see that both the relative and the absolute etch depth can be of interest. For the relative etch depth no reference level is needed and we simply measure the height profile by using a stylus profiler (Dektak 150 Surface Profiler, Veeco). However, in order to measure the absolute etch depth x, a reference point is needed. This was realised by equipping the samples with a thin ridge of Si_3N_4 which is inert in our electrolyte. Then the height of the ridge was measured before and after the electrochemical measurements to determine the absolute etch depth. Exemplary profiles of a Si_3N_4-edge measured with the stylus profiler before and after an electrochemical measurement are presented in Fig. 2.4.

Here the approximate absolute etch depth was 2 μm. To equip the samples with the ridge a Si_3N_4 covered wafer (300 nm Si_3N_4 LPCVD stoichiometric best effort, p-Si 1-10 Ω cm 380$\pm$25 μm, TTV < 10 μm, MicroChemicals) was cut into smaller electrodes. Each electrode was then covered with a layer of photoresist which was developed so as to leave a 20 mm^2 rectangle of exposed Si_3N_4 with a thin ridge of photoresist in the middle. The exposed part of the Si_3N_4 surface was then etched away using reactive ion-etching until the silicon was laid bare. In the next step, the Si_3N_4 on the back was also etched away, again using reactive ion-etching, and then aluminium was evaporated on to the back of the electrode. The electrode was then annealed in order to create an ohmic back contact in the same way as described above. Next, the electrode was mounted on the sample holder and the height of the ridge was determined using the surface profiler. After the electrochemical experiment the height of the ridge was measured again. Si_3N_4 is essentially inert in fluoride containing electrolytes, but to make sure that the thickness of the Si_3N_4 layer did not change it was measured before and after the electrochemical measurement using a

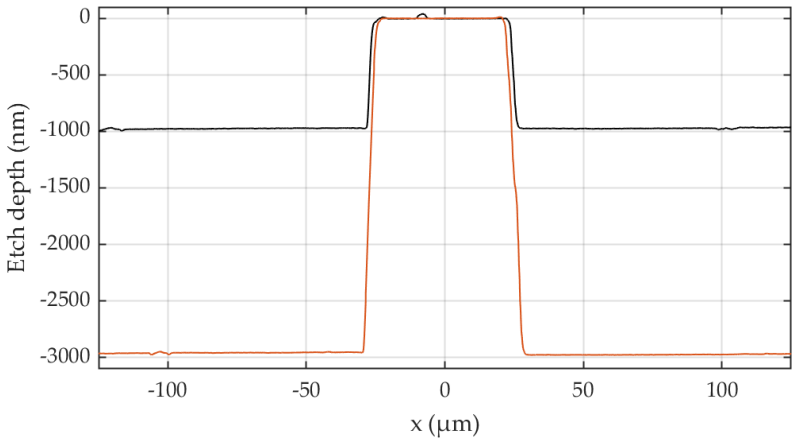

Figure 2.4: Example of Si_3N_4 ridge profile obtained with a surface profiler before (black) and after (red) a measurement consisting of 22 consecutive Cyclic Voltammogram (CV)s from 0.65 to 6.65 V vs SHE and back with a scan rate of 20 mV/s (c_F= 0.05 M, pH 2.3, p-Si (111), 1-10 Ωcm).

commercial ellipsometer (SD2302 Ellipsometer, Plasmos GmbH). For a step-by-step guide to the photolithographic method see Appendix A and Anton Tosolini's Master's thesis [146].

3

PHYSICOCHEMICAL PROPERTIES

Very little is know about the physical mechanism behind the sustained oscillations that occur during the electrodissolution of silicon. Since they were first reported by Turner in the late 1950s [148] they have been studied in great detail by many different research groups, the most notable attempts to uncover the physical mechanism explaining why the oscillations emerge being discussed in Ref. [23, 26, 34, 35, 70, 113, 160]. In this chapter we will take the approach of looking at the most fundamental behaviours of the system, oscillatory or not. This approach is based on the idea that the oscillations, and any other more complicated dynamics, bifurcate from a more simple underlying dynamics, such as a steady state. Thus, we will first look at the system at parameter values at which it does not oscillate and focus on the region where the *IU*-curve exhibits a Negative Differential Resistance (NDR). Second, we will show that even without an external resistor or a current-limit-inducing illumination the system exhibits self-sustained oscillations. Third, we will investigate the influence of the illumination on these oscillations.

We start by looking at the current-voltage characteristics of the system (Sec. 3.1) before measuring the steady state of the system on the NDR branch and determine the dissolution valency (Sec. 3.2). The fact that the dissolution valency increases with increasing potential is a fundamental assumption in the new model proposed by our group [120]. The proposed physical model explains part of the current–voltage characteristics of the system as well as the impedance spectrum on the NDR branch.

Next, we investigate what happens to the system at slightly higher applied potentials and see that for certain parameters at voltages beyond the NDR branch the system oscillates (Sec. 3.3). It was previously thought that the system needed a global coupling, either a linear one in the form of an external resistor or a nonlinear one in the form of an illumination induced current limitation, for the oscillations to remain stable. Hence, the findings that the system remains in an oscillatory state even without a global coupling, both for highly illuminated n-Si and for p-Si in the dark, is both unexpected and new. Seeing that the oscillations are self sustained allows us to explore how the illumination intensity affects the spatio-temporal dynamics in the absence

of an external resistor. We end this chapter by investigating at what parameters patterns appear and discuss how the valence band hole dynamics influences the spatial coupling.

The results in this chapter were in part published previously in Ref. [107] and in Ref. [120]. The protocol for measuring the dissolution valency was developed in part together with Anton Tosolini during his Master's thesis [146] which was supervised as part of this thesis project. The discussions regarding the dissolution valency based on the experimental work presented here relies in part on work made in collaboration with Munir Salman who developed the model presented in Ref. [120] in parallel to this work. Preliminary work on the oscillations without external resistor and the measurements regarding parameter gradients across the WE were done by Richard Hueck during his Master's thesis [49] which was also supervised as part of this thesis project.

3.1 SLOW CYCLIC VOLTAMMOGRAM

We showed in Ref. [106] that when performing a sufficiently slow CV, i.e. sweeping the applied voltage linearly versus time between two set voltages, the resulting quasi-static state constitutes a good approximation to the steady state of the system. In particular it was found that the NDR branch of the CV is stable and hence that it also constitutes a steady flow state. However, further insights into exactly what the physical properties of the steady flow state are were not investigated. We start this section by looking closer at the CV and demonstrating that it is indeed a good approximation to a steady state on the NDR branch. We then increase the applied potential and look closer at the part of the CV where minor oscillations can be seen and confirm that these are in fact oscillations that remain stable when the potential is held constant even without an external resistor, contrary to what was previously assumed.

Fig. 3.1 shows an exemplary, slow CV of the Si-system using a p-doped silicon electrode. Note that the CV looks the same for highly illuminated n-doped silicon, with the exception of a few hundred mV shift on the voltage axis corresponding to the difference in Open Circuit Potential (OCP) [69, 107].

The CV can be divided into four main regions: first, the region below the peak denoted as U_1. The peak itself is associated with the formation of pores [37, 68] in the silicon and the change from mainly divalent to tetravalent oxidation [33]. Second, the region between U_1 and U_2, the so-called electropolishing branch. At voltages below the peak denoted as U_2, the chemical etching is faster than the electrochemical oxidation resulting in a practically oxide free electrode and a current that increases with increasing voltage. This is different in the

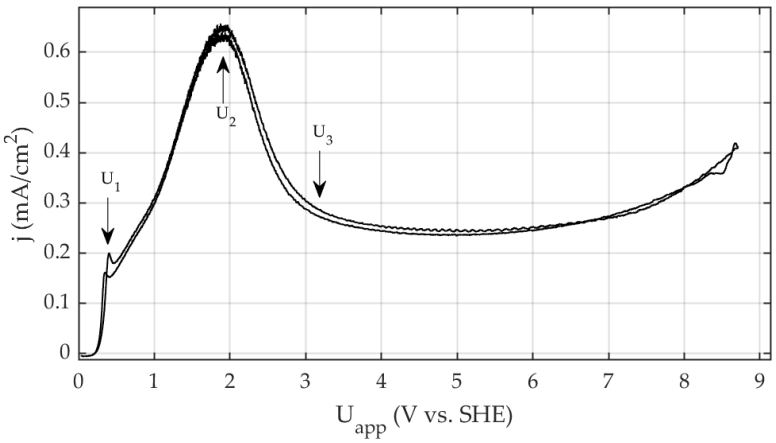

Figure 3.1: CV of a p-Si electrode (5-25 Ωcm) in an electrolyte of 0.06 M NH_4F, pH 1. Scan rate: 2 mV/s. The borders of the NDR branch are marked by the arrows U_2 at 1.75 V vs SHE and U_3 at 2.75 V vs SHE, U_1 marks the transition to the mainly tetravalent regime.

third region, the NDR branch between U_2 and U_3 where an oxide layer starts to form, and in the fourth region, the region above U_3 where the oxidation current is limited by how fast the oxide is etched. Since the etching is purely chemical, the current becomes practically independent of the applied potential in the forth region up to approximately 7 V where it starts to increase slightly, most likely due to morphological changes.

The region, up to U_2, has been studied to quite an extent, see Ref. [160] for an overview, and will not be further investigated here. We will instead start by turning our attention to the NDR branch between U_2 and U_3 and then continue to higher potentials.

3.2 NEGATIVE DIFFERENTIAL RESISTANCE BRANCH

Once the applied voltage is higher than U_2 the current starts to decrease with increasing voltage, i.e. we observe a Negative Differential Resistance (NDR). The exact physical reason why this happens was hitherto unknown and even more surprising, no one knew if this branch is stable or not. We investigated whether the branch remains measurable due to the finite scan rate or if it is in fact an equilibrium branch in Ref. [106]. It was found that the NDR branch is indeed a stable steady state and here we have reproduced these results, with additional measurement points.

In order to measure this, we drove the system into a neighbouring state via a faster CV, stopped the scan, and then kept the applied voltage constant.

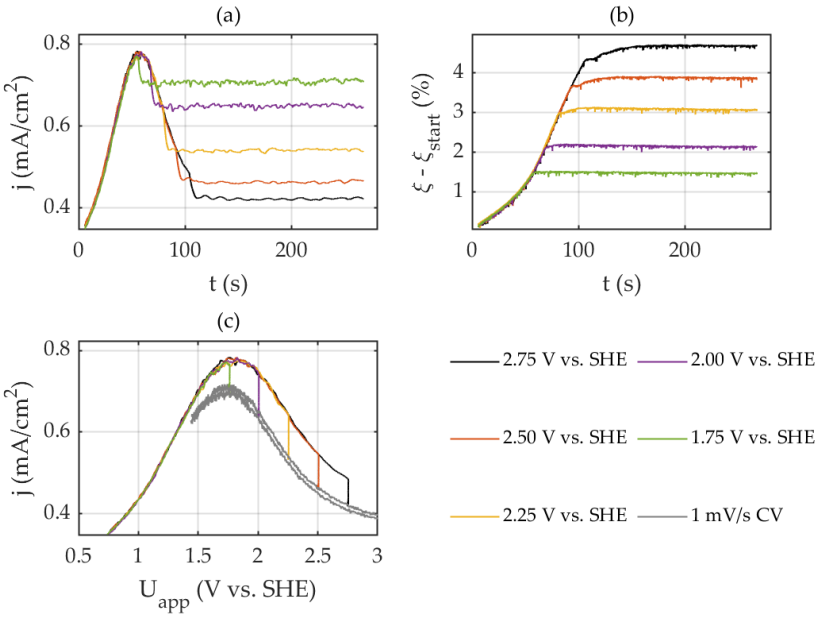

Figure 3.2: 20 mV/s CVs of p-Si in a fluoride containing electrolyte (c_F = 0.05 M, pH 2.3) scanned to different voltages (see legend) and then held at the respective voltage. (a) Current density vs time. (b) Ellipsometric intensity signal minus the ellipsometric intensity signal at the steady state at the start of the scan. (c) Current density vs applied voltage, compared to a 1 mV/s CV (p-Si (111), 5-25 Ωcm).

In Fig. 3.2 a scan rate of 20 mV/s was used and the voltage was held at constant values on the upward scan when the desired value for the applied voltage was reached. We show the current j vs time and the spatially average ellipsometric intensity ξ vs time in Fig. 3.2 (a) and (b), respectively. To attain an initial reference value for the ellipsometric intensity signal these measurements were initialised by jumping from OCP to an arbitrary point on the electropolishing branch between U_1 and U_2, here 0.65 V vs SHE[1], and holding the potential fixed at this value for 30 s. In Fig. 3.2 (b) the initial reference value has been subtracted and the resulting ellipsometric intensity signal is shown. It can be seen that once the scan is halted, both the ellipsometric intensity signal and the current density reach a steady state almost immediately. Upon very close inspection we also see a short transient oscillation for higher potentials, especially for the measurement that was held at 2.75 V vs SHE. Note that these transient oscillations are different from the noise seen at lower potentials. The transient oscillations can also be seen in the ellipsometric intensity signal, albeit not as clear since the signal simultaneously increases slightly on average.

1 This value was chosen due to its reproducibility and fast transient

In plate Fig. 3.2 (c) the current density is plotted against the applied voltage together with a 1 mV/s CV. Here, one can clearly see that the steady states that the system settles in after the initial transients have decayed do indeed coincide with the slow CV. Hence, we have reconfirmed two things. The NDR branch is a stable branch of the system and the slow CV (1 mV/s) presented here is a good approximation of it. Notably, at lower applied potentials the system shows an exponential decay in the current and settles at the steady state almost immediately. This non-oscillatory transient indicates that in this part of the parameter space the stationary state is a stable node. At slightly higher potentials, where we see the transient oscillations, this node-like behaviour changes, and the stationary state becomes a stable focus.

3.2.1 *Physical Mechanism Resulting in the NDR Branch*

As for the question "What physical processes lead to the NDR behaviour?" or "Why does a passivating oxide layer start to form?" we turn to the model by Salman et al. [120]. We, the authors, presented a model which aims to explain why the current decreases with higher potential in the NDR region. The underlying idea of the model is that the etch rate depends on the degree of oxidation of the silicon oxide layer. The model predicts that a higher applied voltage leads to more fully oxidised silicon. Since we assumed that the fully oxidised silicon is etched more slowly the current would then decrease with increasing applied voltage resulting in a NDR.

To better understand how this can come about we look at Fig. 3.3 where a schematic band diagram is sketched together with the three main steps in the electrodissolution of silicon as assumed in the model. The first step is the electrochemical oxidation step at the silicon silicon-oxide interface. Here the silicon can be partially oxidised (SiO) or fully oxidised (SiO_2). The second step takes place inside the oxide layer and consists of the chemical reaction that further oxidises the partially oxidised SiO formed in step 1 to SiO_2. Note that the reaction presented here is a simplification that does not take any sub-steps into account. Also note that these reactions lead to good predictions but that it might also be possible to use reactions with e.g. OH^- and $Si(OH)_x$[2] instead of O^{2-} and SiO_x. The third and final step is the chemical etching of the oxide at the oxide-electrolyte interface. This is where the main idea of the model comes into play; SiO is assumed to be etched faster than SiO_2. Note also that the model assumes that the reaction leading to O^{2-} ions entering the oxide layer is very fast compared to the transport of the ions in the oxide and that the chemical potential of the O^{2-} ions at the oxide-electrolyte interface is prescribed by the electrolyte.

2 Compare to Eq. (2.1) and Eq. (2.2)

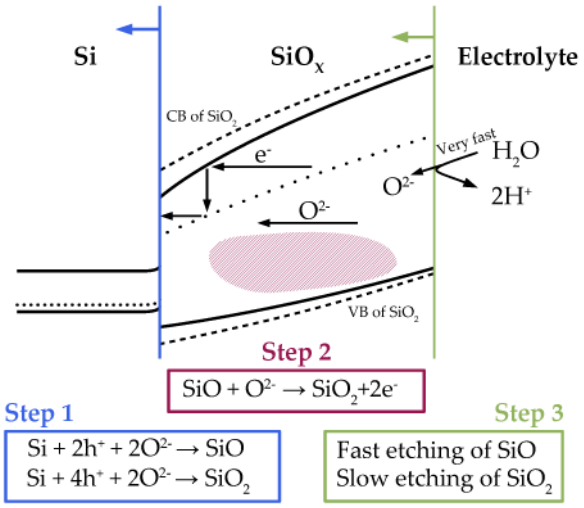

Figure 3.3: Schematic band diagram of the model presented in Ref. [120], not to scale. Note that the bandgap of SiO_x (solid black line) is smaller than that of pure SiO_2 (dashed black line) [75].

Next, we take a look at what happens to the current when we increase the potential: increasing the potential first leads to a higher electric field and thus to more O^{2-} ions at the silicon silicon-oxide interface. This means that both reactions in step 1 increase. This then leads to a thicker oxide layer. A thicker oxide layer means that the ratio of the rates of step 2 and step 1 increases or in other words that on average we see a higher degree of oxidation. Here, a higher degree of oxidation means that the amount of silicon oxide that has been fully oxidised increases and that the dissolution valency approaches 4. Since the main assumption was that fully oxidised silicon is etched more slowly this higher degree of oxidation would mean that step 3 becomes slower, in turn, resulting in a lower equilibrium current.

3.2.2 *Dissolution Valency*

One way of testing this model is to measure the dissolution valency along the NDR branch. Does it increase with increasing applied voltage?

We first turn to the literature. As mentioned in Chapter 2.1, the idea that there are two different oxidation processes, leading to different dissolution valencies, was first suggested by Uhlir [149] and Turner [148]. They claim that there is one divalent and one tetravalent oxidation process and both found that the mechanism changes from being mainly divalent to being mainly tetravalent at the first peak of the CV, marked with U_1 in Fig. 3.1, something that was later confirmed by Memming and Schwandt [84]. Going to voltages above U_1, Eddowes [33] preformed coulometric measurements in combination with measurement of sample weight-loss. He found that the dissolution valency

increased from around 2 at U_1 to approximately 3.6 at the plateau U_3. This supports the model but one should note that the CVs measured by Eddowes have a slightly different shape and a very steep NDR branch. The steep NDR branch could be the result of a possible resistance in the system. As the NDR branch is so steep, there is only one measurement point that can be said to lie within this voltage region and it is difficult to give a conclusive statement regarding the exact dissolution valency along the NDR branch.

As can be seen above in Eq. (2.1), the divalent process is accompanied by hydrogen evolution whereas the tetravalent one takes place without any hydrogen evolution. Stumper et al. [19, 140] made use of this fact and confirmed the findings by Eddowes by performing hydrogen detection measurements during CVs with a scan rate of 10 mV/s, using a rotating ring disk electrode (RRDE) set-up. Schönleber et al. [128] also performed hydrogen detection measurements during a CV (5 mV/s) in a flow cell and found similar dissolution valencies. They measured the hydrogen evolution during the upwards scan. The results in these papers have a high resolution in the potential direction on the NDR branch. The issue now instead lies in the scan rate being fast on the time scale of the formation and dissolution dynamics of the oxide layer. Problems arise when scanning with a scan rate that is so fast that the system does not have time to settle in its steady state. In Fig. 3.4 the CV from Fig. 3.1 is compared to the slightly faster CV that Schönleber et al. measured [128] whilst determining the H_2 production.

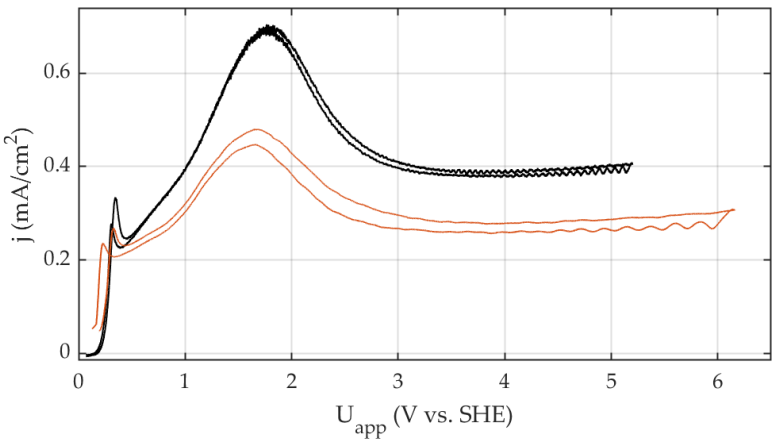

Figure 3.4: Black: CV, 2 mV/s, stirred (p-Si (111), 5-25 Ωcm). Red: CV, 5 mV/s, flow cell, data from [128] (p-Si (100), 10-20 Ωcm). Both measurements in an electrolyte with pH 2.3 and $c_F = 0.05$ M.

As can be seen, there is a hysteresis between up-scan and down-scan in the faster, 5 mV/s, CV indicating that the system did not have time to settle in its real steady state during the H_2 measurement since they

were performed during the upwards scan. Note that the difference in absolute value between the CVs in Fig. 3.4 most likely comes from a difference in the mass transport of the educt and possibly from the different crystal orientations and resistivities. The change in mass transport stems from differences in the cell geometries.

The hysteresis has been shown to increase with higher scan rates [106, 159] and hence we assume that the H_2 measurements by Schönleber et al. as well as the measurements by Stumper et al. (even faster scan) were not conducted in a quasi-stationary state.

Hence, the measurements in the above mentioned references are either lacking in resolution in the potential direction [33] or are not measured in a steady state [19, 128, 140].

Since we have confirmed that the states along the NDR branch of the CV are in fact stable, can we overcome these problems and measure the dissolution valency in a steady state in this region with a sufficient resolution in the potential direction?

Yes. In order to determine the dissolution valency of the silicon at different applied potentials we measured the current density j, and the etch depth x, at constant applied potentials. With these two variables the dissolution valency was calculated using the following relation:

$$v = \frac{m_{\mathrm{Si}}}{xe\rho_{\mathrm{Si}}} \int j \, \mathrm{d}t, \tag{3.1}$$

where e is the elementary charge, m_{Si} is the mass of a silicon atom (28.0855 u), and ρ_{Si} is the mass density of bulk silicon (2.3290 g/cm^3).

In order to measure the etch depth we use the method described in Sec. 2.5. The measurement protocol consisted of two steps: first, a 20 mV/s CV in order to confirm that the fabrication was not flawed and second, a jump in potential from OCP to a fix potential which was then held for approx. 10^4 s.

An average etch depth of the type of CV that was conducted at the start of each measurement was determined in separate measurements and we corrected for it in order to not overestimate the etch depth in the steady state. During the evaluation a correction was also made for the slight height difference stemming from the slight etching of the Si_3N_4. Samples from two different wafer-batches were used. Since it is possible that minor production errors might have an effect on the Si-Si_3N_4 interface, care was taken to use different average etch depths of the initial CVs when evaluating the different sample batches.

The measured dissolution valencies are shown in Fig. 3.5.

The dissolution valency increases strongly from around 3.2 directly above U_1 to 3.7 at U_2 and then to about 3.8 at U_3.

In order to compare the measured values to previous literature values, the same data is shown in Fig. 3.6 together with the data measured by Schönleber et al. [128].

The average etch depth of the initial 20 mV/s reference CV from 0.65 V vs SHE to 6.65 V vs SHE and back was found to be 90 nm for the

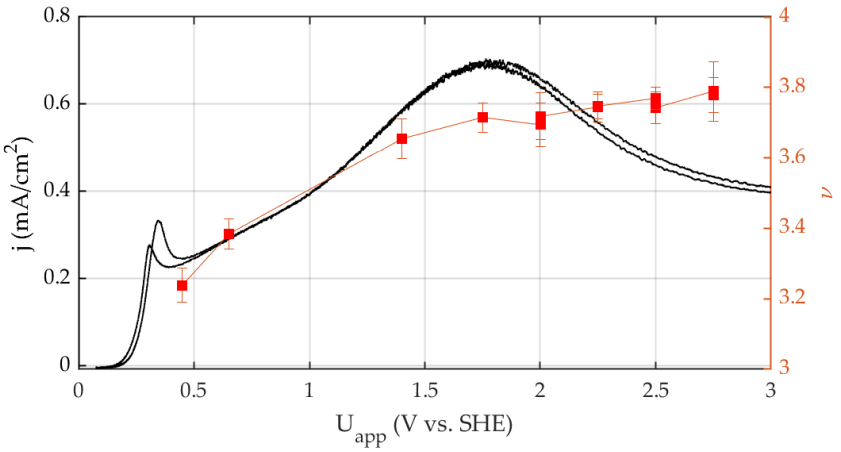

Figure 3.5: Dissolution valencies ν measured ex-situ using the photolithographic method shown superimposed on a 2 mV/s CV, (p-Si (111), 1-10 Ωcm, pH 2.3 $c_F = 0.05$ M.

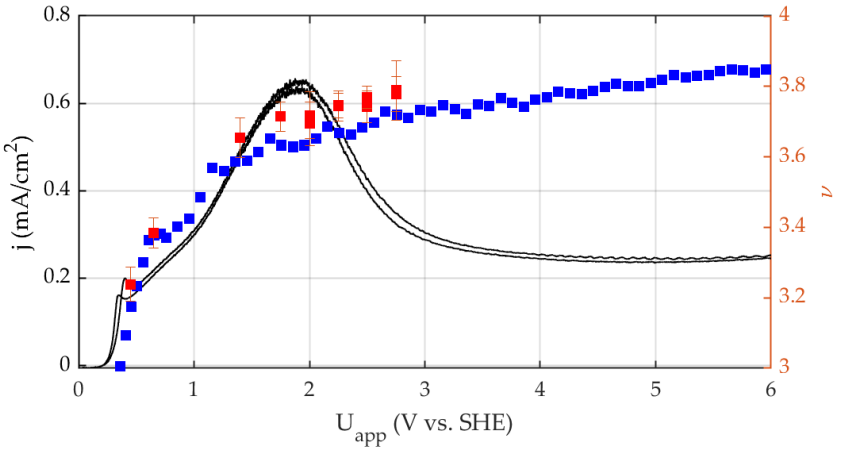

Figure 3.6: Comparison of dissolution valencies ν measured with the photolithography method (red) (p-Si (111), 1-10 Ωcm) to the dissolution valencies measured by Schönleber et al. [128] (p-Si (100), 10-20 Ωcm) (blue), both superimposed on a 2 mV/s CV.

fist wafer and 80 nm for the second wafer. The average etch rate of the Si_3N_4 was found to be 5 nm/h. The errors bars are calculated from the error in the surface profiler data.

3.2.3 *Discussion*

The above presented dissolution valencies are in good agreement with the literature. Our values are slightly higher than the previously reported ones but show a similarly increasing slope in the NDR region (cf. Fig. 3.6). We can be confident that our measurements are reliable since they were performed after the system had attained a stationary state, not during a potential scan. It is reasonable to assume that the slightly higher dissolution valencies could in part be explained by the fact that most measurements presented in the literature were carried out in non-steady states. A measurement that is conducted out of the steady state gives a false dissolution valency for the corresponding applied voltage. For example, if one measures the valency during the upward scan of a fast CV, cf. Ref. [130], the oxide layer will be slightly thinner, corresponding to the state at a lower potential. This roughly corresponds to a shift of the dissolution-valency curve from Ref. [130] in Fig. 3.6 to higher potentials compared to the actual stationary value. Correspondingly, one would need to shift the curve to lower potentials to get the true valency.

As mentioned above, the measurements in Ref. [33], also performed in a stationary state, lack in resolution in potential direction in the NDR region. Our measurements are, in addition to measuring in the steady state, measured with a sufficient resolution in the NDR region to see the change of the dissolution valency within this region. Where our method lacks is at lower potentials. It is ill suited to determine the dissolution valency at lower potentials due to the porous nature of the silicon at U_1 [37, 68].

In addition to the above discussed measurements an attempt was made to determine if any secondary process takes place, more specifically whether any H_2O_2 is produced or not. This could be the case if, due to the formation of a pore in the silicon oxide or a very high electric field in the double layer which occurs for thin oxide layers, water would be oxidised to H_2O_2. If H_2O_2 would be produced the current density in Eq. (3.1) would have to be corrected to a smaller value, resulting in a lower dissolution valency. To determine if any H_2O_2 was formed during the electrodissolution, we used a photometric method as described in a standard procedure by the German Institute of Standardization (DIN 38 409 - 15) [32]. In short, the detection method is based on the formation of the yellow TiO_2^{2+} complex when an aqueous solution of $TiOSO_4$ (Sigma-Aldrich, 1.9–2.1 %, for determination of hydrogen peroxide (H 15), according to DIN 38 409, part 15, DEV-18) is added to a H_2O_2 containing solution. The amount of H_2O_2 can

then be quantitatively determined using a UV-VIS spectrometer. The detection limit of our spectrometer lies at intensities corresponding to ca. 0.1 mM. After electrolysis at 2 V vs SHE for $1.1 \cdot 10^4$ s in a smaller cell (PCTFE, three separate compartments, 4 ml WE-compartment, see Ref. [161] for details on the cell) and adding 1 ml $TiOSO_4$ solution no change in light-adsorption was detected. Hence, we conclude that less than 0.1 mM H_2O_2 is produced. 0.1 mM H_2O_2 corresponds to a faradaic efficiency of 3.3% and would reduce the above measured valency at 2 V vs SHE by approximately 0.12. This is an upper limit of the effect of H_2O_2 production on the valency and it is comparable to the error of the surface profiler.

3.3 OSCILLATIONS WITHOUT EXTERNAL RESISTANCE

Leaving the potential region of the NDR branch for slightly higher potentials we see that upon closer inspection of the CVs in our base electrolyte (pH 1), cf. Fig. 3.1, the plateau current is superimposed on small oscillations in a wide potential window. To test for the stability of these oscillations, we performed potential step experiments from the OCP to a potential value within the region where the oscillations can be seen in the CV. Three such experiments are depicted in Fig. 3.7 for potential steps to 3.15, 4.65 and 7.65 V vs SHE. The respective two upper graphs show the time series of the current density (left) and the spatially average ellipsometric intensity (right) after the potential jump. The left graph below depicts a 2D ellipsometric snapshot of the electrode, and the right one a one-dimensional cross section through the ellipsometric images versus time. Clearly, in Figs. 3.7 (a) and (c) the oscillations are damped, while in (b) we see small amplitude oscillations that persist over several thousand seconds and acquire a stable amplitude.

This is surprising. It was previously thought that the oscillations could only be stabilised by adding an external resistor in series with the WE [26]. Here we see that in this electrolyte the system exhibits stable oscillations even without the insertion of an external resistor.

In this region of sustained oscillations without an external resistance phase waves usually emerge on the electrode, as can be seen in the ellipsometric image of Fig. 3.7 (b). As a consequence, the local oscillation amplitude of the ellipsometric intensity was larger than the average one. In Fig. 3.8 the potential regions in which transient and self-sustained oscillations were found are indicated by I and II, respectively, with the borders between them shown as a hashed region. The width of the borders indicate the uncertainty in the determination of the threshold voltage. This uncertainty is due to the ever slower damping as the transition to sustained oscillations is reached. The low voltage border where damped oscillations start to exist could also only be determined with a relatively large uncertainty as indicated by the

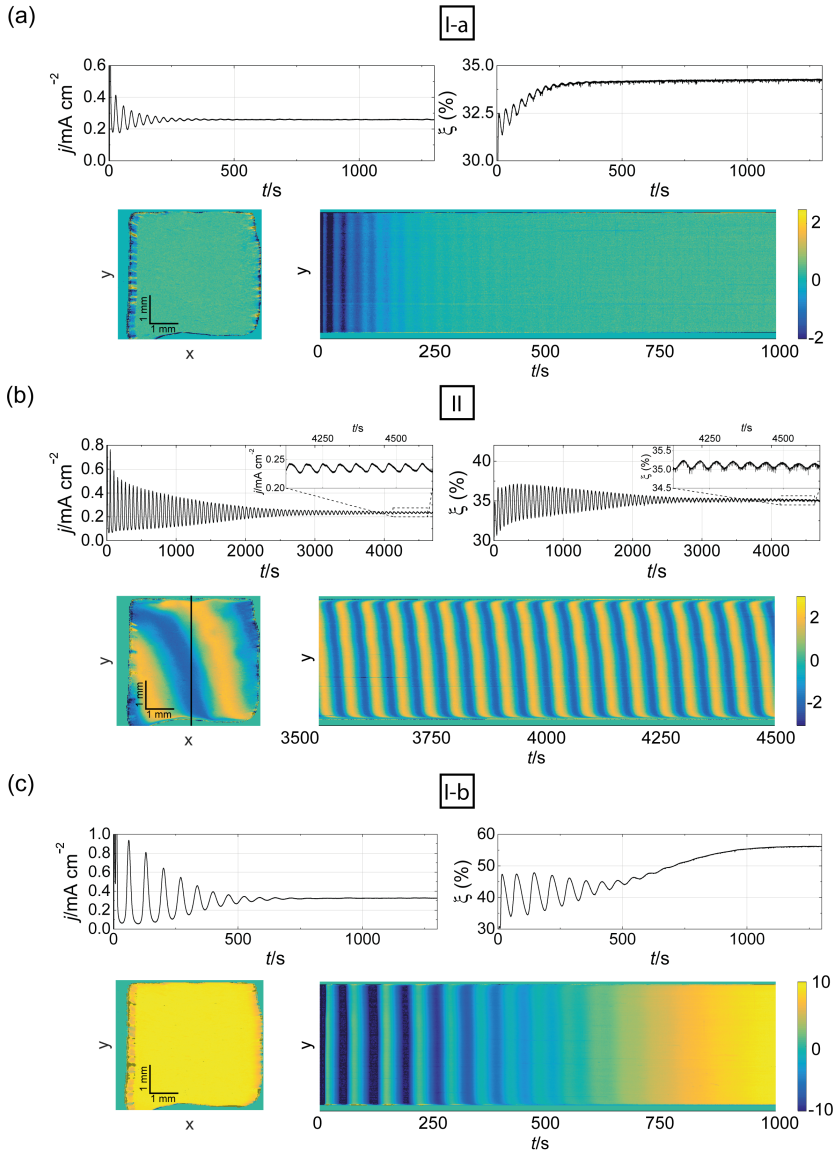

Figure 3.7: Dynamics found in the different regions marked in Fig. 3.8. Current density, j, and spatially averaged ellipsometric intensity, ξ, (top) together with the ellipsometric intensity distribution on the electrode and the temporal evolution of a 1D cut indicated in the snapshot. (a) Damped oscillations at $U_{app} = 3.15\,V$ vs SHE, region I-a, snapshot at $t = 1000\,s$. (b) Stable oscillations at $U_{app} = 4.65\,V$ vs SHE, region II, snapshot at $t = 4000\,s$. (c) Damped oscillations at $U_{app} = 7.65\,V$ vs SHE, region I-b snapshot at $t = 1000\,s$. All measurements with highly illuminated n-Si ($3.88\,mW/cm^2$) in a 0.06 M NH_4F solution (pH 1).

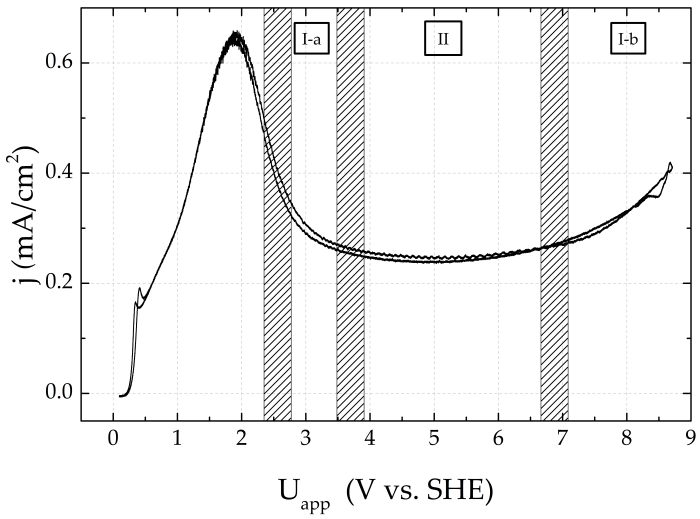

Figure 3.8: Cyclic voltammogram (2 mV/s) of a p-Si electrode in a 0.06 M aqueous NH_4F electrolyte, pH 1. Region I-a and I-b indicate the voltage regimes where damped oscillations were found. Region II indicates where sustained oscillations were found. Hashed regions indicating the approximate borders between the different regions.

width of the hashed lines. This is the same transition from a node-like behaviour to a focus-like behaviour we saw in the measurements for determining the stability of the NDR branch, cf. Fig. 3.2. Note however that the electrolyte used in Fig. 3.2 was different. In Fig. 3.9 the same type of measurement as in Fig. 3.7 (b) is presented, but with the same electrolyte as in Fig. 3.2 with 0.05 M NH_4F and a calculated pH of 2.3. Here, no stable autonomous oscillations were observed without an external series resistor (neither with n- nor with p-doped Si electrodes) confirming findings in the literature [26]. Note the finer colour scale compared to Fig. 3.7. Clearly, both the spatially averaged signal and the spatially extended signal show a continuous damping, in contrast to the behaviour in Fig. 3.7 (b). In other words, for this measurement, as well as in all other measurements in the electrolyte with 0.05 M NH_4F and pH 2.3, the system eventually reached a stationary state. No stable oscillations are found and region I-a reaches all the way to region I-b.

3.3.1 *Spatial Pattern Formation*

In previously published measurements on pattern formation during the photo-electrodissolution of n-Si a linear global coupling in the form of a resistor in series with the WE has typically been used [87, 88, 124, 125, 130]. In addition to the possible introduction of the linear

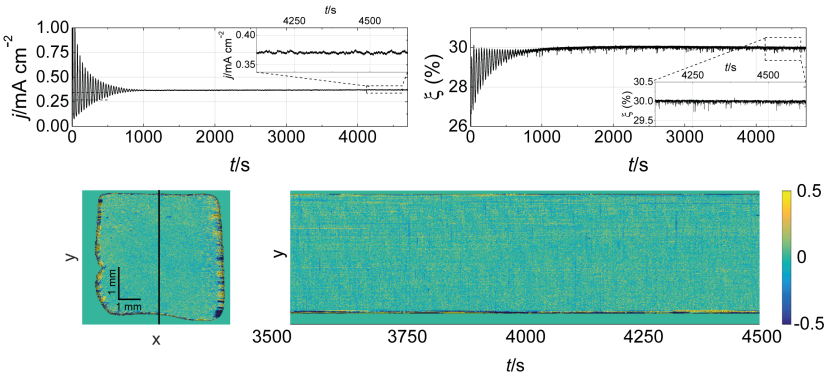

Figure 3.9: Current density, j, and spatially averaged ellipsometric intensity, ξ, (top) together with the spatially averaged ellipsometric intensity distribution on the electrode at $t = 4000\,\mathrm{s}$ and the temporal evolution of a 1D cut indicated in the snapshot. $U_{\mathrm{app}} = 4.65\,\mathrm{V}$ vs SHE, highly illuminated n-Si ($3.88\,\mathrm{mW/cm^2}$) in a $0.05\,\mathrm{M}\,NH_4F$ solution (pH 2.3).

global coupling a second type of coupling mechanism was present in these studies. This second type of coupling was induced by the fact that in all of them the illumination intensity was reduced in such a way that the total current was cut off due to the limited generation of holes in the valence band. This restriction of the current lead to a nonlinear coupling with an—at least partly—global character, seeing as the total current is determining its strength [124].

In the previous section we demonstrated that the sustained oscillations obtained in our base electrolyte emerge even without an external series resistance. Therefore, we are now in a situation in which we can study the influence of the spatial coupling induced when lowering the illumination without the simultaneous presence of the linear global coupling brought about by the ohmic series resistance. We will also see that the electrodes splits into different regions even without an illumination limited current plateau meaning that the nonlinear coupling through the valence band holes does not have to be strictly global for patterns to emerge.

While, when we omit the external resistor, reducing the illumination intensity always induced the spontaneous formation of regions with different oscillatory dynamics, the specific characteristics of the emerging pattern sensitively depended on the value of the illumination intensity.

An example where different oscillatory dynamics emerges can be seen in Fig. 3.10. Here, the global time series of current and spatially averaged ellipsometric intensity become irregular. The temporal evolution of the 1D profile suggests that there is an almost periodically oscillating region with a somewhat higher mean amplitude, flanked

by incoherently oscillating regions. As such this state is reminiscent of a chimera state.

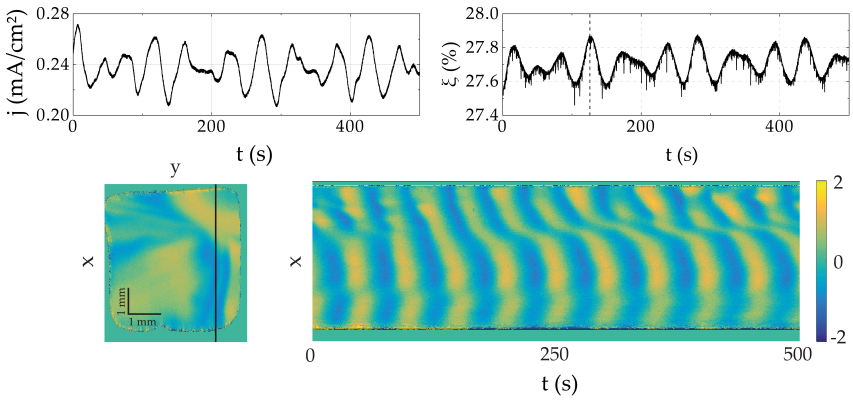

Figure 3.10: Current density, j, and spatially averaged ellipsometric intensity, ξ, (top) together with the ellipsometric intensity distribution on the electrode at $t = 126\,\mathrm{s}$ (indicated by dashed line in in the top right panel) and the temporal evolution of a 1D cut indicated in the snapshot. $U_{\mathrm{app}} = 4.65\,\mathrm{V\,vs\,SHE}$, illumination intensity $0.34\,\mathrm{mW/cm^2}$, $0.06\,\mathrm{M}$ NH_4F, pH 1.

If the illumination intensity is lowered even further, below a critical value where the amount of available holes no longer suffice to uphold an oxide layer, both the oscillations and the patterns vanish. Instead, the system attains a uniform steady state with a high current density. Fig. 3.11 depicts how the current density and the spatially averaged ellipsometric signal developed immediately after lowering the illumination intensity during a measurement from a high value, where the system oscillated (cf. Fig. 3.7 (b)), to an illumination at which the oxide layer was no longer stable. Note that the current is limited during part of the oscillation but that the limit increases as the oxide layer, as measured by the ellipsometric intensity signal, withdraws from the surface. In the temporal evolution of the 1D cut as well as in the snapshots we see that the initially approximately uniform oxide layer quickly develops two regions with different mean thickness, one of them again being incoherent in space and time, before a uniform state with low ellipsometric intensity signal and a high current density spreads over the entire surface. The transient dynamics seem to traverse through the dynamic states that are stable in an interval of a somewhat higher illumination intensity. In other words it seems plausible that it might be possible to observe a stable state with dynamics reminiscent of the transient dynamics at slightly higher illumination intensities. This would be especially interesting due to the chimera like transient seen at up to 450 s in the 1D cut.

To recapitulate, we have demonstrated that a lower but uniform illumination intensity induces the formation of spatial patterns or

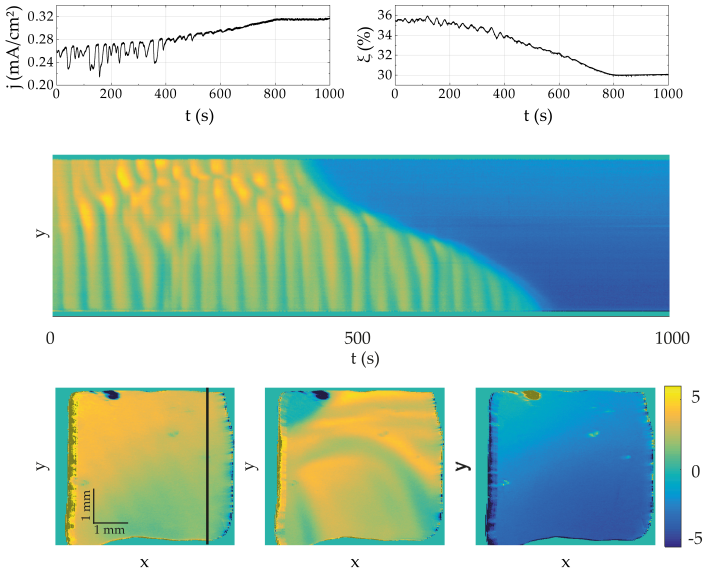

Figure 3.11: Current density and spatially averaged ellipsometric intensity (top), 1D temporal evolution of the ellipsometric intensity signal at the cut indicated in the snapshot (middle) together with the ellipsometric intensity distribution on the electrode at three instances in time ($t = 0\,\mathrm{s}$, $t = 185\,\mathrm{s}$, $t = 900\,\mathrm{s}$) (bottom). $U_{\mathrm{app}} = 4.65\,\mathrm{V}$ vs SHE, illumination intensity $0.25\,\mathrm{mW/cm^2}$, 0.06 M NH_4F, pH 1.

domains with different dynamics, whereby one of them might oscillate incoherently in space and time, being reminiscent of a chimera state.

A different way to probe the influence of the illumination intensity is to only illuminate a part of the electrode. In this way, a gradient in the density of valence band holes is created at the boundary of the illuminated region such that we can expect an outward flow of holes, which mimics a gradient in the illumination intensity, and thus again sheds light on the role of the spatial coupling through charge carriers in the semiconductor and its interaction with the oxide formation/dissolution dynamics.

Fig. 3.12 shows one such example measurement. Here, the opening of the circular aperture in the illumination path (cf. Fig. 2.1) was adjusted to a narrower opening so that only approximately the part of the electrode inside the area indicated by the dashed circle was illuminated. The illumination intensity was set to a level below the high illumination level of Fig. 3.7 and above the level necessary for creating multiple domains. Under these conditions, concentric waves of slightly higher ellipsometric intensity propagated from the rim of the illuminated circular region towards its centre. In the course of time, the border from which these waves emerged withdrew slowly towards the centre, Fig. 3.12 depicting a situation after about half an hour, the outer illuminated ring now taking on a constant value in the ellipsometric intensity. Here, the temporal average of each pixel

is subtracted such that all non-oscillating parts of the electrode are set to 0. We note that after about 8 hours the illuminated surface became uniform and the dynamics stationary, however, due to the enormous duration of the experiment in which one can expect also minor changes in electrolyte composition and possibly also other parameters (e.g. temperature) it does not seem to be sensible to further interpret this result.

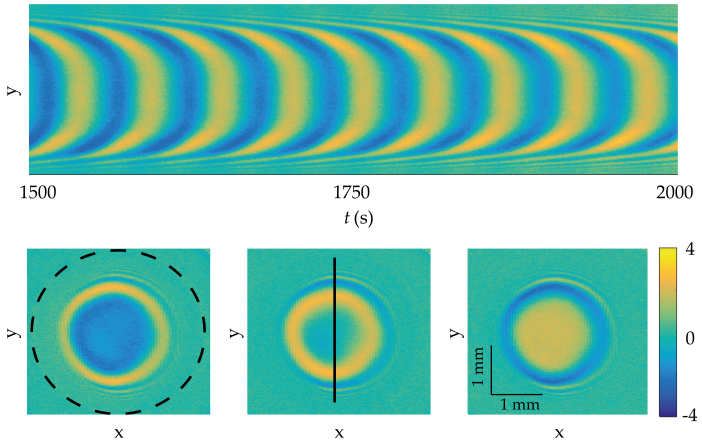

Figure 3.12: Resulting 1D temporal evolution of the ellipsometric intensity when only the centre part of the electrode was illuminated, together with the ellipsometric intensity distribution on the electrode ($t = 1730\,\mathrm{s}$, $t = 1745\,\mathrm{s}$, $t = 1760\,\mathrm{s}$). The illuminated part is indicated by the dashed circle in the left most snapshot and the 1D cut is indicated in the middle snapshot. The temporal average of each pixel was subtracted. $U_{\mathrm{app}} = 4.65\,\mathrm{V}$ vs SHE, illumination intensity $0.78\,\mathrm{mW/cm^2}$, 0.06 M NH_4F, pH 1.

3.3.2 *Discussion*

The ellipsometric snapshot in Fig. 3.7 shows that in contrast to findings in the presence of an external resistance [87, 88, 124, 125, 129, 130], the oscillations were accompanied by wave like structures, apparently propagating across the electrode. This is true for p-type as well as highly illuminated n-type Si. In successive experiments with different samples the orientation of the waves was always the same. Furthermore, the wavelength decreased over time. We attribute these waves to a slight parameter gradient in the system that, in turn, induces a slight gradient in the frequency distribution which implies that the apparent waves are phase waves.

To investigate if the origin of the phase waves was related to connection between the back contact and the wire we used a Cu sheet to bring them in electrical contact, using Ag conductive paste over the entire area of the electrode. Since the phase waves persisted we consider it unlikely that the parameter gradient is caused by the back

contact. In addition, when rotating the electrode by 180°, the phase waves kept their apparent propagation direction in the laboratory frame. Therefore, we also exclude an inhomogeneity in the doping level. Since we observed the phase waves for p-doped silicon which we do not need to illuminate for anodic potentials, we can exclude possible inhomogeneities in the illumination as well. Furthermore, the phase waves did not seem to be related to the position of the circular-shaped counter electrode. They existed in stagnant as well as in stirred electrolytes but upon changing the position of the magnetic stirrer, thereby influencing the direction of flow of the electrolyte across the WE, we could observe that the apparent direction of propagation of the phase waves changed. When we increased the rotation speed of the magnetic stirrer the phase waves also became less pronounced. This leads us to believe that the parameter gradient is likely a gradient in the concentration of the etchant species.

It should also be noted that we could measure the oscillations with a rotating disk electrode configuration (AFM-SRCE, Pine Research Instrumentation, Inc.) as well. This was done in a three-electrode set-up in a custom made, gas tight, polymethylmethacrylate (PMMA) cell with two compartments using a 5 mm diameter p-Si disk mounted on a copper cylinder as in the experiments in Ref. [58]. Using the RDE set-up we test yet another geometry, giving rise to yet another transport mechanism of the electrolyte to the electrode surface. However, this set up did not allow for in-situ monitoring of the surface. If we look at the global current density, see Fig. 3.13, we observe a beat like oscillation. This indicated that also with this transport mechanism the dynamics was made up of more frequencies. The long period of the envelope (approx. 2000 s) indicates that the frequencies only differ by roughly 0.5 mHz.

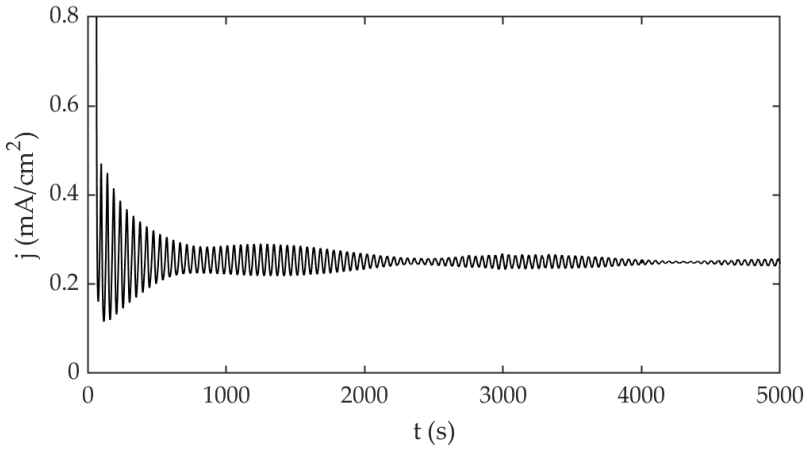

Figure 3.13: Current density, j, in a rotating disc electrode set-up (2000 RPM) with p-Si in a 0.06 M NH_4F solution (pH 1).

Another likely possibility for the parameter gradient appears to be an influence of the insulation border from the silicone seal. Regardless, our interpretation of the waves-like structures as phase waves suggests that under perfectly uniform parameter settings the oscillations would still persist and be uniform.

This means that our experiments present evidence that the anodic oxidation of Si in fluoride containing electrolytes may exhibit autonomous oscillations at high anodic voltages, even when there is no external resistance present. This allows us to investigate spatial self-organisation on the electrode surface in the oscillatory region without the presence of a linear global coupling. The linear global coupling is known to act synchronising for sinusoidal oscillations close to a Hopf bifurcation but might lead to cluster formation if the global coupling function contains higher harmonics [98]. Here we have seen that even without the linear global coupling patterns form on the electrode once the illumination intensity is lowered. At a threshold intensity the electrode splits into domains with distinct temporal behaviour pointing to a spatio-temporal bifurcation induced by a destabilizing action of the spatial coupling. Since the illumination determines the number of electron-hole pairs generated, and at least the first step of the oxidation of Si involves a valence band hole, a change in the illumination intensity affects the spatial coupling through diffusion (or migration) of holes. As long as the oxidation current is limited by the etch rate or, equivalently, by migration of ions through the oxide, the dynamics is insensitive towards fluctuations of the concentration of holes at the silicon silicon-oxide interface. However, when the internal photon flux (i.e. the flux corrected for reflection losses) comes close to the faradaic charge carrier flux, i.e. when the momentary internal quantum efficiency Φ[3] approaches 1, Si atoms in the silicon silicon-oxide interfacial region start to compete for holes. Any lateral hole concentration difference are being translated into both different local hole capture-rates and a lateral hole flux.

For the case where the entire electrode is uniformly illuminated we see that the formation of patterns only took place at relatively low illumination intensities, i.e. when Φ is considerably larger than 1. For example, in the experiment shown in Fig. 3.10, the average value of Φ was approximately 2. Therefore, charge carriers not created through the absorption of a photon must be involved in the oxidation process. Under our experimental conditions, it seems to be most likely that these are valence band holes that are created through tunnelling of valence band electrons into the conduction band. Note that a quantum efficiency larger than 1 during Si electrodissolution in NH_4F electrolyte was reported before but then at low voltages

3 In the following we calculate the internal quantum efficiency at illumination intensity I_{ill} and current density j as $\Phi = jE_{ph} / \left([1-R] \cdot I_{ill}\right)$ and approximate the reflectivity of the electrode for photons with the energy $E_{ph} = 1.96\,eV$ as $R = 0.3$ [28, 110]

where the Si surface is not covered by an oxide [72]. At those voltages the photocurrent multiplication could be explained by the injection of electrons into the conduction band of the dissolving Si atoms. A value of $\Phi \approx 2$ signifies that at least two charge carriers that are not generated through photon absorption are involved in the four-electron oxidation of a Si atom. Despite this change in the hole generation mechanism, the overall rate of oxidation is still the same as at high illumination intensity and the oxide layer (as approximately measured through the ellipsometric intensity) is hardly affected in thickness or quality. These considerations are in agreement with the assumption that the spatial instability is induced by lateral coupling between different parts of the electrode through diffusion and migration of holes (hole-transport induced spatial instability).

At even lower illumination intensities, oscillations and patterns occurred only transiently (cf. Fig. 3.11), the system attaining a steady state with a higher current density. Here, the initial mean current density, which is close to the dry oxide plateau current density beyond U_3, corresponds to $\Phi \approx 2.8$. This value increased to 3.6 at the attained current density. Lowering the illumination intensity changes the photodissolution of Si from etch rate limited to kinetically limited, inducing a feedback loop: a decrease in the hole concentration (due to the lower illumination intensity) slows down the oxide formation rate, disturbing the balance between oxide formation and dissolution in favour of a faster dissolution. This, in turn, results in a thinner oxide layer that promotes the generation rate of charge carriers in the dark, and therewith a higher current density. Hence, we suggest that the steady state current density well above the value of the plateau current at high illumination intensity most likely implies a transition to an oxide free state similar to the one between U_1 and U_2.

This picture is supported by the experiments in which only a circular region of the electrode was illuminated, cf. Fig. 3.12. As long as the illumination intensity was high enough to allow for an internal quantum efficiency (related to the mean current density) considerably below 1, phase waves developed within the illuminated circle identical to the ones found when the entire electrode was illuminated. Only when Φ calculated from the mean current approached 1 did the outward flow of holes affect the dynamics inside the illuminated region and concentric waves emerged from the illuminated rim propagating towards the centre. Fig. 3.12 depicts an example with $\Phi \approx 0.9$, where the phase waves were replaced by such a border induced target wave pattern.

It is of interest to look at the relative etch rate and the surface profile of the electrode after a long measurement where only part of the electrode was illuminated. In Fig. 3.14 such a profile, measured as described in Sec. 2.5, along the middle of the electrode is shown.

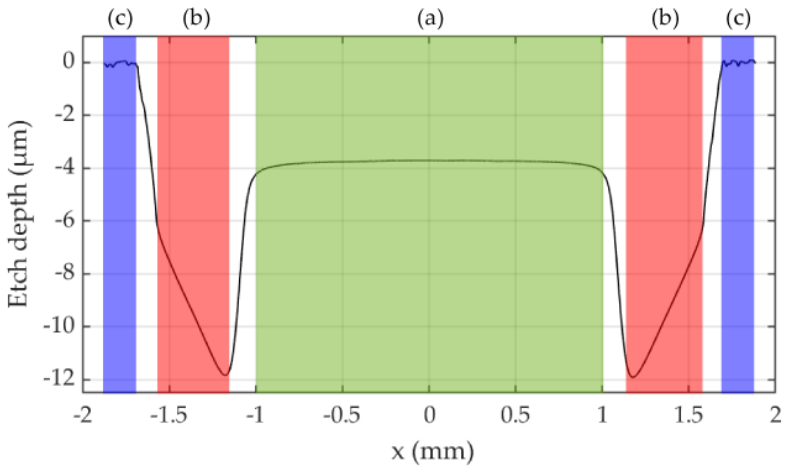

Figure 3.14: Surface profile of the electrode after the measurement shown in Fig. 3.12. The outer regions were used as reference points.

Region (a) (green) shows the approximate region that was illuminated. The profile shows the etch depth relative to a reference point chosen at the outer parts of the electrode. Starting at the centre in region (a) (green) we see the etch depth remains constant throughout this region. It then increases abruptly and is maximal at the beginning of region (b) (red). Within this region the etch depth decreases steadily in radial direction before it abruptly decreases as we leave the region. The outer most region, region (c) (blue), is characterised by its lower etch depth and a rougher surface which also shows macroscopic pores. The rough features in the profile are enhances due to the lateral resolution of the profilometer and do not reflect the size of the pores. The lack in resolution also makes the transitions between the regions appear smoother.

Let us now look closer at the current in the three regions. Assuming that we are in a region where there are enough holes and thus that the current is etch rate limited, then a deeper relative etch depth means a higher etch rate and in consequence a higher average current. Hence, in the illuminated region (a) where the influx of photons is high and there thus is an abundance of holes, the average current is the same at each point in space. In region (b) the amount of holes is limited and depends on the outward flow of holes from region (a) into region (b). Thus, it seems likely that we are in a region where the current is hole limited, resulting in a decrease of the average current in radial direction within region (b). This matches the decrease in etch depth within region (b). In region (c) the correlation between the measured etch depth and the average current no longer holds due to the rough surface and macroscopic pores.

The sharp increase in etch depth as we transition from region (a) to region (b) might at first seem surprising, how can the average current increase with a decreasing amount of holes? Recall the transition

shown in Fig. 3.11. There too, a decrease in illumination intensity leads to an increase in current density. Most likely this happens since there are not enough holes left to uphold a stable oxide layer. The oxide layer is thus etched away and the reaction at the oxide free surface yields a higher current density.

With this in mind we can correlate the different regions on the surface of the partially illuminated electrode to different parts of the CV, cf. Fig. 3.1. Region (a), behaves as the electrode does when it is uniformly illuminated with a high intensity, i.e. it has the same local dynamics as the one found in region II in Fig. 3.8. Further out along the profile, but still in region (a), the electrode does not oscillate any more, cf. Fig. 3.12, but still has the same average etch rate and current density. This means that we have suppressed the oscillations without changing the average current density, so-called amplitude death [121]. Hence, we speculate that the local dynamics here is similar to the one found in region I-a in Fig. 3.8. As we move further out along the electrode surface and transition from region (a) to region (b) we see the abrupt change in etch depth and hence in current density. As mentioned, this is probably due to the lower hole concentration that is likely to locally lead to the same kind of transition as in Fig. 3.11. Hence, we can assume that the final local state in this region is the same as the one in 3.11. As mentioned above it does not seem too far fetched to assume that we have a local dynamics that is similar to the one on the left branch of the CV between U_1 and U_2. This would mean that the local dynamics are now restricted by the local hole concentration. Hence, assuming that the hole concentration decreases in radial direction, our hypothesis is strengthened by the decrease in etch depth (and current density) in radial direction within region (b). The further out we come in region (b) the fewer holes and thus a lower current density on average meaning that less of the electrode has been etched away. Taking it one step further it seems plausible that the local dynamics in region (c) is similar to the one at U_1, seeing as both form macroscopic pores, thus corroborating our hypothesis again. Note, however, that a change in illumination intensity is not trivially linked to a change in potential drop across the electrode and that this mapping of local dynamics to the fundamental behaviour in the highly illuminated case is speculative.

3.4 CONCLUSION

In this chapter we have discussed two main findings, the stability of the NDR branch and the stability of oscillations without a global coupling.

We confirmed that the NDR branch is indeed stable which allowed for a steady-state measurement of the dissolution valency. The dissolution valency was found to increase slightly in this region. We found

that any secondary reaction resulting in H_2O_2 production does not have enough impact to affect the measured valency appreciably. The overall increase in the dissolution valency is minor and might not suffice to confidently claim that it is the main reason for the NDR but it at least suggests that the model presented by Salman et al. [120] is plausible.

We demonstrated that, contrary to what was previously thought, the electrodissolution of Si may exhibit autonomous oscillations which are stable over several hours without an external series resistance or a limited current. This means that we could eliminate the presence of the global coupling mediated through the external control that had been present in all previously published pattern formation experiments. We could then exploit the illumination intensity as a bifurcation parameter and conclude that patterns emerge when the illumination intensity is lowered. Specifically, patterns emerge when the illumination intensity is so low that the photon flux and the resulting current yield an internal quantum efficiency $\Phi > 1$. In contrast to previously published patterns found in the Si electrodissolution system, the ones presented here do not involve illumination limited current plateaus and are found at different parameters. Yet, the electrode splits into different domains with distinct dynamics, similarly to the patterns reported in the literature. The patterns found here include states reminiscent of chimera patterns, their mechanism of formation being one of the crucial questions in nonlinear dynamics.

Hence, we have demonstrated that the spatial coupling through valence band holes seems sufficient to cause the emergence of coexistence patterns, which is a first step towards the elucidation of the properties of the spatial coupling.

4

ADAPTIVE COUPLING AND MULTIFREQUENCY CLUSTERS

Having established the most fundamental behaviour of our system in the previous chapter, we now turn our attention to a more detailed investigation regarding the emerging complex spatio-temporal behaviours. Since we now know that the movement of holes parallel to the surface can constitute a nonlocal, spatial coupling we can take a closer look at the impact of the strength of this coupling on the dynamics. In this chapter, we specifically investigate the emergence of self-organised multifrequency clusters from a uniform oscillatory state when reducing the illumination intensity.

In the last chapter we noted that the effect of the reduced illumination and the coupling that it introduces depends on the internal quantum efficiency which in turn depends on the value of the current density. We also saw that the system exhibits phase waves when there is no external resistance. The phase waves yield a lower current amplitude than when the electrode oscillates in a uniform state. In addition, the formation of phase waves also means that the oscillation amplitude of the current density depends on the length of the measurement. To combat this inhomogeneity and ensure a reproducible initial state for our investigation of the patterns we add a small external resistance in series with the electrode—remembering the finding that the external resistance is not necessary for the oscillations. The external resistance acts as a global synchronizing force on the dynamics [61] and results in spatially uniform oscillations with an amplitude that does not change with the length of the measurement. Hence, there are now two dominant types of coupling present, a global synchronising coupling and a long-range coupling through diffusion and migration of valence band holes. Below we will argue that their interaction creates a *nonlinear*, nonlocal coupling that, in turn, promotes the formation of multifrequency clusters.

The results in this chapter were in part published previously in Ref. [108].

4.1 BACKGROUND

At this point it is worth reminding ourselves that much of the dynamics of oscillating systems as diverse as neural activities [38], electrical power grids [5], multi-mode lasers [78], and Josephson junction arrays [154] can all be understood within the common framework of networks of coupled oscillators. These diverse applications render the study of coupled oscillators an important discipline of nonlinear dynamics. The overwhelming majority of previous studies consider the case of a linear coupling. Only recently, the more general case of nonlinear coupling has received increasing attention [20, 56, 87, 116, 122, 123, 125, 130, 142, 143]. It could be shown that this generalization can produce genuine nonlinear coupling features. For example, the case of global nonlinear coupling has been found to produce self-organised quasi-periodicity in ensembles of phase-oscillators [116], complex chimera states composed of (nearly) synchronised regions of different mean frequencies and incoherent regions [20], or a variety of coexistence patterns, including again chimera states [122, 123, 125, 130]. Another representation of nonlinear coupling is realised in networks of Kuramoto oscillators that are designed to mimic adaptive neural networks [115]. In this type of model, recent studies predict the emergence of multifrequency clusters even when the oscillators are identical [15, 16, 54]. Until then, the existence of multifrequency clusters was always linked to heterogeneous oscillatory systems with some distribution of the natural frequencies [85, 90, 101, 102].

4.2 EXPERIMENTAL FINDINGS

As in the previous chapter, the experiments were conducted with an n-doped (1-10 Ωcm) Si (111) sample as the WE. The electrolyte was our standard aqueous solution, containing 0.06 M NH_4F and 142 mM H_2SO_4. Since we only used spatially uniform illumination we illuminated the electrode with the linearly polarised He-Ne laser, and adjusted the intensity with a linear polarisation filter, see Fig. 2.1.

The experiments were conducted with an applied potential of 4.15 V vs SHE with an external resistor with a resistance such that $R_{\text{ext}}A = 1\ \text{k}\Omega\text{cm}^2$. In this parameter range the oscillation amplitude reacted very sensitively to any perturbation. This implies that the spatial coupling of the oscillatory medium is strong. Here, a strong coupling should be seen in contrast to a weak coupling, where a weak coupling implies that there is a separation of the time scales of the amplitude dynamics and of the phase dynamics. For a weak coupling the amplitude would relax fast, resulting in a pure phase oscillation.

In the measurement presented below the applied voltage and the external resistance were held at constant values and the illumination intensity is used as our bifurcation parameter.

Starting from an oxide free state at OCP we initialised the electrode in a spatially homogeneous state via a potential step from OCP to a constant applied voltage $U_{app} = 4.15$ V vs. SHE at a high illumination intensity. We then decreased the illumination intensity step by step. At each step, we waited until transients had died out and then measured the dynamics for 10^3 s.

Let us start with a brief overview of the dynamics at different illumination intensities before looking at them in more detail. In Fig. 4.1 (a) the initial state at a high illumination intensity is presented.

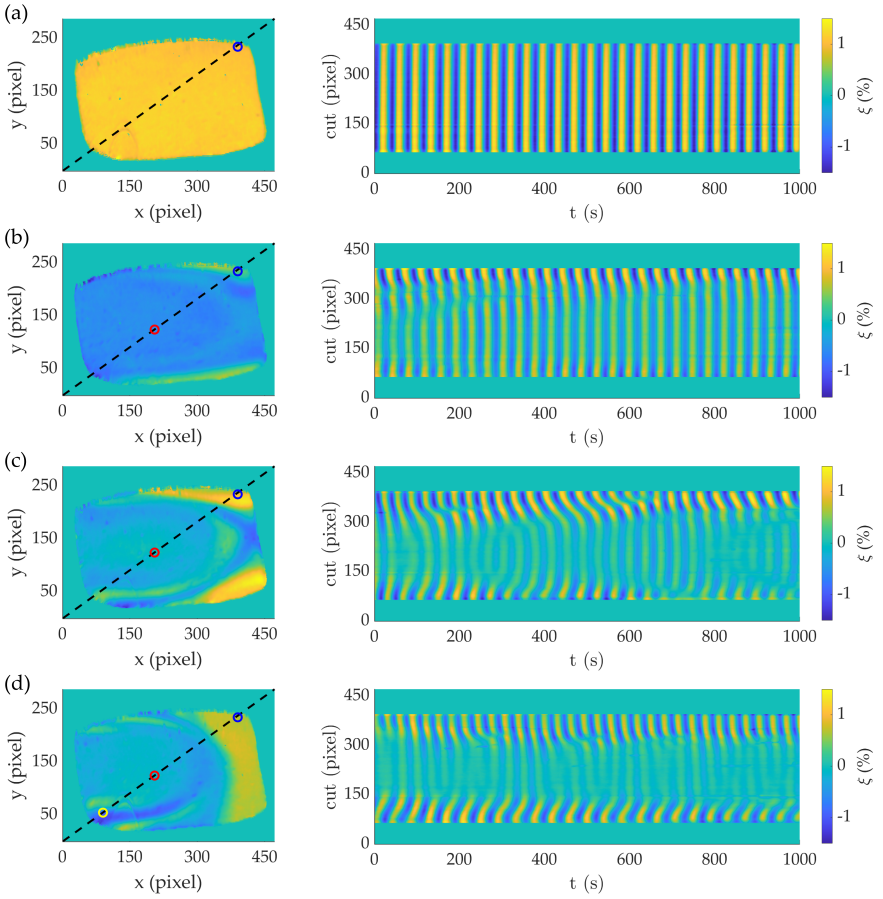

Figure 4.1: Dynamics found at four different illumination intensities: (a) $r = 5.97$ mW/cm^2, (b) $r = 0.95$ mW/cm^2, (c) $r = 0.80$ mW/cm^2, and (D) $r = 0.73$ mW/cm^2. Left: snapshot of the ellipsometric intensity $\xi(\mathbf{x}, t = 807\ s)$. Right: 1D spatio-temporal plot along the respective dashed lines on the left. Electrode size: $A = 12.19$ mm^2. n-Si, $U_{app} = 4.15$ V vs. SHE, pH 1, $c_F = 0.06$ M.

The state is spatially uniform. In the 1D spatio temporal cut on the right in Fig. 4.1 (a) we can see that the ellipsometric intensity is not only spatially homogeneous at one instance in time but changes with the same frequency along this exemplary cut. All in all it can be seen that at a high illumination the oscillation is very ordered: it is spatially

homogeneous and the oscillations are periodic with one clear main frequency.

Here we should make a short detour back to the state shown in Fig. 3.7 (b). Both the state presented here and the one presented in the previous chapter are measured at high illumination and with similar applied potentials. The main difference in the experimental conditions between the two measurements is that here we have placed an external resistor with a small but significant resistance in series with the WE. This results in the difference in the outcome between the state with the phase waves and this nicely ordered state, cf. Ref. [129, 130]. This ordered state does, however, change when we lower the illumination intensity.

Going back to the measurement at hand, we look at Fig. 4.1 (b) where the illumination intensity has been reduced. We see that a spatial symmetry breaking has occurred and that there are regions that oscillate with a higher amplitude and others that oscillate with a lower amplitude. This can be seen more clearly when looking at the cut in Fig. 4.1 (b) where the amplitude in the more central part of the 1D-cut has been suppressed compared to the state in Fig. 4.1 (a) whereas the upper right corner preserves approximately the same amplitude as before. So far, the oscillation takes place with the same frequency on the entire electrode.

When lowering the illumination further we note that different regions start to oscillate with different frequencies, see Fig. 4.1 (c). Fig. 4.1 (c) shows that the electrode does not only exhibit regions with different amplitudes but when looking at the 1D-cut it can also be seen that the upper right region has a higher frequency than the rest of the electrode. Lowering the illumination even further (Fig. 4.1(d)) we observe that the features from the state in Fig. 4.1(c) become even more pronounced.

The difference in frequency becomes especially clear when comparing the upper and lower part of the plot of the 1D-cut (Fig. 4.1 (d)). Here pixels in the upper part complete almost 4 oscillations per 3 oscillations that pixels in the lower part complete. Furthermore, it is also worth noting that the amplitude of the oscillations have been suppressed in the middle of the electrode to such an extent that any changes in the amplitude are effectively below our detection limit.

In order to better distinguish any features in the regions with lower amplitude, we filtered the data both in temporal and spatial dimensions as discussed in chapter 2.3.2.

4.3 AMPLITUDE, PHASE, AND FREQUENCY

To better grasp the nature of the dynamics discussed in the last section, we turn to the algorithm for calculating the analytic signal, described in Chapter 2.3.2.

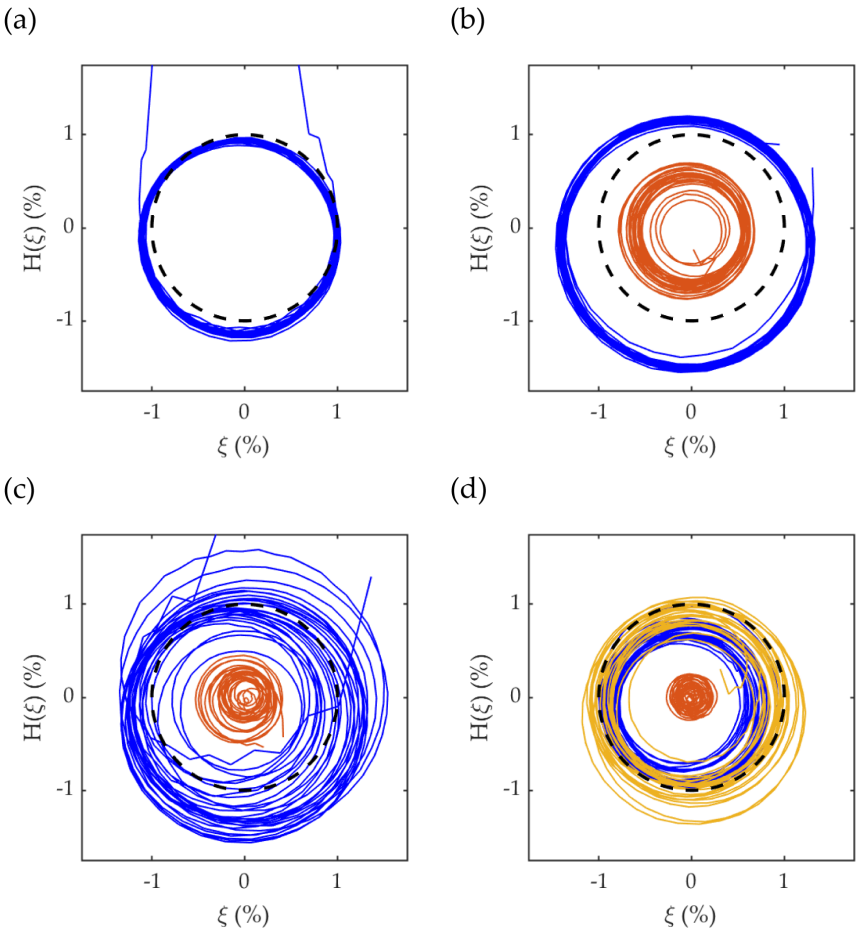

Figure 4.2: Local dynamics of exemplary points marked in Fig. 4.1, same parameters respectively, together with unit circle (dashed).

Let us start with looking at the analytic signal at the exemplary points marked with circles in the snapshots in Fig. 4.1. In Fig. 4.2, we have plotted the analytic signal at these points in the complex plane. As expected the main properties of the states can be found here as well, indicating that this is a reasonable representation. In comparing the first two states, Fig. 4.2 (a)-(b), we can speculate how the amplitude clusters have formed. In Fig. 4.2 (a) the analytic signal plotted in blue, taken at the point marked with a blue circle in the upper right corner of the electrode in Fig. 4.1(a), is a good representation of all points on the electrode. In Fig. 4.2 (b) the amplitude of the analytic signal at this point has increased slightly whereas the amplitude at an exemplary point taken in the centre of the electrode (marked with a red circle in Fig. 4.1 (b)) is clearly smaller, i.e. amplitude clusters have formed. This indicates that the amplitude clusters emerge through a continuous bifurcation, most likely a pitchfork bifurcation. In addition, we can see that the phase portraits are slightly thicker, suggesting the presence of an additional frequency. This is even more clearly visible in the red signal but as we will see below (cf. Fig. 4.5), the dynamics at the blue

point is also modulated. This, suggests that subsequently to the spatial symmetry breaking a Hopf bifurcation took place. In Fig. 4.2 (c) the broadening of the blue signal has increased so much that it is clearly visible in this representation as well. In addition, the red trajectory has decreased in amplitude to the point where we can no longer discern any finer details. This trend continues and in Fig. 4.2 (d) the amplitude of the red trajectory has become even smaller. The blue trajectory has also decreased in amplitude. Considering that we noted a different frequency in the lower left corner at the lowest illumination (cf. Fig. 4.1 (d)) it is also of interest to look at an exemplary point from this region. As can be seen in Fig. 4.2 (d) this point (yellow) has a slightly larger amplitude than the first point (blue). However, it is hard to discern whether the yellow trajectory winds around the origin fewer times than the blue trajectory—thus indicating that the frequencies would be slower—or not.

In order to make a quantitative statement regarding the frequency we have to first take a closer look at the phase.

We start by defining the phase of the analytic signal so that it does not live on a circle but instead on the real line, i.e., we unwrap the phase by adding multiples of $\pm 2\pi$ radians to the angle whenever the phase difference between two consecutive points in time is larger than π radians until the difference is less than π radians. This way of defining the phase allows us to extract the dominant frequency $\nu(\mathbf{x})$ at each point via a linear fit:

$$\phi_{\text{fitted}}(\mathbf{x}, t) = 2\pi\,\nu(\mathbf{x})\; t + \alpha, \tag{4.1}$$

where α is a free fitting parameter

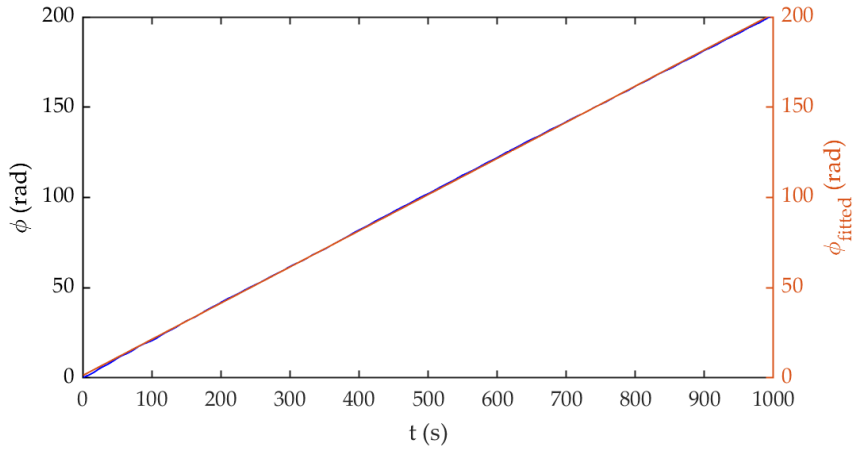

Figure 4.3: Local unwrapped phase (blue) with linear fit (red).

In Fig. 4.3 the phase of an exemplary point is shown together with the linear fit. Note that this way of determining the frequency is not necessarily the same as taking the average of the instant frequencies.

Defining the instant frequency as the difference in phase of two consecutive points in time and dividing the difference by the length of the time step Δt, we see that the average of the instant frequencies would be:

$$\bar{f} = \frac{1}{N_T} \sum_{i=1}^{N_T} f_i = \frac{1}{N_T} \sum_{i=1}^{N_T} \frac{\phi_i - \phi_{i-1}}{\Delta t} = \frac{\phi_{N_T} - \phi_0}{T}, \tag{4.2}$$

where N_T is the number of points in the time series and T is the total duration of the time series. This would, in other words, be equivalent to taking the total change in the phase and dividing by the total elapsed time. This can capture the dynamics fairly well and is an easy way of describing the dynamics under the assumption that the frequency remains constant during the entire time series, that the noise is low, and that the length of the time series is a multiple of the oscillation period. If on the other hand the frequency changes, the first and/or the last recorded point deviates from the rest of the time series due to noise, or the length of the time series does not match the average period, then the average frequency method as defined here is ill suited. With this in mind we use the dominant frequency $\nu(\mathbf{x})$ obtained from Eq. (4.1).

Having determined the time-series of the amplitude and of the phase as well as the dominant frequency at each point we now return to the exemplary states from Fig. 4.1 and look at the dynamics on the entire electrode again.

In Fig. 4.4 the temporally averaged amplitude $\overline{A(\mathbf{x}, t)}$, the dominant frequency $\nu(\mathbf{x})$, and a snapshot of the phase at an arbitrary instant in time, $\phi(\mathbf{x}, t = 807\,\mathrm{s})$, are shown in the first, second, and third column respectively. As before, the four rows depict measurements at four different illumination intensities. The initial, highly illuminated state is shown in Fig. 4.4 (a). Here, we again see that the system oscillates uniformly with the same amplitude, frequency, and phase at each point in space.

Upon lowering the illumination intensity, Fig. 4.4 (b), the average amplitude on the electrode splits into a region with higher and a region with lower amplitude. These two regions still oscillate with the same average frequency, but the oscillation phase differs between points in the higher- and lower-amplitude regions. In other words, we can confirm that amplitude clusters have formed.

However, the data shown in Fig. 4.4 (b) does still not give the full picture of the dynamics. This can be seen if we look at Fig. 4.5. Here, the temporal evolution of the phase at an exemplary point, marked by a cross in the phase plots in Fig. 4.4 (a) and (b), is depicted in a frame rotating uniformly with the dominant frequency of the point in question. Starting with the higher illumination (Fig. 4.5 (a)) we observe only a simple modulation with the same dominant frequency

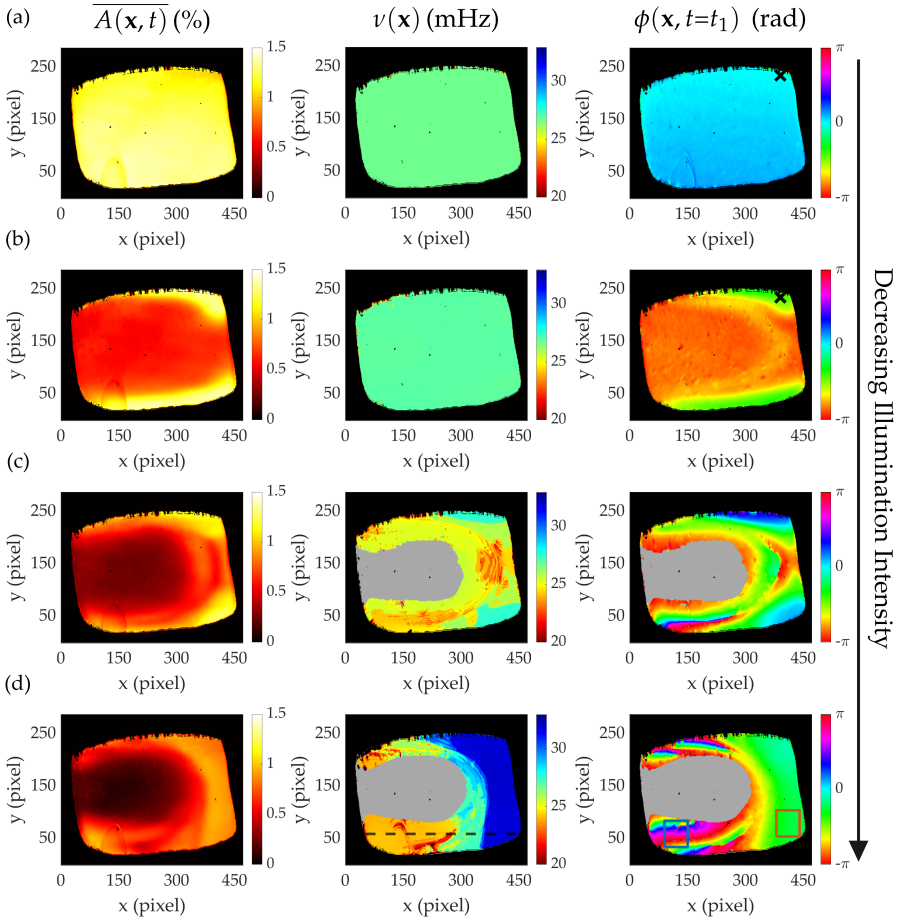

Figure 4.4: Experimentally measured spatial distribution of the temporal average of the amplitude, $\overline{A(\mathbf{x},t)}$, of the dominant frequency $\nu(\mathbf{x})$, and of the phase $\phi(\mathbf{x},t=t_1)$ at $t_1 = 807$ s at four different illumination intensities: (a) $r = 5.97\,\mathrm{mW/cm^2}$, (b) $r = 0.95\,\mathrm{mW/cm^2}$, (c) $r = 0.80\,\mathrm{mW/cm^2}$, and (d) $r = 0.73\,\mathrm{mW/cm^2}$. Electrode size: $A = 12.19\,\mathrm{mm^2}$.

as the one of the rotating frame. This can also be seen in Fig. 4.5 (c) where the absolute value of the Fourier transform of the time series in (a) is shown. Here a clear peak can be seen at 27 mHz. This peak corresponds to the super-harmonic peak in the original frame of reference which in turn can be seen due to the fact that the oscillation is slightly relaxational. The reason why this frequency can be seen in the co-rotating frame of reference is that when we move into a co-rotating frame of reference the entire frequency spectrum is shifted to lower frequencies. This means that that the point of the spectrum that corresponds to the rotational frequency ν is now at 0 Hz. In the same way a point in the spectrum at 2ν will be shifted to ν.

In the case with the lower illumination (Fig. 4.5 (b) and (d)), when the amplitude clusters have formed, we observe a further slow modulation of the phase evolution with a frequency of approximately 2 mHz. This supports our conjecture from above that the system not only

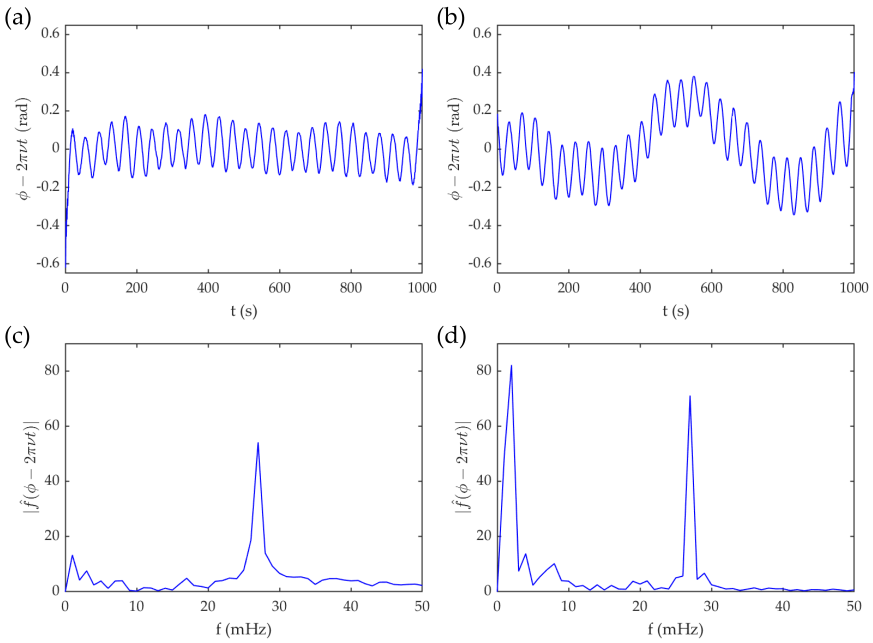

Figure 4.5: (a) and (b): Time series of the local phase in a frame rotating with the respective dominant frequency ν. Time series taken at the point marked by a cross in the ϕ snapshot in Fig. 4.4 (a) and (b) respectively. (c) and (d): Absolute value of the fast Fourier transform of the time series in (a) and (b) respectively.

underwent a pitchfork bifurcation leading to amplitude clusters but also a secondary Hopf bifurcation creating the modulated oscillations.

When lowering the illumination further, two drastic changes in the dynamics can be seen in Fig. 4.4 (c). First, we observe that the mean amplitude differentiates further in space, suppressing the oscillations nearly completely on a part of the electrode. In this region, the very small amplitude combined with experimental noise leads to apparent discontinuities in the phase, rendering the determination of the dominant frequency impossible. Therefore, in the second and the third row of Fig. 4.4, we depict points with $\overline{A(\mathbf{x}, t)} < 0.35\%$, in grey. Second, focusing our attention on the region that exhibits well defined oscillations, $\overline{A(\mathbf{x}, t)} > 0.35\%$, we can confirm our suspicion from above that the dominant frequency is not uniform any more. Rather, the frequencies appear to accumulate around three plateau values, as apparent from the turquoise, red, and yellow patches in Fig. 4.4 (c), whereby the higher frequencies are found in the regions with higher mean amplitude.

In the last state, Fig. 4.4 (d), the features that appeared in Fig. 4.4 (c) become more pronounced; on a part of the electrode the amplitude is practically completely suppressed. In other words, on this part of the electrode we observe amplitude death [57]. Likewise, the frequency differences across the oscillating part of the electrode become more pronounced. Equal, or at least very similar frequencies now

appear in connected regions, whereby the frequency distributions of the two outer orange and blue regions are very narrow, and the frequency distribution of the middle, 'mediating' region is somewhat broader, ranging from light-blue to yellow. Indeed, we witness the self-organised formation of multifrequency clusters in a homogeneous oscillatory medium.

Considering the snapshot of the phase distribution, we observe that there is also a difference in the phase distribution between the faster and the slower region. In Fig. 4.6 (a) the phase distribution of the pixels within the blue box marked in the phase snapshot in Fig. 4.4 (d) is shown for $t = 807$ s. Here, we observe a travelling-wave-type feature; a continuous distribution of the phases over 2π rad. This is not the case in the faster oscillating region (red box) on the right in Fig. 4.4 (d) (Fig. 4.6 (b)). Here, the phases gather around approximately -1 rad and we can say that the phases of the oscillations are almost completely synchronised. Each pixel within this region has approximately the same phase at any given time. Note that there are the same amount of points in the two boxes.

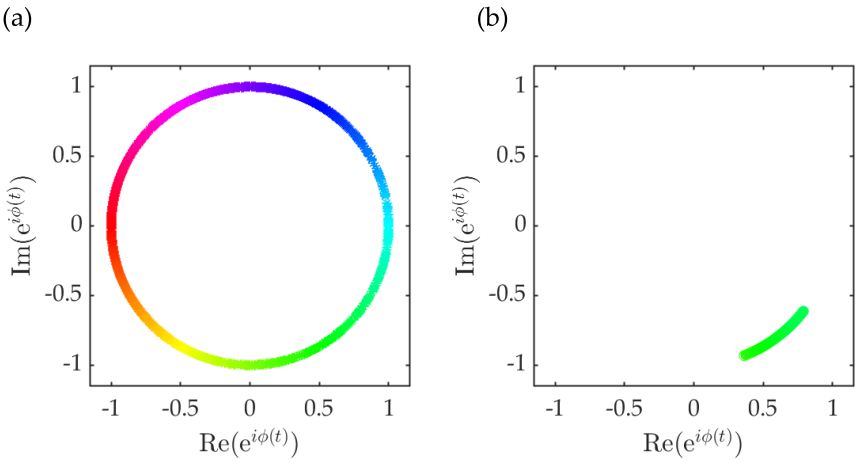

Figure 4.6: Phase dynamics at $t = 807$ s in regions marked with the red box (a) and the blue box (b) in the phase snapshot in Fig. 4.4 (d), both regions contain 3111 pixels.

The state of synchrony of the phase dynamics can be measured by using the Kuramoto order parameter R defined as:

$$R(t) = \left| \frac{1}{N} \sum_{j=1}^{N} e^{i\phi_j(t)} \right| , \tag{4.3}$$

for an ensemble of N oscillators. When the oscillators in an ensemble are synchronised, in the sense that they all have the same phase at the same time, $R(t) = 1$. In the opposite case, when the phases of the oscillators are equally distributed over 2π for all times, $R(t) = 0$. We now define different regions of our electrode depending the local

dominant frequency ν and calculate $R(t)$ for the different regions, see Fig. 4.7.

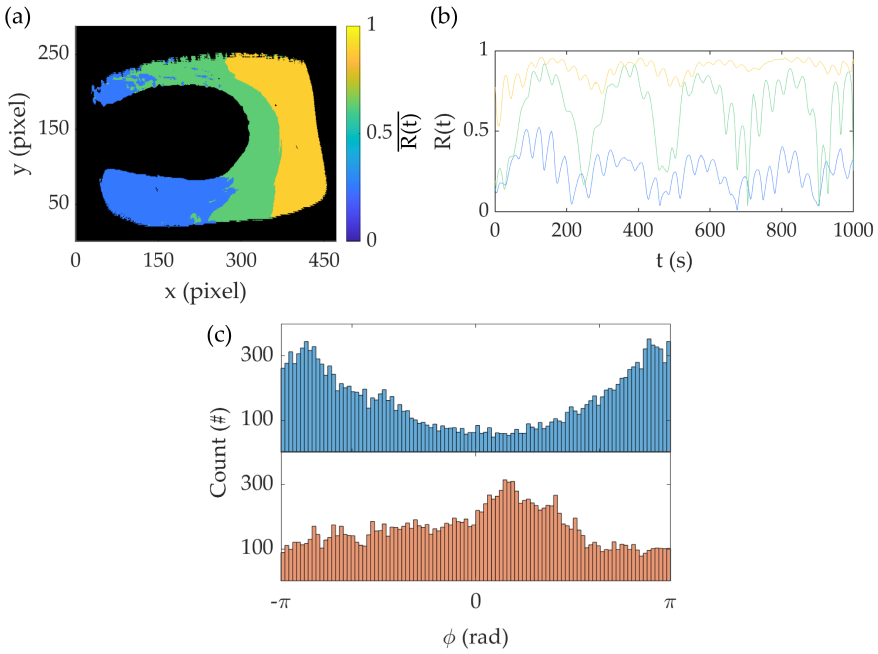

Figure 4.7: (a) Spatial plot of temporal average of the order parameter $|R(t)|$ of the phase only representation of the dynamics taken locally in regions defined by their respective frequencies. Blue region: $\nu \leq 24.5$ mHz, green region: $24.5 < \nu \leq 31$ mHz, yellow region, $\nu > 31$ mHz. (b) Temporal evolution of $R(t)$ in the three different regions (same colour respectively) and temporal evolution of global $R(t)$ (black). (c) Histogram of phases in the blue region in (a) where $\nu \leq 24.5$ mHz, taken at $t = 807$ s (blue) and at $t = 786$ s (red), bin width $\pi/50$ rad.

In all three regions we see that R oscillates slowly and that the slow oscillation is modulated by a faster frequency. The faster modulation frequency approximately matches the main frequency in the respective region. Neglecting the modulations we see that for the faster region on the right hand side of the electrode with $\nu > 31$ mHz the slow oscillation in $R(t)$ is around an average of ≈ 0.9 showing that the phases are almost perfectly synchronised. The oscillating behaviour is even more visible in the mediating region with $24.5 < \nu \leq 31$ mHz. Here, $R(t)$ changes slowly between approximately 0.1 and approximately 0.9 indicating that the phases change between being almost completely synchronised to having an almost uniform distribution. In the slowest region on the left, $R(t)$ oscillates around ≈ 0.25, indicating that the phases are on average spread out.

The value of $R(t)$ does not reach 0 since that would require a perfectly uniform distribution of the phases over a 2π interval and as can be seen in the histograms in Fig. 4.7 (c) this is not the case here. The upper histograms show the phase distribution within the slower

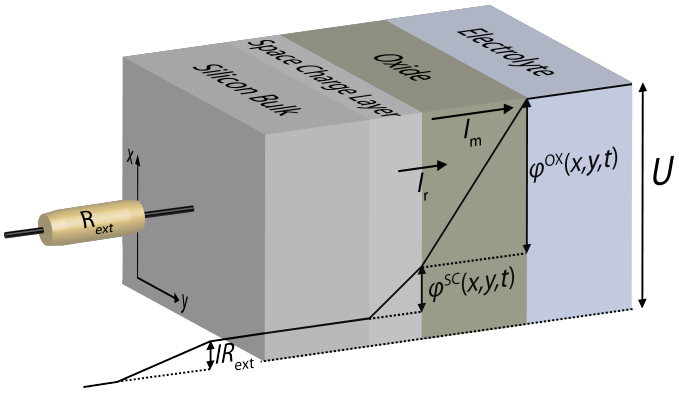

Figure 4.8: Sketch of the different layers of the electrode-electrolyte interface (not to scale) and the potential drops across the different interfacial layers as well as across the external resistor. I_r, reaction current; I_m, migration current of ionic species through the oxide layer. Same x and y as in Fig. 4.4. For the other symbols, see text.

region ($\nu \leq 24.5$ mHz, blue region in Fig. 4.7 (a)) at the time of the snapshot of the phase in Fig. 4.4 (d), i.e $t = 807$ s). The lower histogram is taken at time $t = 786$ s which is approximately half a period earlier for an oscillation with a frequency of 24 mHz. Comparing these we can see that the distribution changes in that the former minima become maxima and vice versa. This indicates that it is the finite size of the region that leads to a non-zero $R(t)$. This together with the borders between the different frequency regions not being as sharp as suggested by Fig. 4.7 (a) results in the oscillating behaviour of $R(t)$ in this low-frequency region.

The travelling-wave-type feature that we observe in the slower region can be seen as the continuum version of a splay state in networks of coupled oscillators. Interestingly, the existence of mixed-type multifrequency clusters consisting of a splay-type cluster and a phase-synchronised cluster, as we observe it here, has also been found in simulations of networks of phase oscillators with adaptive coupling [15, 16, 54].

4.4 NONLINEAR, NONLOCAL COUPLING

Now to the question how these states can emerge: what leads to the spatial symmetry breaking?

A key to understanding the changes in the dynamics is to realise that our bifurcation parameter controls the effective number of degrees of freedom in the system.

First, consider the sketch of the working electrode and the different potential drops across the cell, depicted in Fig. 4.8. The silicon-electrolyte interface is composed of the bulk silicon, the silicon space charge layer, the oxide layer, and the double layer (not shown). The constant applied voltage U splits into the potential drops across the

external resistor IR_{ext}, the space charge layer $\varphi^{\text{SC}}(\mathbf{x},t)$, and the oxide $\varphi^{\text{OX}}(\mathbf{x},t)$ while, to a first approximation, the drops on the electrolyte side and across the bulk silicon can be neglected.

The reaction resistance across the silicon silicon-oxide interface is, to a large part, determined by the concentration of holes n_h. Hence, at high illumination intensities, where there is an excess of valence band holes, this reaction resistance is small. In comparison the resistances across the oxide and the external resistor are large and hence they limit the total current I. In this situation we observe uniform base oscillations. Moreover, any oscillations in the current lead to an oscillating potential drop across the external resistor IR_{ext} and the oxide φ^{OX} while, owing to the nearly constant concentration of holes, the potential drop across the space charge layer φ^{SC} remains constant.

This means that the oscillations are synchronised by a global coupling arising from the presence of the external resistor and the potentiostatic control:

$$\begin{aligned}\varphi^{\text{SC}}(\mathbf{x},t)+\varphi^{\text{OX}}(\mathbf{x},t) &= \\ &= U - R\int\limits_{\mathbf{x}'\in A} i\left(\varphi^{\text{SC}}(\mathbf{x}',t),\varphi^{\text{OX}}(\mathbf{x}',t)\right)\,d\mathbf{x}'.\end{aligned} \tag{4.4}$$

Here, $\varphi^{\text{SC}}(\mathbf{x},t)$ and $\varphi^{\text{OX}}(\mathbf{x},t)$ are the potential drops across the space charge layer of the silicon, and the silicon-oxide layer respectively, U is the applied voltage, R is the external resistance, A is the electrode area, and i is the local current density. The last term in Eq. (4.4) describes the potential drop across the external resistor which depends on the total current. Note that the right hand side of Eq. (4.4) does not depend on space whereas the left hand side does. This is possible since we have two degrees of freedom on the left hand side; φ^{SC} and φ^{OX} can both change. In this way they can both vary in space as long as the sum of them is constant. Since at high illuminations $\varphi^{\text{SC}}(\mathbf{x},t)$ remains constant in space and time, the oscillating total current causes spatially homogeneous oscillations in $\varphi^{\text{OX}}(\mathbf{x},t)$, which in turn influence the reaction rate and thus the oscillations. Hence, our electrochemical oscillator creates a mean field

$$I = \int\limits_{\mathbf{x}'\in A} i(t)\,d\mathbf{x}', \tag{4.5}$$

that feeds back into the dynamics of the oscillations.

However, as the illumination intensity is reduced things change. There is no longer an excess of holes since now the hole production rate and the reaction rate become of the same order, and thus the reaction resistance becomes larger. As a consequence, φ^{SC} increases at the expense of the other potential drops and the oscillations in I now lead also to oscillations in φ^{SC} and n_h.

Spatial fluctuations in $\varphi^{\text{SC}}(\mathbf{x},t)$ and $n_h(\mathbf{x},t)$ lead to changes in the local current density. Moreover, they induce lateral motion of holes

which is determined by the gradient of the electrochemical potential of n_h, i.e. the combination of the differences in the concentration of holes and in the electrical field.

We can write an expression for this lateral motion of the holes by considering the following continuity equation. The change in hole concentration n_h with time has to depend on the generation rate G, the recombination rate R and the divergence of the hole flux div $\mathbf{j}$:

$$\frac{\partial}{\partial t} n_h = G - R - \operatorname{div} \mathbf{j}. \tag{4.6}$$

If we now write the hole flux as a function of the conductivity of the holes $\sigma_h = n_h b_h e$ (b_h is the hole mobility and e is the elementary charge) and the electrochemical potential of the holes $\tilde{\mu}_h = \mu_h - e\varphi$ (μ_h is the chemical potential of the holes and φ is the electrostatic potential) we find that:

$$\mathbf{j} = -\frac{\sigma_h}{e^2} \operatorname{grad} \tilde{\mu}_h = -\frac{n_h b_h}{e} \operatorname{grad} \left(\mu_h - e\varphi\right). \tag{4.7}$$

Next, we use the expression for the electrochemical potential at room temperature in the bulk of the semiconductor and find that:

$$\begin{aligned} &\operatorname{grad} \left(\mu_h - e\varphi\right) = \\ &\quad = \operatorname{grad} \left(\mu_0 + k_B T \ln \frac{n_h}{N_h} + e\varphi\right) \\ &\quad = \operatorname{grad} \mu_0 + \frac{k_B T}{n_h} \operatorname{grad} n_h + e \operatorname{grad} \varphi, \end{aligned} \tag{4.8}$$

where $k_B = 8.617 \cdot 10^{-}5$ eV/K is the Boltzmann constant, N_h is the effective density of states in the valence band and μ_0 is the standard chemical potential.

Combining these expressions we then find that Eq. (4.6) becomes:

$$\frac{\partial}{\partial t} n_h = G - R + \frac{b_h k_B T}{e} \Delta n_h + b_h \operatorname{\mathbf{div}} \left(n_h \operatorname{grad} \varphi\right), \tag{4.9}$$

where we have assumed that the chemical environment is constant and that hence, μ_0 does not change in space. This is the familiar form of a reaction diffusion equation with an additional nonlinear term. Hence, it becomes clear that the coupling which depends on both n_h and φ is nonlinear. These quantities then feed into the mean field I which, as mentioned above, changes φ according to Eq.(4.4) and thus feeds back into the dynamics of the oscillations again, underlining the nonlinearity once more. Note that φ in the space charge layer is determined by Poisson's equation, meaning that the nonlinear term also contains a nonlocal aspect: It entails an instantaneous redistribution of the electrostatic potential in the entire layer upon any change in the charge density.

The solution to Eq. (4.9) of course depends on the boundary conditions.

The generation rate G can be assumed to be constant and is determined by the net influx of photons, i.e. the amount of electron-hole pairs that are generated depends on the illumination intensity and the reflectivity of the electrode surface. The exact form of R is not known. It does however seem reasonable that it depends on the applied potential; an increased applied potential would lead to a different recombination rate due to a higher electric field which in turn would drive more holes towards the surface.

To sum up, we have a base oscillator at high illumination that creates a global field, the total current I. At lower illumination intensity the concentration of holes n_h becomes an additional degree of freedom which induces a spatial, nonlocal coupling and feeds back to the mean field I in a nonlinear manner. Thus, the dynamics can be formally described by the following equations:

$$\dot{\mathbf{w}}(\mathbf{x},t) = \mathbf{F}\left[\mathbf{w}(\mathbf{x},t), n_h, I; \lambda\right], \tag{4.10}$$

$$\dot{n}_h = G\left(n_h, \varphi^{\mathrm{SC}}, I; \lambda\right). \tag{4.11}$$

Here $\mathbf{w}$ are the variables of the base oscillator and the dots indicate the derivative with respect to time. At high illumination intensity λ, n_h remains constant and the function F in Eq. (4.10) represents the dynamics of the base oscillator. Equation (4.11) becomes relevant at low illumination intensity and depends on the mean field I that is created by the base oscillator.

If we consider our spatially continuous system as being composed of infinitesimally small base oscillators $\mathbf{w}_k$, one realises that the nonlinear coupling is of the same type as the general physical setting for nonlinearly coupled oscillators formulated by Rosenblum and Pikovsky [116] [compare Eqs. (4.10) and (4.11) to Eq. (18) in [116]). While in Ref. [116] the nonlinear coupling constituted a strictly global coupling, later a nonlinear and nonlocal coupling was considered [20]. Interestingly, the nonlinear, nonlocal coupling supported states with three synchronised regions, each oscillating with a different frequency. In this respect, these states have a high similarity to our multifrequency clusters. However, in addition to these synchronised 'frequency clustered' regions the states described in Ref. [20] also contained a large incoherent domain rendering the states chimera states.

4.5 CHIMERA STATES AND COEXISTENCE PATTERNS

Adopting a different perspective, one realises that our dynamics also contain features that have been discussed in connection with certain types of chimera states. Fig. 4.9 presents a purely global picture of the dominant frequencies found in the states presented in Fig. 4.4.

Here we have sorted the frequencies in ascending order, neglecting any spatial information.

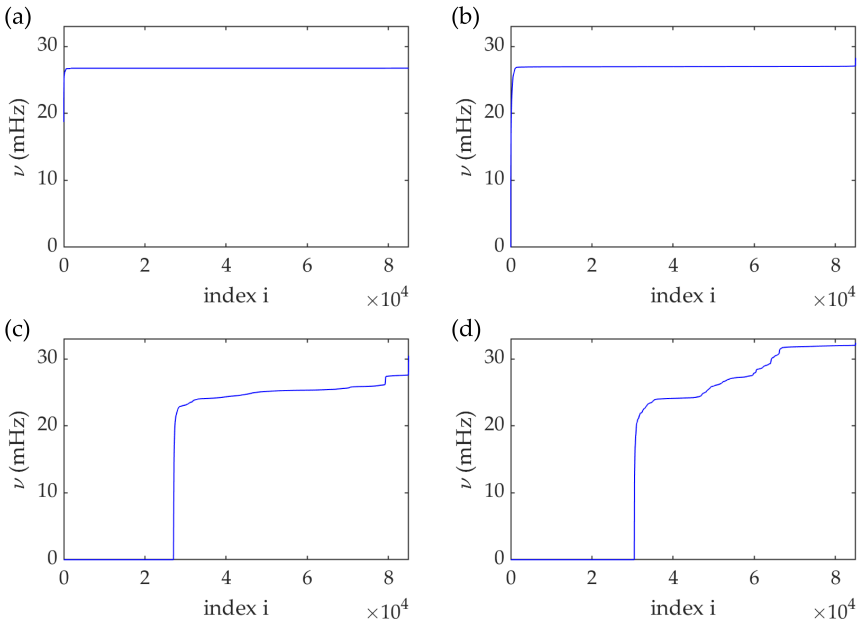

Figure 4.9: The dominant frequencies ν from Fig. 4.4 sorted in ascending order with (a)-(d) corresponding to (a)-(d) in Fig. 4.4

Again, we can see that for the first two states the frequency is uniform and that it splits up for the state shown in Fig. 4.9 (c) before becoming more pronounced in Fig. 4.9 (d). Focusing on the multifrequency state in Fig. 4.4 (d), the first about thirty thousand entries with the value 0 Hz arise from the region where we observe amplitude death. For higher indices, we clearly observe three plateaus. These reflect our three frequency domains. However, the transitions between these plateaus are not sharp but instead occur continuously in a finite index range. As such, this graph is reminiscent of the distribution of dominant frequencies in 2-frequency chimera states [30, 91, 141], and to some extent also of the ones in the hybrid chimera states found in Ref. [20], which are composed of a fully synchronised, a nearly-synchronised, and an incoherent part.

Another study reveals an additional link between multifrequency clusters and chimera states [114]. In this study a birhythmic model of two-frequency oscillators on a ring was considered. When coupling these oscillators nonlocally, synchronised domains oscillating in either of the two bistable limit cycles could be stabilised. The interfacial regions mediating between the domains with different frequencies oscillated asynchronously with frequency components of both adjacent regions. The author interpreted her two frequency-domains separated by a 'more frequency' incoherent region as a chimera state.

Our multifrequency cluster exhibits the same features. This can be seen in Fig. 4.10 (a) where we present the absolute value of the

Fourier coefficients of the three main frequencies, 24 mHz, 27 mHz, and 32 mHz, of the local Fourier spectra along a the dashed line in the ν plot in Fig. 4.4 (d). While in the left low- and the right high-frequency regions the contribution of the other two frequencies are very small, in the middle region we find not only the third, dominant frequency at 27 mHz, but also a significant contribution of the frequencies of the two adjacent regions, just as in the model system in Ref. [114].

This can be seen in more detail in Fig. 4.10 (b) where histograms of the instant frequencies f_i as defined in Eq. 4.2 at three different points along the cut are shown. The point in the slow region that oscillates with a dominant frequency $\nu = 24$ mHz and the point in the fast region with $\nu = 32$ mHz both give narrower, unimodal distributions of f_i with the maxima at approximately the value of the dominant frequency, respectively. The point in the middle region on the other hand gives a much broader, almost bimodal distribution, showing that there are frequency components from both the adjacent regions present in the middle mediating region, again similar to the case in the model system.

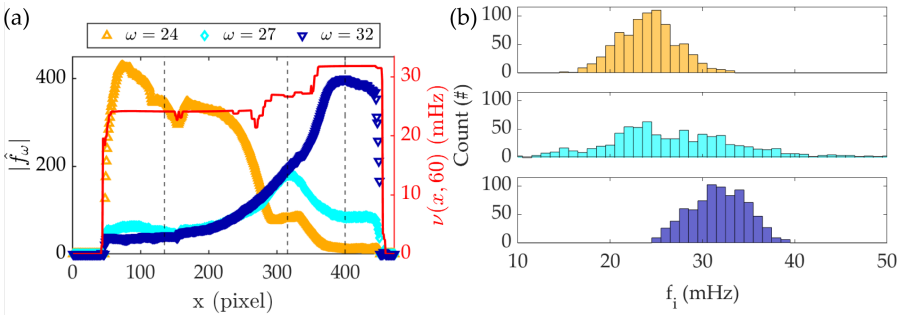

Figure 4.10: (a) Spatial profile of the absolute value of the Fourier transform of the ellipsometric intensity signal ξ for three different frequencies (see legend) together with the dominant frequency ν (red). Profile taken at $y = 60$, see dashed line in the ν plate in Fig. 4.4 (d). (b) Histogram of instant frequencies at three different points along the dashed lines in the ν plate in Fig. 4.4 (d): Yellow $x = 135$ pixel, cyan $x = 315$ pixel and blue $x = 400$ pixel.

However, in our case the dynamics of the mediating region appears phenomenologically rather coherent. On this basis, we would not classify our state as a typical chimera state, in contrast to the chimera states observed previously during silicon photo-electrodissolution [125, 130]. Since the main characteristics of our data is the coexistence of regions oscillating with different dominant frequencies, we classify the state as a multifrequency cluster.

Still, the relation between multifrequency clusters and chimera states as well as the classification of chimera states is a very intricate matter. This becomes clear when considering the relation of multifrequency clusters of different spatial extensions in continuous systems to weak chimera states in ensembles of four coupled discrete oscillators [7].

Loosely speaking, a chimera state in such a system is characterised by two oscillators being synchronised, with the frequency ν_1, while the other two oscillators possess frequencies which differ from each other as well as from ν_1 [7]. If, to a first approximation, we neglect the interfacial regions, a multifrequency cluster state with three different regions in a spatially extended system can likely be reduced to a low-dimensional system of three coupled oscillators where the coupling is weighted by the size of the domains. Thus, the dynamics of multifrequency clusters in systems with many degrees of freedom is in a sense equivalent to the one of a weak chimera state. If we now consider what happens if we do the reverse, i.e. extend the system size from a minimal weak chimera to a spatially extended system, it appears worthwhile to differentiate between chimera states, in which the number of incoherent oscillators scales with the system size and states in which it does not. Kemeth et al. have presented considerations along these lines and coined the first type of chimera state *extensive* which would suggest that the three frequency cluster state could be classified as an *intensive* chimera state [55]. In this respect, an important question to be investigated in the future is whether one can identify general dynamical properties that determine whether a weak chimera state behaves as an intensive or extensive chimera, in the sense defined here when successively increasing the number of oscillators.

Last, let us compare our findings to the multifrequency clusters in Ref. [15, 16]. The decisive element in their model equations is that the coupling is adaptive, i.e. the coupling function has its own temporal dynamics leading to different inter-coupling strengths between the clusters. In our case, the hole concentration n_h is the nonlinear coupling variable that also modifies the dynamics locally. From this point of view, it can be seen as establishing an adaptive coupling.

In Fig. 4.11 the frequencies of the multifrequency state from Fig. 4.4 (d) have again been indexed by their value and then the difference between the frequency at index i and index j is plotted for every 100th index. This again shows the plateaus of the frequencies, this time as squares with the value zero. It also gives an indication of how a possible self-organised coupling matrix resulting from the adaptive coupling could look with the intra and inter coupling strengths having different values, cf. Fig. 3. in Ref. [15]. Note that since we are looking at the difference in frequency here there is no information regarding the phase and hence we cannot, as Berner et al. differentiate between splay type and phase synchronised type clusters.

4.6 CONCLUSION

In conclusion, we have shown that the interaction of the global linear coupling in the form of an external resistor and the nonlocal coupling

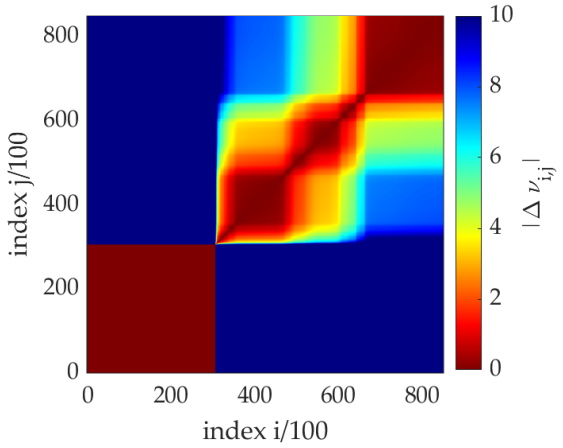

Figure 4.11: Absolute value of difference between dominant frequencies ν at every 100th index i and j of frequency data from Fig. 4.4 (d) sorted in ascending order. Note that the scale goes from 0-10 mHz and that the two blue regions at $i/100 > 300 \wedge j/100 < 300$ and $j/100 > 300 \wedge i/100 < 300$ respectively are not properly resolved, instead see Fig. 4.9 (d).

induced by the lateral movement of the holes results in an adaptive, nonlinear, nonlocal coupling. Our experimental observation of multifrequency clusters is not only an exceptional example where a self-organised adaptive coupling was observed in a nonliving system, but also reveals important open problems concerning the properties of multifrequency states in continuous systems, such as their relation to chimera states or requirements on the adaptive coupling for their existence.

5

BIRHYTHMICITY, INTRINSIC ENTRAINMENT, AND MINIMAL CHIMERAS

In the previous chapters we have discussed one type of oscillation and how it reacts on variations in the potential and illumination intensity. These oscillations, both with and without the external resistor (and the thereby introduced linear global coupling) have been classified as so-called Low Amplitude Oscillations (LAOs) [147]. The LAOs are typically found at high illumination (or in p-Si) with either a small or a very large external resistance [128, 147]. However, there is another type of oscillation. This other, so-called High Amplitude Oscillation (HAO) was first reported in Ref. [128] and is typically found either when the external resistance (linear global coupling) is moderate [128, 147] or the illumination is restricted in such a way that the current is limited (nonlinear global coupling) [125]. Although the electrochemical mechanism leading to either of these oscillations is not yet known, experiments suggested that they arise due to two different main feedback loops in the system [128]. This was also suggested by Tosolini et al. who reported the coexistence of chaotic attractors in the Si system and speculated that the bichaoticity is linked to an intrinsic bistability between two different types of oscillations—also referred to as birhythmicity—the interaction between the coexisting oscillators in phase space causing both of the limit cycles to become unstable and give rise to chaotic attractors [147]. In a birhythmic system, each of the two coexisting stable oscillatory states can have its own frequency and amplitude, and, in addition, might oscillate around different mean values [31]. Here, we will show explicitly that the electrodissolution of silicon does indeed exhibit the coexistence of two stable limit cycles albeit in a drastically different parameter range than the bichaotic one. As above, instead of using p-doped silicon as our Working Electrode (WE) as in Refs. [128, 147], we again use n-doped silicon. Recall that since at least the first oxidation requires a valence band hole, the electrooxidation of n-doped Si requires the illumination of the electrode with a wavelength that is larger than the band gap. The illumination intensity is thus an additional bifurcation parameter here that was not available in the bichaoticity study.

While dynamic phenomena connected to the coexistence between two stationary states, such as transitions between them or travelling

waves that might form in spatially extended systems, are well investigated [89], this is not the case for other types of bistability. Below, we demonstrate that the two directions of the transitions between the limit cycles can be of qualitatively different nature and that one oscillation might intrinsically be influenced by the other coexisting limit cycle, a phenomenon we refer to as intrinsic entrainment. Furthermore, we show that the coupling between two birhythmic systems oscillating on different limit cycles can be strongly asymmetric.

This chapter is structured as follows: in Sections 5.1-5.3 we first show the results obtained with one electrode, where birhythmicity is illustrated in phase space and physical space (5.2), and in the frequency domain (5.3). Then, coupling experiments with two electrodes are presented in Section 5.4. Implications of the experimental data concerning intrinsic and extrinsic coupling of the birhythmic system are discussed in Section 5.5.

The results in this chapter are part of Ref.[153] and are based in part on the work done by Juliane Wiehl during her Master's thesis [152]. Preliminary work was also done by Richard Hueck during his Master's thesis [49]. Both their theses were supervised as part of this thesis project.

5.1 BIRHYTHMICITY

In Fig. 5.1 exemplary time series of the current density j and the spatially averaged ellipsometric intensity signal $\langle\xi\rangle$ of the two oscillation types found during Si electrodissolution are depicted. The oscillations shown in Fig. 5.1 a)-b) are HAOs and the ones in Fig. 5.1 c)-d) are LAOs. The most striking differences between the two oscillation types are that the HAOs have a larger amplitude of the current density and a higher frequency than the LAOs. They also differ in their shapes; specifically the current of the HAOs is limited by the concentration of the available valence band holes during part of the oscillation. In Fig. 5.1 a) the current limit is indicated by a dotted line. We can tune this limit by changing the illumination intensity. Even though this means that the current amplitude of the HAO can be lower than the one of the LAO, we keep the naming convention introduced in the literature [128].

The two types of oscillations depicted in Fig. 5.1 were measured at identical parameter values, indicating that the system is birhythmic. Thus, which oscillation type is attained depends on the initial conditions. In order to establish HAOs we performed a voltage step from the open-circuit potential to a potential in the oscillatory region (6 V vs MSE for the measurements in Fig. 5.1) at high illumination intensity (> 2.5 mW/cm^2) and then reduced the illumination intensity to the desired intensity after the first two transient current oscillations. The LAOs were initialised by performing the same potential jump at the

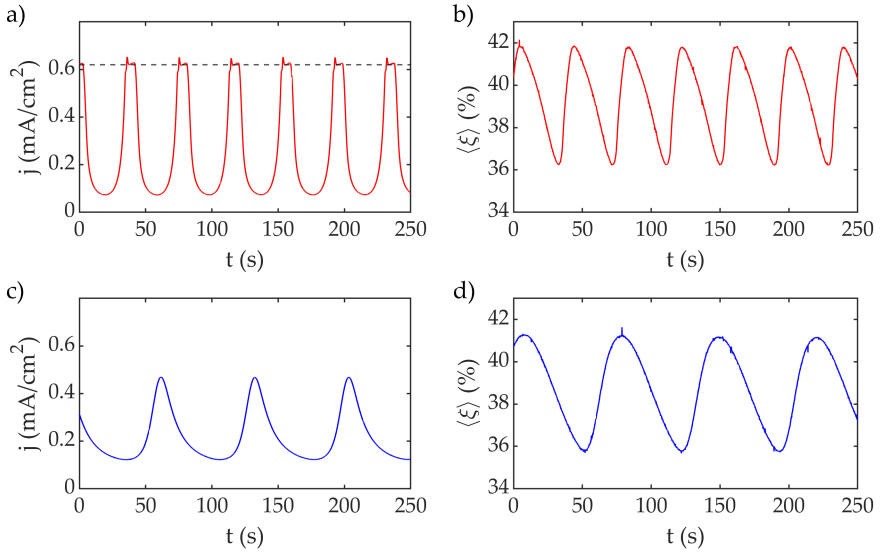

Figure 5.1: Exemplary time series of a High Amplitude Oscillation (HAO), red, and of a Low Amplitude Oscillation (LAO)), blue. a), c) current density j. b), d) spatially averaged ellipsometric intensity $\langle\xi\rangle$. Both oscillations were measured at $U = 6$ V vs MSE, $R_{\text{ext}}A$ =1kΩcm^2, A =15.72 mm^2, and $I_{\text{Ill}} = 1.31$ mW/cm^2.

same high initial illumination intensity as when initializing the HAOs. However, before lowering the illumination intensity to the desired value, we waited until any transients had decayed. Below we refer to these two protocols as the HAO- and the LAO-initialization protocols, respectively.

5.2 PARAMETER SPACE

In the following, we determine the illumination intensity interval in which the system exhibits birhythmicity at 6 V vs MSE. Therefore, we first initialised HAOs at a low illumination intensity of 0.68 mW/cm^2 and then increased the illumination intensity stepwise. At each step we waited until any transients had died out and then recorded the oscillation. In Fig. 5.2 a) representative HAOs at different illumination intensities are shown in the $j\langle\xi\rangle$-plane.

In these phase portraits the increase in the illumination-limited current plateau with increasing illumination density becomes obvious. When we increase the illumination intensity beyond the highest illumination intensity shown in Fig. 5.2 a) the system transitions to LAOs.

As we will detail below, the transition from HAOs to LAOs occurred through a nucleation and growth mechanism of the LAOs which entailed very long ($\geq$ 2 h), spatially inhomogeneous, transients. Therefore, we investigated the LAO branch by re-initializing LAOs according

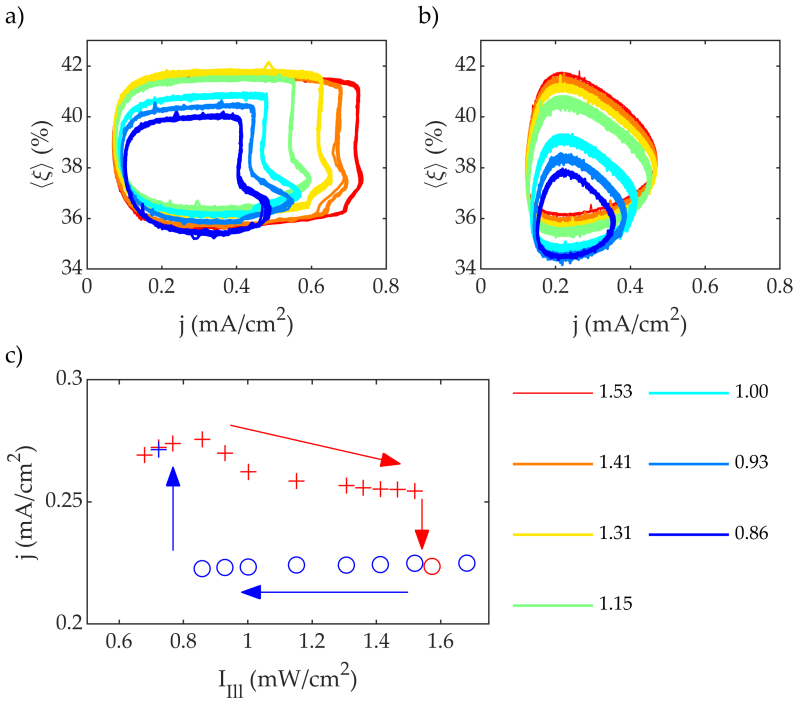

Figure 5.2: Birhythmic oscillations in the $j\langle\xi\rangle$-plane: a) HAOs and b) LAOs at different illumination intensities I_{Ill} (mW/cm^2) indicated by their respective colour (see legend in). Other parameter values: 6 V vs MSE and $R_{\mathrm{ext}}A = 1\mathrm{k}\Omega\mathrm{cm}^2$ with $A = 15.72$ mm^2 c) Average current density j_{av} of LAOs (○) and HAOs (+) vs illumination intensity I_{Ill} for the same parameters as used in (a) and (b). The measurements of (a) and (b) are included. The arrows indicate the order of measurement. Data from two separate measurement series: Red/blue symbols indicating that the series was initialised at low/high illumination intensities and that the illumination intensity was increased/decreased stepwise (see text).

to the LAO initialization protocol. In this way, we obtained spatially uniform oscillations before we lowered the illumination stepwise.

In Fig. 5.2 b) LAOs measured at the same parameters as the HAOs in Fig. 5.2 a) are depicted. The LAOs remain spatially homogeneous until the illumination is lowered down to 1 mW/cm^2. For lower illumination intensities patterns emerge leading to a lower amplitude of the spatially averaged signals, as shown in Fig. 5.2 b). The spatial symmetry breaking at low illumination intensity confirms our previous findings [107, 108]. Comparing the location of the coexisting HAOs and LAOs in the phase-space projections in Fig. 5.2 a)-b), it can be seen that they overlap at the corresponding illumination intensity. This strongly suggests that they live in an at least three dimensional phase-space.

The hysteretic behaviour is summarised in Fig. 5.2 c) where the average current densities of the oscillations are plotted versus the illumination intensity. Here, the measurement series shown in red was initialised using the HAO protocol and the measurement series shown

in blue was initialised using the LAO protocol, as described above. The HAO measurement series starts at low illumination intensities. If we follow it towards higher illumination intensities we see that the average current density decreases with increasing illumination before reaching a fixed value at approx. 0.26 mA/cm^2. The LAO measurement series starts at high illumination intensities. Following it, we see that the average current density does not change with decreasing illumination intensity until the system transitions from the LAO to the HAO at an illumination intensity of 0.72 mW/cm^2.

Next, we will have a closer look at the transient behaviour during the transition from HAOs to LAOs at high illumination intensities and the transition from LAOs to HAOs at low illumination intensities.

A 1D cut vs. time of the evolution of ξ and three 2D snapshots of the ellipsometric signal during the HAO→LAO transition are shown in Fig. 5.3 a) and b).

Here we can see that shortly after having increased the illumination intensity, a nucleus of the LAO appeared in the lower left part of the electrode at a point in time where the HAO current was limited, and thus very sensitive towards an increase in the hole concentration at the interface. This nucleus expands in space each time the HAO has again reached the current-limited phase. This indicates that the transition is triggered by diffusion of holes from the LAO region to the HAO region.

Thus, during the transition the LAO state expands in a step-like manner resulting in a striped pattern on the electrode surface (Fig. 5.3 b). The stepwise expansion can also be seen from the chequered pattern in the 1D-cut taken approximately along the direction of propagation of the LAO region. The arrangement of the squares of the chequerboard pattern reflects that the ratio of the frequencies of HAOs and LAOs is approximately 2:1.

In contrast to this stepwise transition, the transition from an LAO to a HAO at the low illumination border is abrupt and takes place on the entire electrode at the same time. In Fig. 5.3 c)-d) an example of such a transition is shown. Once the illumination has been reduced below a critical value, the electrode attains a HAO as soon as the current reaches the new maximal current level imposed by the reduced illumination.

If we expand our parameter space by also changing the applied voltage U, we obtain the 2D phase diagram shown in Fig. 5.4. Here, the HAOs are marked with crosses and the LAOs with circles. The red and blue areas indicate the regions where either HAOs or LAOs only were found, respectively, and the striped area marks the birhythmic region. Evidently, the birhythmic region extends over a large region in this parameter plane, demonstrating that birhythmicity is a robust feature of the system.

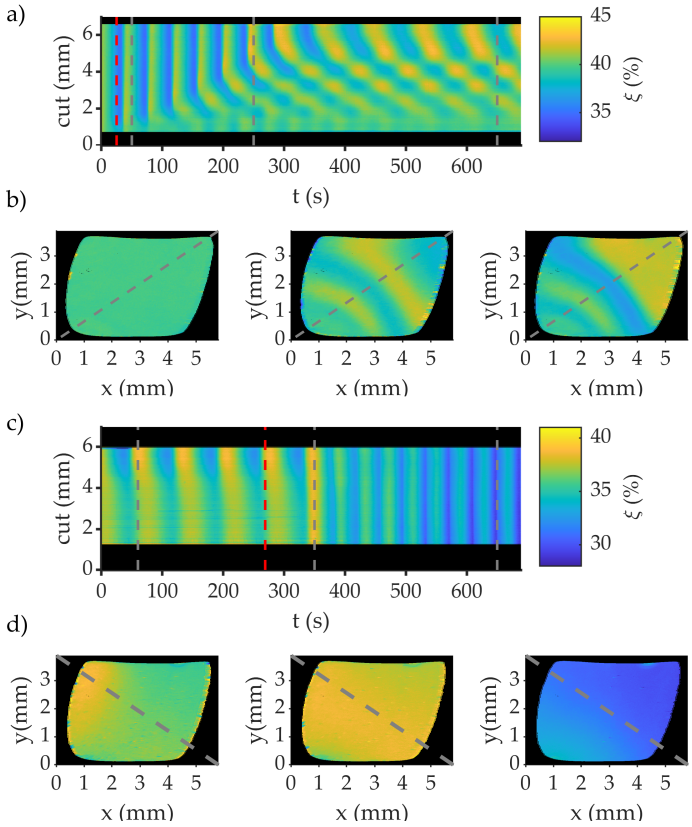

Figure 5.3: Examples of the spatio-temporal dynamics at the border of the birhythmic region when the system transitions to the other oscillatory state: a)-b) high illumination (transition from HAO to LAO) and c)-d) low illumination (transition from LAO to HAO) at the same parameters as in Fig. 5.2 c). The dashed red lines indicate the time when the illumination intensity was changed. a) and c): Temporal evolution of the ellipsometric intensity of a 1D cut indicated by the dashed line in the snapshots in b) and d) respectively. b) and d): Snapshots of the ellipsometric intensity taken at the times indicated by the dashed gray lines in a) and c) respectively. $R_{\text{ext}}A = 1\ \text{k}\Omega\text{cm}^2$ with $A = 15.72\ \text{mm}^2$.

5.3 FREQUENCY DOMAIN

For a further characterization of the birhythmicity, it is instructive to investigate how the frequencies of HAOs and LAOs change as a function of the parameter, and in particular how they behave at the transition points between the two oscillation forms. The easiest way to realise this is to use the applied voltage as our bifurcation parameter and perform a slow voltage scan while keeping the illumination intensity at a constant value. Therefore, we initialised the system at $I_{\text{Ill}} = 0.78\ \text{mW/cm}^2$ on either side of the birhythmic region and swept the voltage slowly until a transition was observed. Then the voltage sweep was reversed and the voltage was swept back to the initial value. We used a sweep rate of $\text{d}U/\text{d}t = 0.1\ \text{mV/s}$ which is slow on the time scale

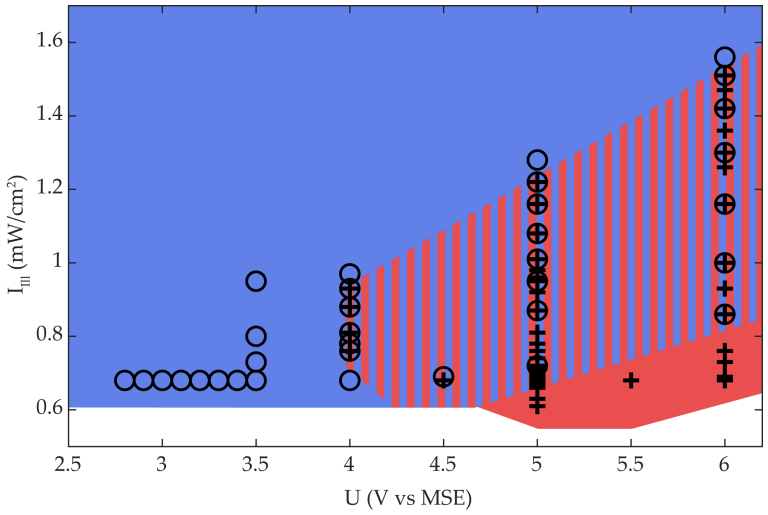

Figure 5.4: Birhythmic parameter region in the U-I_{Ill} parameter plane: HAOs (+) and LAOs (○). Approximate existence region of HAOs (red) and LAOs (blue). The striped region indicates the birhythimic region where both oscillation types are found. All measurements with $R_{ext}A = 1$ kΩcm^2.

of the oscillations. Hence, we consider the measured quasi-stationary states to be a good representation of the true state at the respective voltages.

In Fig. 5.5 the resulting spectrograms of the spatially averaged ellipsometric intensity signal of two such scans are shown.[1] Fig. 5.5 a) depicts an experiment that we initialised in an LAO at a low voltage, and b) one that we initialised in a HAO at high voltages. In each spectrogram the main frequency and the second frequency at each voltage are marked with a solid and a dashed line, respectively.

Again we can see that there is a hysteresis between the forwards and backwards scan, confirming once more that the system is birhythmic.

In the spectrogram in Fig. 5.5 a) we see that the main frequency of the initial LAO at 3.9 V vs MSE decreases before the system transitions to the faster oscillating HAO state at 5.8 V vs MSE. This transition from LAOs to HAOs occurs quasi-simultaneously on the entire electrode, just as in the case when we varied the illumination, cf. Fig. 5.3 c)-d). As the system undergoes the transition to a HAO, the main frequency abruptly jumps from 16 mHz to 26 mHz. This frequency of the HAO first stays approximately constant and then starts to increase at about 5 V vs MSE. The increase in frequency is accompanied by the emergence of a subharmonic mode.

We observe a similar behaviour when the system is initialised in a HAO state and the voltage is swept towards lower values (Fig. 5.5 b)). First, the frequency hardly changes with decreasing voltage until at

1 Note that the moving average is subtracted for each window. Frequency resolution 1 mHz, leakage 0.85, overlap 85 %.

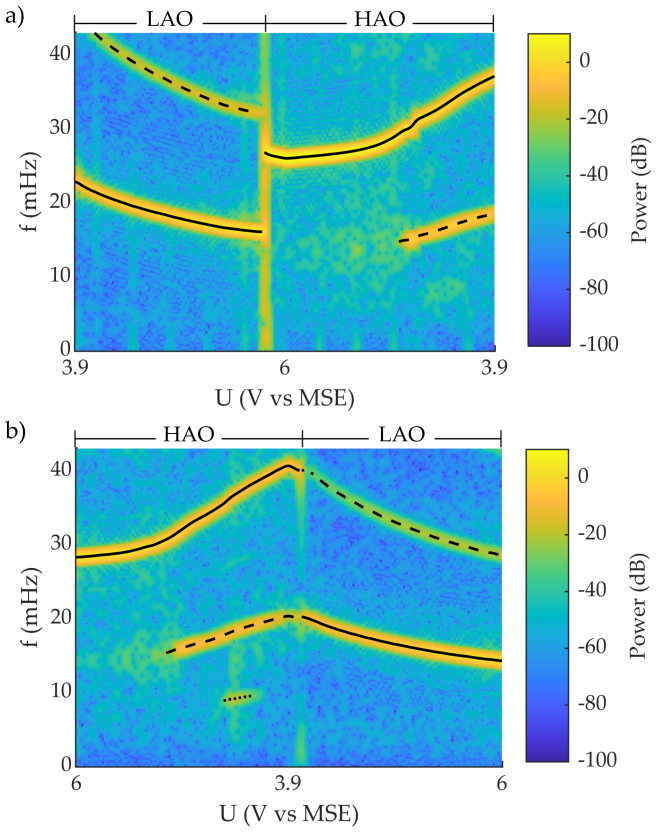

Figure 5.5: Spectrograms of the spatially averaged ellipsometric intensity signal $\langle \xi \rangle$ from quasi-stationary cyclic voltage scan (dU/dt =0.1 mV/s) at illumination intensity I_{Ill} =0.78 mW/cm^2. The solid line indicates the main frequency, the dashed line indicates the second frequency, and the dotted line indicates the third frequency. a) System initialised in an LAO state at 3.9 V vs MSE. b) System initialised in HAO state at 6 V vs MSE. Both measurements with $R_{\mathrm{ext}}A$ =1 kΩcm^2 and with A =17.51 mm^2 in a) and A =16.69 mm^2 in b).

about 5 V vs MSE where it starts to increase and a first subharmonic peak emerges. In a small voltage interval around 4.5 V vs MSE this first subharmonic peak is accompanied by a sub-subharmonic frequency.

The emergence of the subharmonic frequencies is accompanied by a spatial symmetry breaking. This is shown in Fig. 5.6 where a 1D cut vs. time of the evolution of ξ and three 2D snapshots of the ellipsometric intensity signal are shown. The 1D cut begins as the subharmonic frequency, just before the electrode starts to show pronounced antiphase clusters, at approx. 5 V and the snapshots are taken at the times indicated by the dashed lines in the cut.

We can see that the cut initially shows uniform oscillations before the electrode splits into two regions. That the two regions oscillate with a phase difference of approx. π can be seen clearly in the last two snapshots taken at two consecutive maxima of the spatially averaged

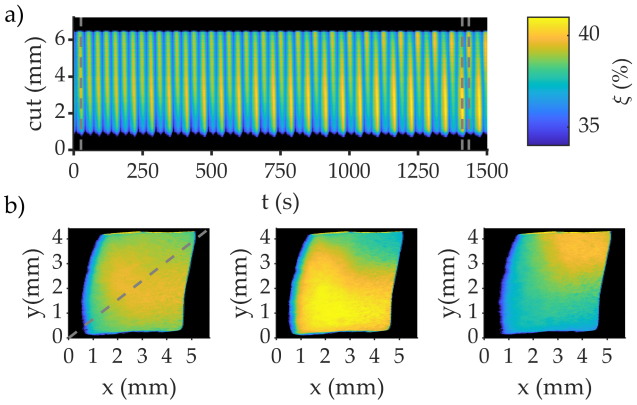

Figure 5.6: Spatio-temporal dynamics at approx. 5-4.85 V on the downwards scan shown in Fig. 5.5 b) where the first subharmonic peak has emerged. a) Temporal evolution of the ellipsometric intensity of a 1D cut indicated by the dashed line in the leftmost snapshots in b). b) Snapshots of the ellipsometric intensity taken at the times indicated by the dashed gray lines in a). $R_{\text{ext}}A = 1$ kΩcm^2 with $A = 16.69$ mm^2.

ellipsometric intensity signal $\langle\xi\rangle$. The different sizes of the two regions is reflected in the period 2 of $\langle\xi\rangle$ seen in Fig. 5.5 b).

Another way of visualizing the spatial symmetry breaking is by employing the Kuramoto order-parameter calculated from the phase dynamics of the electrode, see Eq. (4.3).[2] This gives us a clearer overview of how the spatial behaviour of the electrode changes as we scan the voltage. In Fig. 5.7 we plot the order parameter from the scan presented in Fig. 5.5 b) together with the main frequencies from the same scan.

Note that R oscillates, reflecting an oscillation between a narrower and a broader phase distribution. Here we see that at the beginning of the scan the oscillations in R are close to 1 indicating that the phase distribution is narrow and that the electrode is in a spatially uniform state. Once the subharmonic frequency emerges at around 5 V (leftmost dashed grey line) R starts to break down as the minimum value in each oscillation decreases. This happens due to the antiphase behaviour seen in Fig. 5.6. The non-zero minimum value of the oscillations in R is due to the difference in size of the two phase clusters. Going to lower voltages the minimum in the R-oscillations increases slightly, reflecting a more coherent phase dynamics on average, before it again decreases. This time the minimum in the R-oscillations decreases at the voltage where the sub-subharmonic frequency emerges. It is possible that this decrease is linked to a temporal period doubling but it reproduces a more complex spatial structure on the electrode. The

2 Note that the raw uncorrected video data was used to determine R. To determine the origin around which the phase winds a 200 s sliding mean was subtracted from each local time series. The time series were divided into multiple parts of 1500 s.

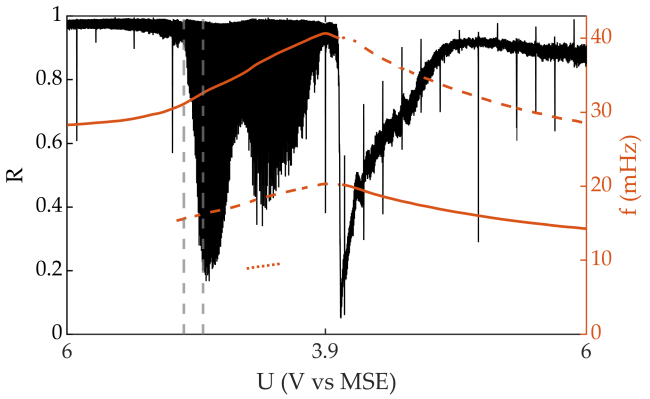

Figure 5.7: Order parameter R from the quasi-stationary scan presented in Fig. 5.5 b), together with the main frequencies from the scan. Dashed gray lines indicate the time window shown in Fig. 5.6. Spikes in R are numerical artefacts.

phase clusters seen at these higher potentials are less ordered and exhibit a more turbulent pattern.

These phase-cluster-type patterns disappear and the phase dynamics becomes more coherent at lower potentials, before the system transitions into the LAO state at 4 V vs MSE. At this transition the order parameter breaks down since the electrode undergoes the same type of transition as depicted in Fig. 5.3 a). Interestingly, at this transition the subharmonic frequency of the HAO matches the main frequency of the LAO and, accordingly, the main frequency of the HAO matches the first superharmonic frequency of the LAO. The appearance of the subharmonic frequency during the HAOs and the 1:2 frequency ratio of LAOs and HAOs at the HAO→LAO transition could be linked to a mutual influence of the two oscillations in phase space. We will come back to this point below.

5.4 TWO ELECTRODES

To better understand how HAOs and LAOs influence each other, we will now look at what happens when we physically split the WE into two smaller electrodes and couple the electrodes by short-circuiting them through a common external resistor. Due to this coupling, any change in current at one electrode causes the potential drops across both electrode/electrolyte interfaces $U_{\mathrm{el},1/2}$, to change according to:

$$U_{\mathrm{el},1} = U_{\mathrm{el},2} = U - R_{\mathrm{ext}} \left(j_1 A_1 + j_2 A_2 \right), \tag{5.1}$$

where U is the externally applied voltage, and $j_{1/2}$ and $A_{1/2}$ are the current densities and areas of the respective electrodes. Furthermore, the use of the SLM allows us to employ different initialization protocols to the two electrodes so that we can initialise each electrode in either a HAO or an LAO state independently.

In Fig. 5.8 the resulting time series of the spatially averaged ellipsometric intensity of the respective electrodes are shown for three different cases. All three cases were measured at the same parameters, they only differ in the initialization protocol. Note that both electrodes remain essentially spatially homogeneous, except of the LAO initialised electrode of case c) where minor spatial wave-like patterns emerged. Fig. 5.8 a) depicts time series of the two electrodes when they are both initialised with the HAO protocol. It can be seen that the oscillations on the two electrodes are slightly out of phase at $t = 0\,\mathrm{s}$, are in phase at $t = 185\,\mathrm{s}$, and have drifted to an antiphase configuration again at $t = 550\,\mathrm{s}$. Clearly, the slightly different parameters of the two electrodes (such as a minor difference in their electrode areas) lead to a small difference of their natural frequencies, and the coupling via the external resistor does not suffice to synchronise them.

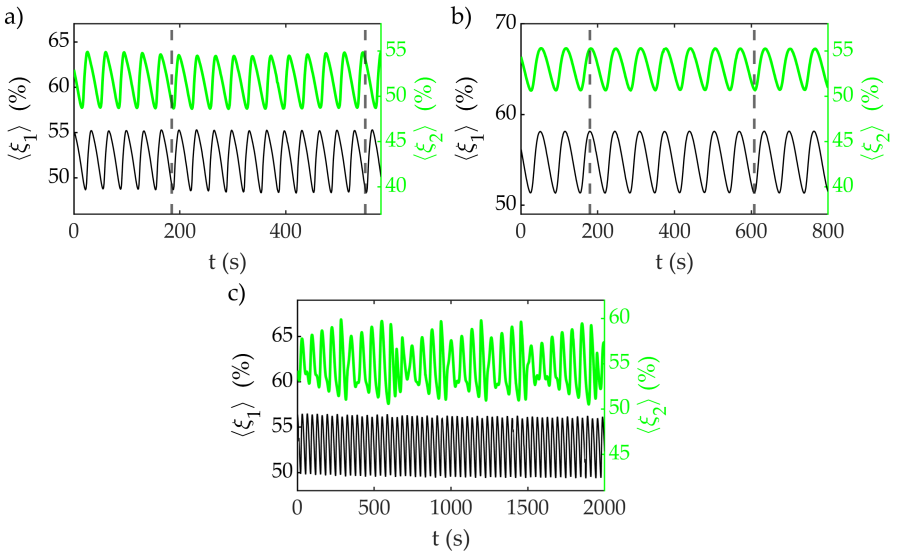

Figure 5.8: Exemplary time series of the spatially averaged ellipsometric intensity of two electrodes coupled electrically through an external resistor. a) Both electrode 1 $\langle\xi_1\rangle$ and electrode 2 $\langle\xi_2\rangle$ in a HAO state. b) Both electrodes in an LAO state. c) Electrode 1 in a HAO state and electrode 2 in a chaotic state. Here, electrode 2 was initialised using the LAO-initialization protocol. $A_1 = 11.43\ \mathrm{mm}^2$, $A_2 = 10.55\ \mathrm{mm}^2$. $R_{\mathrm{ext}}\,(A_1 + A_2) = 1\ \mathrm{k\Omega cm}^2$, $I_{\mathrm{Ill}} = 1.0\ \mathrm{mW/cm}^2$, $U = 5.75$ V vs MSE.

The picture is different in the case of the LAOs. When we initialise both electrodes using the LAO protocol, they typically exhibit phase synchronization, as can be seen in Fig. 5.8 b).

The behaviour is different again in Fig. 5.8 c) where we show an example where electrode 1 was initialised with the HAO protocol and electrode 2 with the LAO protocol. In this case, electrode 1 assumes a periodic HAO which is very close to the one of case a). In contrast, electrode 2 does not oscillate in a simple periodic LAO state. Instead it exhibits a more complex temporal behaviour. The frequency spectrum

of the time series (not shown) exhibits a strongly enhanced background distribution around the main oscillation frequency, suggesting that the dynamics is chaotic.

This counterintuitive coexistence of chaos and order is not only stable under these exact conditions but it persists for a wide range of potentials. When initializing the two electrodes in the same way as in Fig. 5.8 c) and then performing a quasi-static cyclic sweep of the applied potential we obtain the two spectrograms shown in Fig. 5.9.

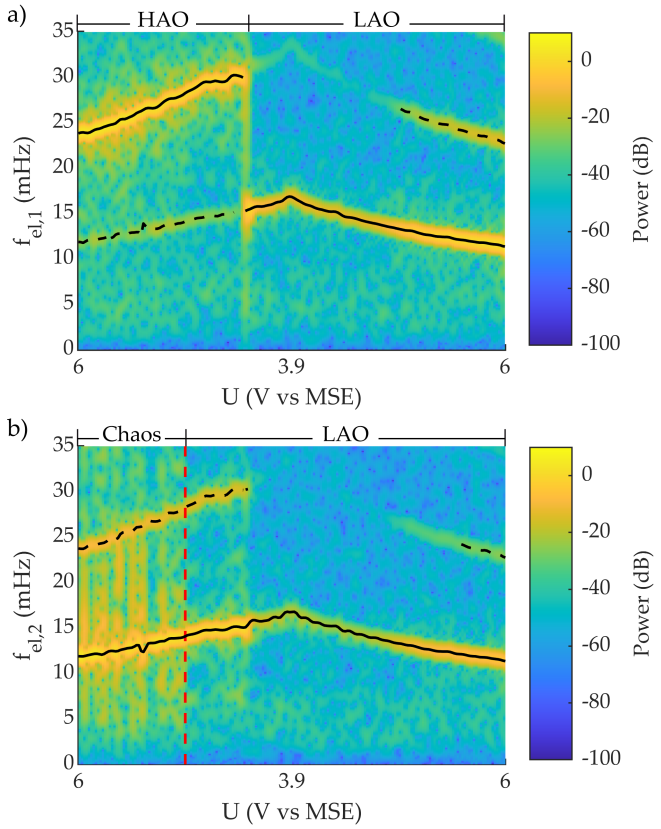

Figure 5.9: Spectrograms of two coupled electrodes, obtained from the spatially averaged ellipsometric intensity signal and a quasi-stationary cyclic voltage scan (dU/dt =0.1 mV/s) at illumination intensity I_{Ill} =0.94 mW/cm^2 and R_{ext} $(A_1 + A_2)$ =1 kΩcm^2. The solid line indicates the main frequency and the dashed line indicates the second frequency. a) Electrode 1, initialised with the HAO protocol, A_1 =5.53 mm^2. b) Electrode 2, initialised with the LAO protocol, A_2 =6.17 mm^2.

Again, the sweep rate was slow (dU/dt =0.1 mV/s) on the time scale of the oscillations and we assume that the measured states are in good agreement with the true state at the respective parameters. Fig. 5.9 a) shows the corresponding spectrogram of the electrode that was initialised with the HAO protocol. The electrode oscillates in a HAO state and behaves similarly to a single electrode under the same conditions; cf. Fig 5.5 b). The only difference is that the subharmonic

frequency is active in the entire existence region of the HAOs, not just from approximately 5 V vs MSE downwards. Fig. 5.9 b) shows the spectrogram of the electrode that was initialised according to the LAO protocol. This spectrogram differs significantly from the case with only one electrode; cf. LAO regions in Fig. 5.5. Here, we can see a broad potential region between 6 V vs MSE and approximately 4.9 V vs MSE, indicated by the dashed red line, where the power spectrum exhibits a strongly enhanced background and is smeared out around the main frequency and the first superharmonic frequency. This is a manifestation of the temporally complex behaviour. Hence, we have a large region in parameter space in which we find the coexistence of a periodic HAO on one electrode and complex, most likely chaotic oscillations on the other one. For potentials beyond the dashed red line the spectrogram of electrode 2 becomes narrower again before the superharmonic frequency disappears at the same voltage at which electrode 1 transitions from the HAO to the LAO. In this intermediate region the HAOs and LAOs on the two electrodes exhibit a 2:1 locking. After the transition of electrode 1 to the LAO state both electrodes exhibit phase-synchronised LAOs. The reason for the slightly lower power after the transition is that patterns form on both electrodes, suppressing the amplitude of the spatially averaged signal. Once the electrodes become spatially more uniform again, the superharmonic peak in the spectrum becomes visible again, too.

5.5 DISCUSSION

We have here presented clear-cut experimental evidence that the Si-system exhibits birhythmicity. Besides this observation, our experiments elucidated unusual, though general ways, in which coexisting limit cycles can interact with each other. In the following we take a closer look at these interactions. We discriminate here between an *extrinsic* interaction of (nearly) identical birhythmic systems, and an *intrinsic* interaction of the two limit cycles in phase space.

The extrinsic coupling mechanism is the one easier to rationalise. We will therefore discuss it first. Consider again the results depicted in Fig. 5.8. Here, we coupled two nearly identical Si electrodes through an external resistor. Hence, the coupling acts, as given by Eq. (5.1), on the potential drops across the interface of the electrodes. The fact that the oscillations of the two electrodes phase-synchronise when they are both initialised with the LAO protocol but that the phases of the oscillations remain drifting when the electrodes are initialised with the HAO protocol reveal that the sensitivity of HAOs and LAOs towards perturbations in the potential is vastly different. The experiment, where the two electrodes were initialised in different states, shows that the impact of the electrode initialised in an LAO on the one initialised in a HAO is negligible, while the other way round the electrode initialised

in an LAO is strongly forced by the electrode initialised in the HAO state. Thus, the mutual interactions of the two types of oscillations is unidirectional.

The phase-space portraits depicted in Fig. 5.2 shed light on this unidirectional coupling. The phase portraits of the two limit cycles intersect in the $j\langle\xi\rangle$-phase-space plane suggesting that the oscillations live in a phase space spanned by at least three essential variables. The sensitivity of the LAO with respect to changes in the electrode potential indicates that the electrode potential is an essential variable for the LAOs. Contrary, from the insensitivity of the HAOs upon variations of the electrode potential we can conjecture that the HAO limit cycle occupies a subspace of phase space that is orthogonal to the electrode potential axis. Yet, since during HAOs the current oscillates, the coupling through the resistor changes the electrode potential of both electrodes. The oscillating electrode potential acts like a periodic forcing on the LAO, while it is like an 'invariant' parameter for the HAO. That the HAOs are insensitive towards variations in the electrode potential is in line with previous findings where the method of control was changed from potentiostatic control, via an external current limiting circuit, all the way to galvanostatic control without changing the qualitative behaviour of the HAO [127].

The coupling experiments presented in Fig. 5.8 c) were carried out at 5.75 V vs MSE. The spectrograms in Fig. 5.5 confirm, that between approx. 6 and 5 V vs MSE the HAO frequency is essentially independent of the applied voltage.

This changes at lower voltages, where we will argue that an intrinsic coupling comes into play. Here, the HAO frequency increases considerably, and, more strikingly, a subharmonic frequency emerges. In Fig. 5.10 we take a closer look at what happens to the signals during the scan as this frequency emerges. To do this we construct an orbit diagram by taking all maxima of relative importance of the signals and plot them vs. the applied voltage.[3] Here the orbit diagrams of the total current density and the average ellipsometric signal around 5 V vs MSE are plotted.

These exhibit the typical signature of a period doubling bifurcation with decreasing voltage, i.e. increasing differences in the maxima of successive oscillations. This corroborates that the system lives in an at least 3-dimensional phase space.

More importantly, the subharmonic frequency coincides almost perfectly with the frequency of the LAO, at least at the HAO→LAO transition (see Fig. 5.5 b)). It appears likely that this is not a coincidence but rather that the existence of the LAO in phase space triggers the period doubling bifurcation. In other words, the HAO is intrinsically

3 We choose a minimum peak prominence of 0.1 for the current density and 0.5 for the ellipsometric signal, required a minimal distance between the peaks of 1 mV and confirmed the detection of the peaks by ocular inspection.

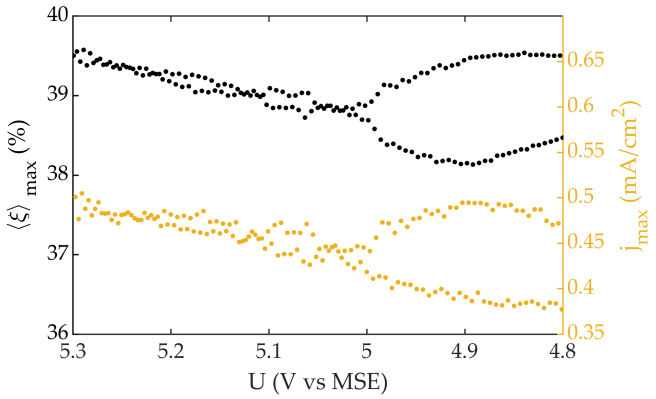

Figure 5.10: Orbit diagram of the current density j and the average ellipsometric signal $\langle\xi\rangle$ during the downwards scan presented in Fig. 5.5 b). Here the maximal values of the oscillations are plotted vs the applied voltage.

entrained to the LAOs in a 2:1 resonance. The emergence of patterns at the period doubling (cf. Figs. 5.6 and 5.7) could also be interpreted as an indication that the LAOs influences the HAOs. It has been shown that when an oscillatory medium is exposed to a time-periodic perturbation it can show 2:1 subharmonic resonant patterns [73, 74] possibly explaining why the period doubling is accompanied by phase clusters.

A possible scenario for this intrinsic entrainment would be as follows: recall that also here the WE is connected to the potentiostat via an external resistor. Thus, the oscillating current during HAOs causes an oscillating electrode potential. Above we have discussed that these changes in the electrode potential affect the LAOs in a second electrode. For an individual electrode, the LAOs exist somewhere else in phase space. Yet, the phase space structure can be such that the oscillatory motion of the LAO is felt also on the other side of the separatrix where initial conditions relax to the HAO. Hence, the oscillatory potential will induce an oscillatory motion in the plane spanned by the essential variables of the LAOs. We have argued above that one of these variables is the electrode potential upon which the HAOs are insensitive. HAOs could, however, be sensitive, on changes in the second essential LAO variable. Then, we can interpret the period doubling of the HAO as being caused by an intrinsic entrainment originating from the coexisting LAOs.

Note that in addition, at voltages lower than approx. 4 V vs MSE the HAOs might become more sensitive against perturbations in the electrode potential than they are at higher potentials. We have seen that the LAOs are sensitive towards the concentration of holes at the Si/SiO_2 interface. At high voltages, the potential drop across the space charge layer is large, and with the space charge layer being compact nearly all holes that are generated by the illumination in the bulk of the Si are quickly drawn to the Si/SiO_2 interface. Their concentration

thus remains unaffected by the externally applied voltage. At lower voltages, however, some of the holes will recombine with electrons before reaching the surface. The fraction of holes which is lost due to recombination is larger the lower the voltage is. At present, we do not know whether the mechanism leads to an appreciable change in hole concentration at the interface. If it does, it would lead to a sensitivity change of the HAOs towards changes in the potential. However, independently of the sensitivity of the HAOs towards perturbations in the electrode potential, the occurrence of a 2:1 resonance still seems to require that the HAOs couple to the motion of the LAOs - most likely involving a second variable.

The different sensitivity of HAOs and LAOs on perturbations in different variables also explains the different nature of the transitions HAO→LAO and LAO→HAO (cf. Fig. 5.3).

Let us first look at the HAO→LAO transition, which occurs through a nucleation and growth mechanism. We can assume that the growth of the LAO domain is mediated via diffusion of valence band holes. Every time the HAO is on the current limited plateau, diffusion of holes from the LAO covered region to the HAO region triggers a transition from the HAO to the LAO close to the boundary between the two oscillations. Thus, the propagation velocity of the LAO region is determined by a combination of the limited (nonlocal, see Refs. [107, 108]) diffusion length of the holes and the oscillation frequency of the HAOs.

In contrast, the LAO→HAO transition takes place on the entire electrode at almost exactly the same time. This fast transition indicates that the coupling has a nearly global range. Considering that the external resistor introduces a global coupling on the potential and the fact that the LAOs are very sensitive to changes in the potential, it is most likely that this spatially uniform transition is triggered through a perturbation in the potential that lifts the LAO on the entire electrode across the separatrix.

Finally, let us turn again to the two coupled electrodes, where one electrode was initiated in the HAO state and the other in the LAO state (Fig. 5.8 c). These dynamics are very similar to the smallest chimera state as found as solutions in a chemical model of two coupled identical unimodal oscillators [9, 10]. Similar to our results, the simulation shows one oscillator exhibiting regular oscillations while the other one exhibited chaotic oscillations. To the best of our knowledge, we present here the first experimental realization of a smallest chimera state consisting of only two coupled oscillators. Furthermore, the authors of Refs. [9, 10] attributed this particular type of chimera state to a "'master-slave' interaction". The authors argue that in their case this coupling was generated by a canard explosion. We present evidence that in our case the effective unidirectional coupling comes about by the widely different sensitivities of the two birhythmic limit cycles with respect to the coupling variables.

Yet, we note that at this stage it is unclear whether the chaotic behaviour of the LAO initialised electrode can be fully explained by the unidirectional coupling. The dynamics is further complicated by the fact that the forcing of the LAO by the HAO increases the maximal current density of the LAO such that it reaches the illumination-limited current level. We saw in Chapters 3 and 4 that when an LAO comes close to the illumination-limited current level, the electrode tends to form spatial structures. Here, too, the electrode does not remain completely uniform but tends to form fast spreading waves. This is typical for the current limiting phase. In Fig. 5.11 the order parameter R, see Eq. (4.3), during a HAO is plotted together with the total current density.[4]

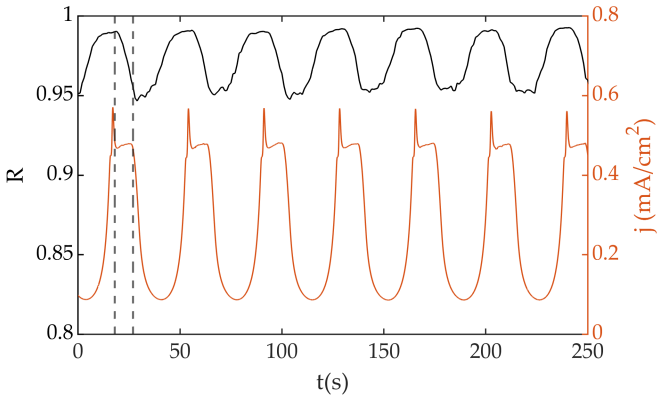

Figure 5.11: Order parameter R and total current density j of the HAO shown in Fig. 5.2 a) in turquoise.

We see that the order parameter oscillates with the same frequency as the current, reaching minima at around 0.95 as the current density leaves the current limited region and then increasing up to almost 1. Once the current density reaches its limit again R decreases sharply. A decrease in R means that the phase distribution on the electrode becomes broader. Since the order parameter decreases upon the oscillation reaching the current limit this indicates that we have a nonlinear desynchronising coupling that is activated once the amount of available holes at the interface is no longer abundant.

A connection between birhythmic systems and chimera states has also been discussed in the context of ensembles of coupled oscillators [114, 157]. In Ref. [114] a model of nonlocally coupled birhythmic oscillators was considered and the authors found that the oscillators could organise themselves in synchronised domains separated by asynchronous domains. Also in ensembles of birhythmic Stuart-Landau-type as well as birhythmic phase oscillators chimera states were reported to exist [157].

4 Note that here the corrected video data (cf. Eq. (2.6)) was used.

With the present system, it might be possible to experimentally validate some of the predictions of the theoretical studies. Furthermore, when changing the perspective and viewing the system of two coupled electrodes not as a system consisting of two individual units but instead regarding each subsystem as an oscillatory medium with many coupled degrees of freedom, then a large variety of possibilities opens up to investigate pattern formation in coupled networks experimentally.

5.6 CONCLUSION

In this chapter, we confirmed that there are two different types of current oscillations during silicon electrodissolution. We explicitly showed that, for a broad range of parameters, these oscillation types are bistable; i.e. the system exhibits birhythmicity. Furthermore, we were able to identify three dynamical properties that are closely related to the birhythmic nature of the system:

(1) An *intrinsic* entrainment of the motion of one oscillator to the motion of the other one, mediated by the vector field in phase space.

(2) A unidirectional type coupling of two identical oscillatory systems. This behaviour is linked to the possibility that the two limit cycles exhibit pronouncedly different sensitivities towards the perturbation in a variable.

(3) The existence of a stable state of two coupled, identical electrodes where one electrode oscillated chaotically and the other one periodically, illustrating a route to a two oscillator minimal chimera state.

Currently, we are only in the beginning of understanding coupled birhythmic systems. The present system promises to become a prototypical experimental model system for studies of birhythmic dynamics. The very property that distinguishes the present system from other ones is that the initial conditions can be easily controlled both in time and space, allowing to set each location - or coupled electrode - in the chosen oscillation type.

6

SUMMARY AND OUTLOOK

We have investigated a robust experimental model system: the electrodissolution of silicon in a fluoride containing electrolyte under anodic potential. This investigation can be split into two main parts: the physicochemical studies and the studies of emergent patterns. In this way we have furthered not only the understanding of dynamical phenomena but also progressed our knowledge of the experimental system itself.

We started by looking closer at the physicochemical properties and focused on elucidating the most fundamental behaviour of the system.

The first property we investigated was the NDR-branch of the CV. We were able to confirm that NDR-branch is stable and also showed that the dissolution valency increases with increasing voltage on this branch. This work was done in parallel to the development of the model presented in Ref. [120] which aims to explain, among other things, the origin of the NDR. The model assumes that the etch rate depends on the degree of Si-oxidation in the silicon/silicon-oxide/electrolyte interface and predicts that the interfacial valency in the oxide layer increases with increasing applied voltage in the NDR region. Our experimental validation of the increase of the valency leads us to conclude that the model is plausible and that the NDR behaviour is linked to a change in oxide quality.

Furthermore, we found that the system can oscillate even without an external resistor or an illumination-induced cut-off of the current. This unexpected finding opened up the option to investigate the impact of the hole dynamics on pattern formation without an additional coupling of different positions on the electrode by a global coupling, brought about by an external resistance. Here we found that when there is a scarcity of electron holes, i.e. when the internal quantum efficiency is larger than 1, spatiotemporal patterns are observed. This implies that the hole dynamics is decisive for the formation of the observed spatiotemporal patterns.

Both the findings regarding the NDR and the ones regarding the hole dynamics are also of interest when considering the dynamics of the system.

Let us here first discuss the NDR behaviour, which is typically associated with the emergence of oscillations [60]. However, in the case

of the Si-system, possible links between the NDR and the oscillations are not clear and we cannot yet say that the NDR is necessary for, or that it can explain these oscillations. Still, we cannot exclude it as an important factor either, especially for the HAO. For the oscillations to be linked to the NDR it is decisive that electrode potential enters the region where the NDR is found. The oscillations are typically observed at applied potentials that are higher than the potentials where the NDR is found and hence an additional significant potential drop is needed, e.g. an IR-drop across an external resistor. The combination of the relative large current amplitude and an external resistance that is typically associated with the HAOs [128, 147] could lead to a potential drop across the electrode that is comparable to the potential where the NDR is typically measured. The exact potential distribution in the case of the HAOs with a current cut-off that we presented in Chapter 5 is not yet known but the potential drop across the space charge layer can be assumed to be large during the part of the oscillations where the current is limited.

Why the current amplitude of the HAOs is large compared to the one of the LAOs is not known. It is possible that the larger current amplitude is linked to micropores in the silicon oxide which could lead to the electrolyte coming in direct contact with the silicon [42, 71], or to an increased roughness [95]. It should, however, be noted that it is not clear what type of oscillations were measured in the above mentioned references. Another possible reason for the larger current amplitude could be that the pH could be different close to the electrode compared to the electrolyte bulk. This can happen due to the fact that the electrochemical oxidation emits protons, cf. Eq. (2.1)-(2.2). This would lead to a different distribution of the fluoride species and in turn to a different etch rate, possibly resulting in a higher current. One way of measuring the local change in the pH would be to use so-called scanning ion conductance microscopy [93].

In the case of the LAOs a connection between the NDR and the oscillations is less likely. The LAOs are found at potentials that are higher than the NDR-region and any IR-drop is small, either due to a small current amplitude or a small external resistance. In the extreme case shown in Chapter 3, the LAOs do not even require an external resistor.

However, the interplay between the NDR and the LAOs is interesting from another point of view. We showed in Chapter 3.2 that at the low-current end of the NDR-branch the transients become oscillatory, indicating that the system is close to a Hopf bifurcation. This is corroborated by the fact that we found stable oscillations at slightly higher voltages. This is also in line with our findings reported in Ref. [147]. Therein, we also showed that the NDR-branch becomes unstable through a saddle-node bifurcation when a sufficiently large external resistor is added. It seems plausible that the two bifurcations

could meet in a local codimension-2 bifurcation [119], a so-called Fold-Hopf bifurcation [43]. This would require an at least 3-dimensional phase space where the oscillations that emerge from the Hopf bifurcation would live on a 2-dimensional manifold and the third direction would undergo the saddle-node bifurcation. Initial experiments from our group have even shown that there is a seemingly slow variable component of the ellipsometric intensity signal that could correspond to the saddle-node direction, see [106, 147]. It could be helpful to decompose the ellipsometric signal into its oscillatory components and a slowly varying component. One candidate for such a slowly changing variable is the oxide layer thickness and it would thus be of interest to measure how it changes directly. This would require a different measurement technique than our implementation of the ellipsometric imaging set-up since our signal is a measurement of the relative change of the optical path-length through the oxide and not the oxide thickness directly. There is even data that strongly suggest that the oxide thickness is not one of the oscillating variables for what we interpret to be LAOs [139]. One way of measuring the thickness directly could, for example, be to combine so-called etch-back experiments [128] with scanning electrochemical microscopy-atomic force microscopy (SECM-AFM) [53]. SECM-AFM could also be used to determine the etch rate of the oxide locally as well as to measure the local current. A big challenge with these type of measurements is that the instruments have to be stable in our fluoride containing electrolyte.

Having discussed the NDR-branch let us now look at the hole dynamics and the role that they play in the formation of the spatiotemporal patterns. We here presented the first experimental observation of self-organised multifrequency clusters, the coexistence of multiple regions with different frequencies. These were found to emerge from uniform initial conditions without any externally controlled feedback. We attribute this to the coupling being adaptive in the sense that the hole concentration acts as our coupling variable and that it influences the local dynamics which, in turn, determines the coupling strength. By looking at the gradient of the electrochemical potential we could show that the hole-induced coupling is both nonlinear and nonlocal.

The fact that this is an example of a self-organised adaptive coupling in an easily controllable inanimate system again corroborates that the Si-system is an extraordinary model system. Not only is it of interest to investigate how the resulting multifrequency cluster relates to the previously reported chimera states [124, 125, 130], the system can also, for example, be used as a model system for better understanding nonlinear adaptive coupling. One way of investigating the coupling further would be to couple several, spatially separated active parts of the electrode and thus to build up networks of adaptively coupled oscillators. The SLM could then be used to selectively illuminate the

active electrode areas. The coupling type is of interest in its own right but it is also of interest, for example, in a biological context [41].

The other main dynamical feature that we found in the Si-system is birhythmicity. We demonstrated that the two previously reported different oscillation types [128, 147] do in fact coexist in phase space and, hence, that the system exhibits birhythmicity. Not only do the two oscillation types coexist but they also interact in phase space, causing an intrinsic entrainment whereby the motion of one oscillation type is influenced by the other via the vector field in phase space. In addition, the two oscillation types exhibit pronouncedly different sensitivities towards perturbations in the electrode potential. This difference in sensitivity explains the difference in the transients from one oscillation type to the other. Together with the fact that the initial conditions can be easily controlled, the difference in sensitivity also allowed us to investigate a unidirectional coupling of two identical oscillatory systems.

One of the results of this unidirectional coupling in the case of two coupled electrodes was that one electrode exhibited periodic oscillations and the other one exhibited chaotic oscillations, yielding what we interpret as a two oscillator minimal chimera state.

Due to this interesting interaction and the fact that the initial conditions can be easily set, the Si-system promises to become a prototypical experimental model system for studying birhythmic systems. The understanding of birhythmic systems and how they interact is still in its infancy and it would, for example, be interesting to investigate what happens for a large number of coupled birhythmic oscillators.

We have here presented some of the aspects of the multifaceted, robust, and complex behaviour of silicon electrodissolution as well as some of the different coupling modes and oscillatory behaviours found therein. In conclusion, our explorative study has shed new light not only on the system itself but also on more general questions within the field of nonlinear dynamics. Specifically, we have extended the plethora of dynamic phenomena found in the system by experimental examples of both adaptively coupled oscillators and birhythmicity. Both these findings open up two directions that can be explored further.

APPENDIX

A

PREPARING SAMPLES WITH PHOTOLITHOGRAPHY

Below are step-by-step instructions for how to prepare p-silicon samples for the valency measurements using Si_3N_4 covered silicon wafers. Here we used wafers with a Si_3N_4 thickness of 300 ± 10 nm.

The complex refractive index used to determine the Si_3N_4 thickness was: $n = 1.99369$, $k = 0.00507$.

A.1 CUTTING WAFER

ATTENTION! Always cover the wafer with photoresist before cutting/scratching it or doing anything that could result in dust getting in contact with the sample!

1. Clean the wafer successively in acetone and isopropanol in an ultrasonic bath for approx. 10 min each at 45°C. Blow dry.
2. Spin coat the smooth surfaced side with photoresist AZ 5214 E (Merck).
3. Soft-bake for 120 s at 100°C.
4. Scratch the photoresist-covered side using a diamond cutter. Ensure that the scratch is deep enough for easy cutting.
5. Cut wafers into 11x11 mm samples. Do this away from the workstation to avoid contaminating it.
6. Remove the photoresist by cleaning the wafer successively in acetone and isopropanol in an ultrasonic bath for approx. 10 min each at 45°C. Blow dry.

A.2 PHOTOLITHOGRAPHY

1. Spin coat the smooth-surfaced side with photoresist. Take care so that the photoresist forms a homogeneous layer (approx 1-2 µm). Program the spin coater to do 3000 RPM for 30 s.
2. Soft-bake for 120 s at 100°C.
3. Illuminate with a mask aligner with 350 W for 12 s.
4. Develop for approximately 45-60 s in a 1:4 developer:water solution, use non-metallic tweezers. Developer: AZ 400 K (Merk)

5. Ensure that there is no photoresist residue by using a microscope. If there are visible larger residue, develop for longer.
6. Etch the samples in a Reactive Ion Etching (RIE) system. Assume an approximate etch rate of the Si_3N_4 of approx. 1 nm/s.
7. Remove the photoresist by cleaning the wafer in acetone and rinse using isopropanol. Blow dry.

ATTENTION! Do not put the samples in a plasma asher as this can result in structures on the samples caused by oxidising possible metal residue!

A.3 BACK CONTACT

1. Etch the rough side of the samples in the RIE system.
2. Put on new photoresist on the front side to protect it.
3. Clean the back side of the samples with acetone and isopropanol with the help of a cotton swabs.
4. Put the samples in water to ensure that any isopropanol residue is dissolved.
5. Optional step: etch the rough side with buffered 1:6 HF:NH_4F. This can be omitted if step 4 is done directly after, or on the same day as step 1.
6. Evaporate Al onto newly etched side of the wafer (4 slugs, approx. 200 nm).
7. Clean the samples in acetone, isopropanol, and water to get rid of the photoresist.
8. Anneal the samples at 400°C for 30 min.

ATTENTION! Always remove any photoresist before heating the samples or storing them for a longer period of time!

B

LIST OF PUBLICATIONS

- K. Schönleber, M. Patzauer and K. Krischer. 'A comparison of modeling frameworks for the oscillatory silicon electrodissolution'. In: *Electrochimica Acta* 210 (Aug. 2016), pp. 346–351. ISSN: 00134686. DOI: 10.1016/j.electacta.2016.05.144.
- M. Patzauer, R. Hueck, A. Tosolini, K. Schönleber and K. Krischer. 'Autonomous Oscillations and Pattern Formation with Zero External Resistance during Silicon Electrodissolution'. In: *Electrochimica Acta* 246 (Aug. 2017), pp. 315–321. ISSN: 00134686. DOI: 10.1016/j.electacta.2017.06.005.
- D. Koster, M. Patzauer, M. M. Salman, A. Battistel, K. Krischer and F. La Mantia. 'Measurement and Analysis of Dynamic Impedance Spectra Acquired During the Oscillatory Electrodissolution of p-Type Silicon in Fluoride-Containing Electrolytes'. In: *ChemElectroChem* 5.12 (June 2018), pp. 1548–1551. ISSN: 2196-0216. DOI: 10.1002/celc.201800252.
- M. M. Salman, M. Patzauer, D. Koster, F. La Mantia and K. Krischer. 'Electro-oxidation of p-silicon in fluoride-containing electrolyte: a physical model for the regime of negative differential resistance'. In: *The European Physical Journal Special Topics* 227.18 (Apr. 2019), pp. 2641–2658. ISSN: 1951-6355. DOI: 10.1140/epjst/e2019-800118-x.
- A. Tosolini, M. Patzauer and K. Krischer. 'Bichaoticity induced by inherent birhythmicity during the oscillatory electrodissolution of silicon'. In: *Chaos* 29.4 (Apr. 2019), p. 043127. ISSN: 1054-1500. DOI: 10.1063/1.5090118.
- M. Patzauer and K. Krischer. 'Self-Organized Multifrequency Clusters in an Oscillating Electrochemical System with Strong Nonlinear Coupling'. In: *Physical Review Letters* 126.19 (May 2021), p. 194101. ISSN: 0031-9007. DOI: 10.1103/PhysRevLett.126.194101.
- J. C. Wiehl, M. Patzauer and K. Krischer. 'Birhythmicity, intrinsic entrainment, and minimal chimeras in an electrochemical experiment'. In: *Chaos* 31.9 (Sept. 2021), p. 091102. ISSN: 1054-1500. DOI: 10.1063/5.0064266.

BIBLIOGRAPHY

[1] D. M. Abrams and S. H. Strogatz. 'Chimera States for Coupled Oscillators'. In: *Physical Review Letters* 93.17 (Oct. 2004), p. 174102. ISSN: 0031-9007. DOI: 10.1103/PhysRevLett.93.174102.

[2] M. Alamgir and I. R. Epstein. 'Birhythmicity and Compound Oscillation in Coupled Chemical Oscillators: Chlorite-Bromate-Iodide System'. In: *Journal of the American Chemical Society* 105.8 (Apr. 1983), pp. 2500–2502. ISSN: 15205126. DOI: 10.1021/ja00346a080.

[3] M. Alamgir and I. R. Epstein. 'Systematic design of chemical oscillators. Part 19. Experimental study of complex dynamical behavior in coupled chemical oscillators'. In: *The Journal of Physical Chemistry* 88.13 (June 1984), pp. 2848–2851. ISSN: 0022-3654. DOI: 10.1021/j150657a036.

[4] P. W. Anderson. 'Spin Glass I: A Scaling Law Rescued'. In: *Physics Today* 41.1 (Jan. 1988), pp. 9–11. ISSN: 0031-9228. DOI: 10.1063/1.2811268.

[5] M. Anvari, F. Hellmann and X. Zhang. 'Introduction to Focus Issue: Dynamics of modern power grids'. In: *Chaos* 30.6 (June 2020), p. 063140. ISSN: 10897682. DOI: 10.1063/5.0016372.

[6] F. T. Arecchi, R. Meucci, G. Puccioni and J. Tredicce. 'Experimental Evidence of Subharmonic Bifurcations, Multistability, and Turbulence in a Q-Switched Gas Laser'. In: *Physical Review Letters* 49.17 (Oct. 1982), pp. 1217–1220. ISSN: 0031-9007. DOI: 10.1103/PhysRevLett.49.1217.

[7] P. Ashwin and O. Burylko. 'Weak chimeras in minimal networks of coupled phase oscillators'. In: *Chaos* 25.1 (Jan. 2015), p. 013106. ISSN: 1054-1500. DOI: 10.1063/1.4905197.

[8] O. V. Astakhov, S. V. Astakhov, N. S. Krakhovskaya, V. V. Astakhov and J. Kurths. 'The emergence of multistability and chaos in a two-mode van der Pol generator versus different connection types of linear oscillators'. In: *Chaos* 063118 (2018). ISSN: 1054-1500. DOI: 10.1063/1.5002609.

[9] N. M. Awal, D. Bullara and I. R. Epstein. 'The smallest chimera: Periodicity and chaos in a pair of coupled chemical oscillators'. In: *Chaos* 29.1 (2019). ISSN: 10541500. DOI: 10.1063/1.5060959.

[10] N. M. Awal and I. R. Epstein. 'Post-canard symmetry breaking and other exotic dynamic behaviors in identical coupled chemical oscillators'. In: *Physical Review E* 101.4 (2020). ISSN: 24700053. DOI: 10.1103/PhysRevE.101.042222.

[11] D. Battogtokh and J. J. Tyson. 'Turbulence near cyclic fold bifurcations in birhythmic media'. In: *Physical Review E* 70.2 (Aug. 2004), p. 026212. ISSN: 1539-3755. DOI: 10.1103/PhysRevE.70.026212.

[12] D. Baulch, J. F. Griffiths, A. J. Pappin and A. F. Sykes. 'Stationary-state and oscillatory combustion of hydrogen in a well-stirred flow reactor'. In: *Combustion and Flame* 73.2 (Aug. 1988), pp. 163–185. ISSN: 00102180. DOI: 10.1016/0010-2180(88)90044-2.

[13] M. Bennett, M. F. Schatz, H. Rockwood and K. Wiesenfeld. 'Huygens's clocks'. In: *Proceedings of the Royal Society of London. Series A: Mathematical, Physical and Engineering Sciences* 458.2019 (Mar. 2002), pp. 563–579. ISSN: 1364-5021. DOI: 10.1098/rspa.2001.0888.

[14] B. K. Bera, S. Majhi, D. Ghosh and M. Perc. 'Chimera states: Effects of different coupling topologies'. In: *EPL (Europhysics Letters)* 118.1 (Apr. 2017), p. 10001. ISSN: 0295-5075. DOI: 10.1209/0295-5075/118/10001.

[15] R. Berner, J. Fialkowski, D. Kasatkin, V. Nekorkin, S. Yanchuk and E. Schöll. 'Hierarchical frequency clusters in adaptive networks of phase oscillators'. In: *Chaos* 29.10 (Oct. 2019), p. 103134. ISSN: 1054-1500. DOI: 10.1063/1.5097835.

[16] R. Berner, E. Schöll and S. Yanchuk. 'Multiclusters in Networks of Adaptively Coupled Phase Oscillators'. In: *SIAM Journal on Applied Dynamical Systems* 18.4 (Jan. 2019), pp. 2227–2266. ISSN: 1536-0040. DOI: 10.1137/18M1210150.

[17] D. Biswas, T. Banerjee and J. Kurths. 'Control of birhythmicity through conjugate self-feedback: Theory and experiment'. In: *Physical Review E* 94.4 (2016), pp. 1–7. ISSN: 24700053. DOI: 10.1103/PhysRevE.94.042226.

[18] D. Biswas, T. Banerjee and J. Kurths. 'Control of birhythmicity: A self-feedback approach'. In: *Chaos* 27.6 (2017). ISSN: 10541500. DOI: 10.1063/1.4985561.

[19] D. J. Blackwood, A. M. Borazio, R. Greef, L. M. Peter and J. Stumper. 'Electrochemical and optical studies of silicon dissolution in ammonium fluoride solutions'. In: *Electrochimica Acta* 37.5 (1992), pp. 889–896. ISSN: 00134686. DOI: 10.1016/0013-4686(92)85040-R.

[20] M. I. Bolotov, L. Smirnov, G. Osipov and A. Pikovsky. 'Simple and complex chimera states in a nonlinearly coupled oscillatory medium'. In: *Chaos* 28.4 (Apr. 2018), p. 045101. ISSN: 1054-1500. DOI: 10.1063/1.5011678.

[21] J. Buck and E. Buck. 'Mechanism of Rhythmic Synchronous Flashing of Fireflies'. In: *Science* 159.3821 (Mar. 1968), pp. 1319–1327. ISSN: 0036-8075. DOI: 10.1126/science.159.3821.1319.

[22] S. Cattarin, I. Frateur, M. Musiani and B. Tribollet. 'Electrodissolution of p-Si in Acidic Fluoride Media Modeling of the Steady State'. In: *Journal of The Electrochemical Society* 147.9 (2000), p. 3277. ISSN: 00134651. DOI: 10.1149/1.1393895.

[23] J.-N. Chazalviel. 'Ionic processes through the interfacial oxide in the anodic dissolution of silicon'. In: *Electrochimica Acta* 37.5 (1992), pp. 865–875. ISSN: 00134686. DOI: 10.1016/0013-4686(92)85038-M.

[24] J.-N. Chazalviel, M. Etman and F. Ozanam. 'A voltammetric study of the anodic dissolution of p-Si in fluoride electrolytes'. In: *Journal of Electroanalytical Chemistry and Interfacial Electrochemistry* 297.2 (Jan. 1991), pp. 533–540. ISSN: 00220728. DOI: 10.1016/0022-0728(91)80049-V.

[25] J.-N. Chazalviel and F. Ozanam. 'A Theory for the Resonant Response of an Electrochemical System: Self-Oscillating Domains, Hidden Oscillation, and Synchronization Impedance'. In: *Journal of The Electrochemical Society* 139.9 (Sept. 1992), pp. 2501–2508. ISSN: 0013-4651. DOI: 10.1149/1.2221253.

[26] J.-N. Chazalviel, F. Ozanam, M. Etman, F. Paolucci, L. M. Peter and J. Stumper. 'The p-Si/fluoride interface in the anodic region: Damped and/or sustained oscillations'. In: *Journal of Electroanalytical Chemistry* 327.1-2 (1992), pp. 343–349. ISSN: 00220728. DOI: 10.1016/0022-0728(92)80160-6.

[27] R. Cheggou, A. Kadoun, N. Gabouze, F. Ozanam and J.-N. Chazalviel. 'Theoretical modelling of the I–V characteristics of p-type silicon in fluoride electrolyte in the first electropolishing plateau'. In: *Electrochimica Acta* 54.11 (Apr. 2009), pp. 3053–3058. ISSN: 00134686. DOI: 10.1016/j.electacta.2008.12.006.

[28] J. R. Chelikowsky and M. L. Cohen. 'Nonlocal pseudopotential calculations for the electronic structure of eleven diamond and zinc-blende semiconductors'. In: *Physical Review B* 14.2 (July 1976), pp. 556–582. ISSN: 01631829. DOI: 10.1103/PhysRevB.14.556.

[29] D. S. Cohen and J. P. Keener. 'Multiplicity and stability of oscillatory states in a continuous stirred tank reactor with exothermic consecutive reactions A $\rightarrow$ B $\rightarrow$ C'. In: *Chemical Engineering Science* 31.2 (1976), pp. 115–122. ISSN: 00092509. DOI: 10.1016/0009-2509(76)85046-4.

[30] Q. Dai, D. Liu, H. Cheng, H. Li and J. Yang. 'Two-frequency chimera state in a ring of nonlocally coupled Brusselators'. In: *PLOS ONE* 12.10 (Oct. 2017). Ed. by C. Zhou, e0187067. ISSN: 1932-6203. DOI: 10.1371/journal.pone.0187067.

[31] O. Decroly and A. Goldbeter. 'Birhythmicity, chaos, and other patterns of temporal self-organization in a multiply regulated biochemical system.' In: *Proceedings of the National Academy of Sciences* 79.22 (1982), pp. 6917–6921. ISSN: 0027-8424. DOI: 10.1073/pnas.79.22.6917.

[32] *DIN 38 409, part 15*. Berlin, 1987.

[33] M. Eddowes. 'Anodic dissolution of p- and n-type silicon: Kinetic study of the chemical mechanism'. In: *Journal of Electroanalytical Chemistry and Interfacial Electrochemistry* 280.2 (1990), pp. 297–311. ISSN: 00220728. DOI: 10.1016/0022-0728(90)87005-5.

[34] E. Foca, J. Carstensen and H. Föll. 'Modelling electrochemical current and potential oscillations at the Si electrode'. In: *Journal of Electroanalytical Chemistry* 603.2 (2007), pp. 175–202. ISSN: 00220728. DOI: 10.1016/j.jelechem.2007.01.019.

[35] H. Föll, M. Leisner, A. Cojocaru and J. Carstensen. 'Self-organization phenomena at semiconductor electrodes'. In: *Electrochimica Acta* 55.2 (2009), pp. 327–339. ISSN: 00134686. DOI: 10.1016/j.electacta.2009.03.076.

[36] D. Gabor. 'Theory of communication. Part 1: The analysis of information'. In: *Journal of the Institution of Electrical Engineers - Part III: Radio and Communication Engineering* 93.26 (Nov. 1946), pp. 429–441. ISSN: 2054-0604. DOI: 10.1049/ji-3-2.1946.0074.

[37] F. Gaspard, A. Bsiesy, M. Ligeon, F. Muller and R. Herino. 'Charge Exchange Mechanism Responsible for P-Type Silicon Dissolution during Porous Silicon Formation'. In: *Journal of The Electrochemical Society* 136.10 (1989), pp. 3043–3046. ISSN: 0013-4651. DOI: 10.1149/1.2096399.

[38] D. Golomb, D. Hansel and G. Mato. 'Chapter 21 Mechanisms of synchrony of neural activity in large networks'. In: *Handbook of biological physics*. Ed. by F. Moss and S. Gielen. Vol. 4. Elsevier, 2001, pp. 887–968. ISBN: 9780444502841. DOI: 10.1016/S1383-8121(01)80024-5.

[39] J. González-Avella, M. Cosenza and M. San Miguel. 'Localized coherence in two interacting populations of social agents'. In: *Physica A: Statistical Mechanics and its Applications* 399 (Apr. 2014), pp. 24–30. ISSN: 03784371. DOI: 10.1016/j.physa.2013.12.035.

[40] B. Gray and J. Jones. 'The heat release rates and cool flames of acetaldehyde oxidation in a continuously stirred tank reactor'. In: *Combustion and Flame* 57.1 (July 1984), pp. 3–14. ISSN: 00102180. DOI: 10.1016/0010-2180(84)90132-9.

[41] T. Gross and B. Blasius. 'Adaptive coevolutionary networks: a review'. In: *Journal of The Royal Society Interface* 5.20 (Mar. 2008), pp. 259–271. ISSN: 1742-5689. DOI: 10.1098/rsif.2007.1229.

[42] J. Grzanna, H. Jungblut and H. J. Lewerenz. 'A model for electrochemical oscillations at the Si | electrolyte contact: Part II. Simulations and experimental results'. In: *Journal of Electroanalytical Chemistry* 486.2 (May 2000), pp. 190–203. ISSN: 15726657. DOI: 10.1016/S0022-0728(00)00142-X.

[43] J. Guckenheimer and Y. Kuznetsov. 'Fold-Hopf bifurcation'. In: *Scholarpedia* 2.10 (2007), p. 1855. ISSN: 1941-6016. DOI: 10.4249/scholarpedia.1855.

[44] A. M. Hagerstrom, T. E. Murphy, R. Roy, P. Hövel, I. Omelchenko and E. Schöll. 'Experimental observation of chimeras in coupled-map lattices'. In: *Nature Physics* 8.9 (July 2012), pp. 658–661. ISSN: 1745-2473. DOI: 10.1038/nphys2372.

[45] H. Haken. *Advanced Synergetics*. Vol. 20. Springer Series in Synergetics 2. Berlin, Heidelberg: Springer Berlin Heidelberg, Feb. 1983, p. 209. ISBN: 978-3-642-45555-1. DOI: 10.1007/978-3-642-45553-7.

[46] J. D. Hart, K. Bansal, T. E. Murphy and R. Roy. 'Experimental observation of chimera and cluster states in a minimal globally coupled network'. In: *Chaos* 26.9 (2016). ISSN: 10541500. DOI: 10.1063/1.4953662.

[47] A. Heinrich. 'Mechanistische und dynamische Eigenschaften der Elektrodissolution von Silizium'. Master's thesis. Technische Universität München, 2013.

[48] J. Hounsgaard, H. Hultborn, B. Jespersen and O. Kiehn. 'Bistability of alpha-motoneurones in the decerebrate cat and in the acute spinal cat after intravenous 5-hydroxytryptophan.' In: *The Journal of Physiology* 405.1 (Nov. 1988), pp. 345–367. ISSN: 00223751. DOI: 10.1113/jphysiol.1988.sp017336.

[49] R. Hueck. 'From Subcritical to Strong Nonlinear Spatial Coupling during Electrodissolution of n-type Si : Phase Waves , Frequency Clusters and Tristability'. Master's Thesis. Technische Universität München, 2017.

[50] H. Jahnsen and R. Llinás. 'Ionic basis for the electro-responsiveness and oscillatory properties of guinea-pig thalamic neurones in vitro.' In: *The Journal of Physiology* 349.1 (Apr. 1984), pp. 227–247. ISSN: 00223751. DOI: 10.1113/jphysiol.1984.sp015154.

[51] B. R. Johnson, J. F. Griffiths and S. K. Scott. 'Characterisation of oscillations in the H2+ O2reaction in a continuous-flow reactor'. In: *Journal of the Chemical Society, Faraday Transactions* 87.4 (1991), pp. 523–533. ISSN: 09565000. DOI: 10.1039/FT9918700523.

[52] J. S. Judge. 'A study of the dissolution of SiO2 in acidic fluoride solutions'. In: *Journal of The Electrochemical Society* 118.11 (1971), pp. 1772–1775. ISSN: 00134651. DOI: 10.1149/1.2407835.

[53] M. Kang, D. Momotenko, A. Page, D. Perry and P. R. Unwin. 'Frontiers in Nanoscale Electrochemical Imaging: Faster, Multifunctional, and Ultrasensitive'. In: *Langmuir* 32.32 (2016), pp. 7993–8008. ISSN: 15205827. DOI: 10.1021/acs.langmuir.6b01932.

[54] D. V. Kasatkin, S. Yanchuk, E. Schöll and V. I. Nekorkin. 'Self-organized emergence of multilayer structure and chimera states in dynamical networks with adaptive couplings'. In: *Physical Review E* 96.6 (Dec. 2017), p. 062211. ISSN: 2470-0045. DOI: 10.1103/PhysRevE.96.062211.

[55] F. P. Kemeth, S. W. Haugland and K. Krischer. 'Symmetries of Chimera States'. In: *Physical Review Letters* 120.21 (May 2018), p. 214101. ISSN: 0031-9007. DOI: 10.1103/PhysRevLett.120.214101.

[56] M. Komarov and A. Pikovsky. 'Finite-size-induced transitions to synchrony in oscillator ensembles with nonlinear global coupling'. In: *Physical Review E* 92.2 (Aug. 2015), p. 020901. ISSN: 1539-3755. DOI: 10.1103/PhysRevE.92.020901.

[57] A. Koseska, E. Volkov and J. Kurths. 'Oscillation quenching mechanisms: Amplitude vs. oscillation death'. In: *Physics Reports* 531.4 (2013), pp. 173–199. ISSN: 03701573. DOI: 10.1016/j.physrep.2013.06.001.

[58] D. Koster, G. Du, A. Battistel and F. La Mantia. 'Dynamic impedance spectroscopy using dynamic multi-frequency analysis: A theoretical and experimental investigation'. In: *Electrochimica Acta* 246 (2017), pp. 553–563. ISSN: 0013-4686. DOI: 10.1016/J.ELECTACTA.2017.06.060.

[59] C. J. Krebs. *Ecology; the Experimental Analysis of Distribution and Abundance*. Second Pri. New York, NY: Harper & Row, 1972, p. 694. ISBN: 060437707.

[60] K. Krischer. 'Principles of Temporal and Spatial Pattern Formation in Electrochemical Systems'. In: *Modern Aspects of Electrochemistry*. Ed. by B. E. et al Conway. Vol. 213. Part_2. Boston: Kluwer Academic Publishers, 1999. Chap. 1, pp. 1–142. DOI: 10.1007/0-306-46916-2_1.

[61] K. Krischer. 'Nonlinear Dynamics in Electrochemical Systems'. In: *Advances in Electrochemical Science and Engineering, Volume 8*. Vol. 8. Weinheim, FRG: Wiley-VCH Verlag GmbH & Co. KGaA, 2003, pp. 89–208. ISBN: 3527302115. DOI: 10.1002/3527600787.ch2.

[62] Y. Kuramoto and T. Tsuzuki. 'On the Formation of Dissipative Structures in Reaction-Diffusion Systems: Reductive Perturbation Approach'. In: *Progress of Theoretical Physics* 54.3 (Sept. 1975), pp. 687–699. ISSN: 0033-068X. DOI: 10.1143/PTP.54.687.

[63] Y. Kuramoto. *Chemical Oscillations, Waves, and Turbulence*. Vol. 19. Springer Series in Synergetics. Berlin, Heidelberg: Springer Berlin Heidelberg, 1984. ISBN: 978-3-642-69691-6. DOI: 10.1007/978-3-642-69689-3.

[64] Y. Kuramoto. 'Self-entrainment of a population of coupled nonlinear oscillators'. In: *International Symposium on Mathematical Problems in Theoretical Physics*. 02. Berlin/Heidelberg: Springer-Verlag, 2004, pp. 420–422. DOI: 10.1007/BFb0013365.

[65] Y. Kuramoto and D. Battogtokh. 'Coexistence of Coherence and Incoherence in Nonlocally Coupled Phase Oscillators'. In: *Nonlinear Phenom. Complex Syst.* 5 (2002), pp. 380–385.

[66] P. Lamba and J. L. Hudson. 'Experimental Evidence of Multiple Oscillatory States in a Continuous Reactor'. In: *Chemical Engineering Communications* 32.6 (Jan. 1985), pp. 369–375. ISSN: 0098-6445. DOI: 10.1080/00986448508911657.

[67] H. A. Lechner, D. A. Baxter, J. W. Clark and J. H. Byrne. 'Bistability and its regulation by serotonin in the endogenously bursting neuron R15 in Aplysia'. In: *Journal of Neurophysiology* 75.2 (1996), pp. 957–962. ISSN: 00223077. DOI: 10.1152/jn.1996.75.2.957.

[68] V. Lehmann. 'The Physics of Macropore Formation in Low Doped n-Type Silicon'. In: *Journal of The Electrochemical Society* 140.10 (1993), p. 2836. ISSN: 00134651. DOI: 10.1149/1.2220919.

[69] V. Lehmann and H. Föll. 'Formation Mechanism and Properties of Electrochemically Etched Trenches in n-Type Silicon'. In: *Journal of The Electrochemical Society* 137.2 (Feb. 1990), pp. 653–659. ISSN: 0013-4651. DOI: 10.1149/1.2086525.

[70] H. J. Lewerenz. 'Spatial and temporal oscillation at Si (111) electrodes in aqueous fluoride-containing solution'. In: *The Journal of Physical Chemistry B* 5647.111 (1997), pp. 2421–2425. ISSN: 1520-6106. DOI: 10.1021/jp962694x.

[71] H. J. Lewerenz. 'Operational principles of electrochemical nanoemitter solar cells for photovoltaic and photoelectrocatalytic applications'. In: *Journal of Electroanalytical Chemistry* 662.1 (Nov. 2011), pp. 184–195. ISSN: 15726657. DOI: 10.1016/j.jelechem.2011.05.019.

[72] H. J. Lewerenz, J. Stumper and L. M. Peter. 'Deconvolution of charge injection steps in quantum yield multiplication on silicon'. In: *Physical Review Letters* 61.17 (Oct. 1988), pp. 1989–1992. ISSN: 00319007. DOI: 10.1103/PhysRevLett.61.1989.

[73] A. L. Lin, M. Bertram, K. Martinez, H. L. Swinney, A. Ardelea and G. F. Carey. 'Resonant Phase Patterns in a Reaction-Diffusion System'. In: *Physical Review Letters* 84.18 (May 2000), pp. 4240–4243. ISSN: 0031-9007. DOI: 10.1103/PhysRevLett.84.4240.

[74] A. L. Lin, A. Hagberg, E. Meron and H. L. Swinney. 'Resonance tongues and patterns in periodically forced reaction-diffusion systems'. In: *Physical Review E* 69.6 (June 2004), p. 066217. ISSN: 1539-3755. DOI: 10.1103/PhysRevE.69.066217.

[75] Y.-P. Lin and J.-G. Hwu. 'Suboxide characteristics in ultrathin oxides grown under novel oxidation processes'. In: *Journal of Vacuum Science & Technology A: Vacuum, Surfaces, and Films* 22.6 (Nov. 2004), pp. 2265–2272. ISSN: 0734-2101. DOI: 10.1116/1.1795824.

[76] E. N. Lorenz. 'Deterministic Nonperiodic Flow'. In: *Journal of the Atmospheric Sciences* 20.2 (Mar. 1963), pp. 130–141. ISSN: 0022-4928. DOI: 10.1175/1520-0469(1963)020<0130:DNF>2.0.CO;2.

[77] E. N. Lorenz. *The Essence of Chaos*. 1st ed. Seattle: University of Washington Press, 1995, p. 227. ISBN: 0295975148.

[78] K. Lüdge and H. G. Schuster. *Nonlinear Laser Dynamics*. Ed. by K. Lüdge. Weinheim, Germany: Wiley-VCH Verlag GmbH & Co. KGaA, Dec. 2011. ISBN: 9783527639823. DOI: 10.1002/9783527639823.

[79] E. A. Martens, S. Thutupalli, A. Fourriere and O. Hallatschek. 'Chimera states in mechanical oscillator networks'. In: *Proceedings of the National Academy of Sciences* 110.26 (June 2013), pp. 10563–10567. ISSN: 0027-8424. DOI: 10.1073/pnas.1302880110.

[80] J. Maselko and H. L. Swinney. 'Complex periodic oscillations and Farey arithmetic in the Belousov–Zhabotinskii reaction'. In: *The Journal of Chemical Physics* 85.11 (Dec. 1986), pp. 6430–6441. ISSN: 0021-9606. DOI: 10.1063/1.451473.

[81] MATLAB:2019b. *9.7.0.1586710 (R2019b)*. Natick, Massachusetts: The MathWorks Inc., 2019.

[82] R. M. May. 'Simple mathematical models with very complicated dynamics'. In: *Nature* 261.5560 (June 1976), pp. 459–467. ISSN: 0028-0836. DOI: 10.1038/261459a0.

[83] R. M. May and G. F. Oster. 'Bifurcations and Dynamic Complexity in Simple Ecological Models'. In: *The American Naturalist* 110.974 (July 1976), pp. 573–599. ISSN: 0003-0147. DOI: 10.1086/283092.

[84] R. Memming and G. Schwandt. 'Anodic dissolution of silicon in hydrofluoric acid solutions'. In: *Surface Science* 4.2 (Mar. 1966), pp. 109–124. ISSN: 00396028. DOI: 10.1016/0039-6028(66)90071-9.

[85] K. O. Menzel, O. Arp and A. Piel. 'Spatial Frequency Clustering in Nonlinear Dust-Density Waves'. In: *Physical Review Letters* 104.23 (June 2010), p. 235002. ISSN: 0031-9007. DOI: 10.1103/PhysRevLett.104.235002.

[86] I. Miethe. 'Spatio-temporal pattern formation during the anodic electrodissolution of silicon in ammonium fluoride solution'. PhD Thesis. Technische Universität München, 2010.

[87] I. Miethe, V. García-Morales and K. Krischer. 'Irregular Subharmonic Cluster Patterns in an Autonomous Photoelectrochemical Oscillator'. In: *Physical Review Letters* 102.19 (May 2009), p. 194101. ISSN: 0031-9007. DOI: 10.1103/PhysRevLett.102.194101.

[88] I. Miethe and K. Krischer. 'Ellipsomicroscopic studies of the anodic oxidation of p-type silicon in fluoride containing electrolytes during current oscillations'. In: *Journal of Electroanalytical Chemistry* 666 (Feb. 2012), pp. 1–10. ISSN: 15726657. DOI: 10.1016/j.jelechem.2011.11.027.

[89] A. S. Mikhailov. *Foundations of Synergetics I*. Vol. 51. Springer Series in Synergetics. Berlin, Heidelberg: Springer Berlin Heidelberg, 1994. ISBN: 978-3-642-78558-0. DOI: 10.1007/978-3-642-78556-6.

[90] A. S. Mikhailov, D. H. Zanette, Y. M. Zhai, I. Z. Kiss and J. L. Hudson. 'Cooperative action of coherent groups in broadly heterogeneous populations of interacting chemical oscillators'. In: *Proceedings of the National Academy of Sciences* 101.30 (July 2004), pp. 10890–10894. ISSN: 0027-8424. DOI: 10.1073/pnas.0402899101.

[91] M. Mikhaylenko, L. Ramlow, S. Jalan and A. Zakharova. 'Weak multiplexing in neural networks: Switching between chimera and solitary states'. In: *Chaos* 29.2 (Feb. 2019), p. 023122. ISSN: 1054-1500. DOI: 10.1063/1.5057418.

[92] A. E. Motter, S. A. Myers, M. Anghel and T. Nishikawa. 'Spontaneous synchrony in power-grid networks'. In: *Nature Physics* 9.3 (Mar. 2013), pp. 191–197. ISSN: 1745-2473. DOI: 10.1038/nphys2535.

[93] B. P. Nadappuram, K. McKelvey, R. Al Botros, A. W. Colburn and P. R. Unwin. 'Fabrication and Characterization of Dual Function Nanoscale pH-Scanning Ion Conductance Microscopy (SICM) Probes for High Resolution pH Mapping'. In: *Analytical Chemistry* 85.17 (Sept. 2013), pp. 8070–8074. ISSN: 0003-2700. DOI: 10.1021/ac401883n.

[94] T. Nagy, E. Verner, V. Gáspár, H. Kori and I. Z. Kiss. 'Delayed feedback induced multirhythmicity in the oscillatory electrodissolution of copper'. In: *Chaos* 25.6 (2015). ISSN: 10541500. DOI: 10.1063/1.4921694.

[95] O. Nast, S. Rauscher, H. Jungblut and H. J. Lewerenz. 'Micromorphology changes of silicon oxide on Si(111) during current oscillations: A comparative in situ AFM and FTIR study'. In: *Journal of Electroanalytical Chemistry* 442.1-2 (1998), pp. 169–174. ISSN: 15726657. DOI: 10.1016/S0022-0728(97)00476-2.

[96] S. Nkomo, M. R. Tinsley and K. Showalter. 'Chimera and chimera-like states in populations of nonlocally coupled homogeneous and heterogeneous chemical oscillators'. In: *Chaos* 26.9 (Sept. 2016), pp. 662–665. ISSN: 10541500. DOI: 10.1063/1.4962631.

[97] A. M. Nobili. 'Secular effects of tidal friction on the planet-satellite systems of the solar system'. In: *The Moon and the Planets* 18.2 (Apr. 1978), pp. 203–216. ISSN: 0165-0807. DOI: 10.1007/BF00896743.

[98] K. Okuda. 'Variety and generality of clustering in globally coupled oscillators'. In: *Physica D: Nonlinear Phenomena* 63.3-4 (Mar. 1993), pp. 424–436. ISSN: 01672789. DOI: 10.1016/0167-2789(93)90121-G.

[99] O. E. Omel'chenko. 'The mathematics behind chimera states'. In: *Nonlinearity* 31.5 (May 2018), R121–R164. ISSN: 0951-7715. DOI: 10.1088/1361-6544/aaaa07.

[100] O. E. Omel'chenko, Y. L. Maistrenko and P. A. Tass. 'Chimera States: The Natural Link Between Coherence and Incoherence'. In: *Physical Review Letters* 100.4 (Jan. 2008), p. 044105. ISSN: 0031-9007. DOI: 10.1103/PhysRevLett.100.044105.

[101] G. V. Osipov and M. M. Sushchik. 'Synchronized clusters and multistability in arrays of oscillators with different natural frequencies'. In: *Physical Review E* 58.6 (Dec. 1998), pp. 7198–7207. ISSN: 1063-651X. DOI: 10.1103/PhysRevE.58.7198.

[102] G. V. Osipov, A. S. Pikovsky, M. G. Rosenblum and J. Kurths. 'Phase synchronization effects in a lattice of nonidentical Rössler oscillators'. In: *Physical Review E* 55.3 (Mar. 1997), pp. 2353–2361. ISSN: 1063-651X. DOI: 10.1103/PhysRevE.55.2353.

[103] M. J. Panaggio and D. M. Abrams. 'Chimera states: coexistence of coherence and incoherence in networks of coupled oscillators'. In: *Nonlinearity* 28.3 (2015), R67–R87. ISSN: 0951-7715. DOI: 10.1088/0951-7715/28/3/R67.

[104] J. Pantaleone. 'Synchronization of metronomes'. In: *American Journal of Physics* 70.10 (Oct. 2002), pp. 992–1000. ISSN: 0002-9505. DOI: 10.1119/1.1501118.

[105] F. Paolucci, L. M. Peter and J. Stumper. 'Wavelength-dependent photocurrent multiplication during the anodic dissolution of n-Si in ammonium fluoride solutions'. In: *Journal of Electroanalytical Chemistry* 341.1-2 (1992), pp. 165–180. ISSN: 00220728. DOI: 10.1016/0022-0728(92)80482-J.

[106] M. Patzauer. 'Multistability in the Oscillatory Electrodissolution of Silicon'. Master's Thesis. Technische Universität München, 2016.

[107] M. Patzauer, R. Hueck, A. Tosolini, K. Schönleber and K. Krischer. 'Autonomous Oscillations and Pattern Formation with Zero External Resistance during Silicon Electrodissolution'. In: *Electrochimica Acta* 246 (Aug. 2017), pp. 315–321. ISSN: 00134686. DOI: 10.1016/j.electacta.2017.06.005.

[108] M. Patzauer and K. Krischer. 'Self-Organized Multifrequency Clusters in an Oscillating Electrochemical System with Strong Nonlinear Coupling'. In: *Physical Review Letters* 126.19 (May 2021), p. 194101. ISSN: 0031-9007. DOI: 10.1103/PhysRevLett.126.194101.

[109] J. S. Pendergast, K. D. Niswender and S. Yamazaki. 'The complex relationship between the light-entrainable and methamphetamine-sensitive circadian oscillators: evidence from behavioral studies of Period -mutant mice'. In: *European Journal of Neuroscience* 38.7 (July 2013), pp. 3044–3053. ISSN: 0953816X. DOI: 10.1111/ejn.12309.

[110] H. R. Philipp and H. Ehrenreich. 'Optical Properties of Semiconductors'. In: *Physical Review* 129.4 (Feb. 1963), pp. 1550–1560. ISSN: 0031-899X. DOI: 10.1103/PhysRev.129.1550.

[111] A. Pikovsky, M. Rosenblum and J. Kurths. *Synchronization*. Cambridge University Press, Oct. 2001. ISBN: 9780521533522. DOI: 10.1017/CBO9780511755743.

[112] A. N. Pisarchik and U. Feudel. 'Control of multistability'. In: *Physics Reports* 540.4 (July 2014), pp. 167–218. ISSN: 03701573. DOI: 10.1016/j.physrep.2014.02.007.

[113] J. Proost, F. Blaffart, S. Turner and H. Idrissi. 'On the Origin of Damped Electrochemical Oscillations at Silicon Anodes (Revisited)'. In: *ChemPhysChem* 15.14 (Oct. 2014), pp. 3116–3124. ISSN: 14397641. DOI: 10.1002/cphc.201402207.

[114] A. Provata. 'Chimera states formed via a two-level synchronization mechanism'. In: *Journal of Physics: Complexity* 1.2 (July 2020), p. 025006. ISSN: 2632-072X. DOI: 10.1088/2632-072X/ab79bd.

[115] Q. Ren and J. Zhao. 'Adaptive coupling and enhanced synchronization in coupled phase oscillators'. In: *Physical Review E* 76.1 (July 2007), p. 016207. ISSN: 1539-3755. DOI: 10.1103/PhysRevE.76.016207.

[116] M. Rosenblum and A. Pikovsky. 'Self-Organized Quasiperiodicity in Oscillator Ensembles with Global Nonlinear Coupling'. In: *Physical Review Letters* 98.6 (Feb. 2007), p. 064101. ISSN: 0031-9007. DOI: 10.1103/PhysRevLett.98.064101.

[117] A. Rothkegel and K. Lehnertz. 'Irregular macroscopic dynamics due to chimera states in small-world networks of pulse-coupled oscillators'. In: *New Journal of Physics* 16 (2014). ISSN: 13672630. DOI: 10.1088/1367-2630/16/5/055006.

[118] J.-C. Roux. 'Experimental studies of bifurcations leading to chaos in the Belousof-Zhabotinsky reaction'. In: *Physica D: Nonlinear Phenomena* 7.1-3 (May 1983), pp. 57–68. ISSN: 01672789. DOI: 10.1016/0167-2789(83)90115-X.

[119] M. M. Salman. 'Modeling Complex Phenomena in Open Electrochemical Systems'. PhD thesis. Technische Universität München, 2020.

[120] M. M. Salman, M. Patzauer, D. Koster, F. La Mantia and K. Krischer. 'Electro-oxidation of p-silicon in fluoride-containing electrolyte: a physical model for the regime of negative differential resistance'. In: *The European Physical Journal Special Topics* 227.18 (Apr. 2019), pp. 2641–2658. ISSN: 1951-6355. DOI: 10.1140/epjst/e2019-800118-x.

[121] G. Saxena, A. Prasad and R. Ramaswamy. 'Amplitude death: The emergence of stationarity in coupled nonlinear systems'. In: *Physics Reports* 521.5 (2012), pp. 205–228. ISSN: 03701573. DOI: 10.1016/j.physrep.2012.09.003.

[122] L. Schmidt and K. Krischer. 'Chimeras in globally coupled oscillatory systems: From ensembles of oscillators to spatially continuous media'. In: *Chaos* 25.6 (June 2015), p. 064401. ISSN: 10541500. DOI: 10.1063/1.4921727.

[123] L. Schmidt and K. Krischer. 'Clustering as a Prerequisite for Chimera States in Globally Coupled Systems'. In: *Physical Review Letters* 114.3 (Jan. 2015), p. 034101. ISSN: 0031-9007. DOI: 10.1103/PhysRevLett.114.034101.

[124] L. Schmidt, K. Schönleber, V. García-Morales and K. Krischer. 'Unusual synchronization phenomena during electrodissolution of silicon: the role of nonlinear global coupling'. In: *Engineering of Chemical Complexity II* 12 (May 2014), pp. 239–260. DOI: 10.1142/9789814616133_0014.

[125] L. Schmidt, K. Schönleber, K. Krischer and V. García-Morales. 'Coexistence of synchrony and incoherence in oscillatory media under nonlinear global coupling'. In: *Chaos* 24.1 (Mar. 2014), p. 013102. ISSN: 1054-1500. DOI: 10.1063/1.4858996.

[126] E. Schöll. 'Synchronization patterns and chimera states in complex networks: Interplay of topology and dynamics'. In: *European Physical Journal: Special Topics* 225.6-7 (2016), pp. 891–919. ISSN: 19516401. DOI: 10.1140/epjst/e2016-02646-3.

[127] K. Schönleber. 'Self-organization phenomena during the electrodissolution of silicon'. PhD Thesis. Technische Universität München, 2015.

[128] K. Schönleber and K. Krischer. 'High-Amplitude versus Low-Amplitude Current Oscillations during the Anodic Oxidation of p-Type Silicon in Fluoride Containing Electrolytes'. In: *ChemPhysChem* 13.12 (Aug. 2012), pp. 2989–2996. ISSN: 14394235. DOI: 10.1002/cphc.201200230.

[129] K. Schönleber, M. Patzauer and K. Krischer. 'A comparison of modeling frameworks for the oscillatory silicon electrodissolution'. In: *Electrochimica Acta* 210 (Aug. 2016), pp. 346–351. ISSN: 00134686. DOI: 10.1016/j.electacta.2016.05.144.

[130] K. Schönleber, C. Zensen, A. Heinrich and K. Krischer. 'Pattern formation during the oscillatory photoelectrodissolution of n-type silicon: turbulence, clusters and chimeras'. In: *New Journal of Physics* 16.6 (June 2014), p. 063024. ISSN: 1367-2630. DOI: 10.1088/1367-2630/16/6/063024.

[131] A. G. Smart. 'Exotic chimera dynamics glimpsed in experiments'. In: *Physics Today* 65.10 (Oct. 2012), pp. 17–19. ISSN: 0031-9228. DOI: 10.1063/PT.3.1738.

[132] K. Srinivasan and G. A. Rechnitz. 'Activity Measurements with a Fluoride-Selective Membrane Electrode'. In: *Analytical Chemistry* 40.3 (1968), pp. 509–512. ISSN: 15206882. DOI: 10.1021/ac60259a039.

[133] M. Stich, M. Ipsen and A. S. Mikhailov. 'Self-organized stable pacemakers near the onset of birhythmicity'. In: *Physical Review Letters* 86.19 (2001), pp. 4406–4409. ISSN: 00319007. DOI: 10.1103/PhysRevLett.86.4406.

[134] M. Stich, M. Ipsen and A. S. Mikhailov. 'Self-organized pacemakers in birhythmic media'. In: *Physica D: Nonlinear Phenomena* 171.1-2 (2002), pp. 19–40. ISSN: 01672789. DOI: 10.1016/S0167-2789(02)00549-3.

[135] S. H. Strogatz. 'From Kuramoto to Crawford: exploring the onset of synchronization in populations of coupled oscillators'. In: *Physica D: Nonlinear Phenomena* 143.1-4 (2000), pp. 1–20. ISSN: 01672789. DOI: 10.1016/S0167-2789(00)00094-4.

[136] S. H. Strogatz. *Sync: How order emerges from chaos in the universe, nature, and daily life*. 1 st ed. New York, NY: Hyperion, 2003, p. 338. ISBN: 0-7868-6844-9.

[137] S. H. Strogatz. *Nonlinear Dynamics and Chaos*. Boulder, CO: Westview Press, 2015, p. 513. ISBN: 978-0-81334910-7.

[138] S. H. Strogatz, D. M. Abrams, A. McRobie, B. Eckhardt and E. Ott. 'Crowd synchrony on the Millennium Bridge'. In: *Nature* 438.7064 (Nov. 2005), pp. 43–44. ISSN: 0028-0836. DOI: 10.1038/438043a.

[139] J. Stumper, R. Greef and L. M. Peter. 'Current Oscillations during Anodic-Dissolution of P-Si in Ammonium Fluoride - an Investigation Using Ring Disk Voltammetry and Ellipsometry'. In: *Journal of Electroanalytical Chemistry* 310.1-2 (1991), pp. 445–452. ISSN: 00220728. DOI: 10.1016/0022-0728(91)85281-S.

[140] J. Stumper and L. M. Peter. 'A rotating ring-disc study of the photodissolution of n-Si in ammonium fluoride solutions'. In: *Journal of Electroanalytical Chemistry and Interfacial Electrochemistry* 309.1-2 (July 1991), pp. 325–331. ISSN: 00220728. DOI: 10.1016/0022-0728(91)87024-X.

[141] Y. Suda and K. Okuda. 'Emergence of second coherent regions for breathing chimera states'. In: *Physical Review E* 101.6 (June 2020), p. 062203. ISSN: 2470-0045. DOI: 10.1103/PhysRevE.101.062203.

[142] A. A. Temirbayev, Y. D. Nalibayev, Z. Z. Zhanabaev, V. I. Ponomarenko and M. Rosenblum. 'Autonomous and forced dynamics of oscillator ensembles with global nonlinear coupling: An experimental study'. In: *Physical Review E* 87.6 (June 2013), p. 062917. ISSN: 1539-3755. DOI: 10.1103/PhysRevE.87.062917.

[143] A. A. Temirbayev, Z. Z. Zhanabaev, S. B. Tarasov, V. I. Ponomarenko and M. Rosenblum. 'Experiments on oscillator ensembles with global nonlinear coupling'. In: *Physical Review E - Statistical, Nonlinear, and Soft Matter Physics* 85.1 (2012), pp. 1–4. ISSN: 15393755. DOI: 10.1103/PhysRevE.85.015204.

[144] M. R. Tinsley, S. Nkomo and K. Showalter. 'Chimera and phase-cluster states in populations of coupled chemical oscillators'. In: *Nature Physics* 8.9 (July 2012), pp. 662–665. ISSN: 10541500. DOI: 10.1063/1.4962631.

[145] E. Tognoli and J. A. Kelso. 'The Metastable Brain'. In: *Neuron* 81.1 (2014), pp. 35–48. ISSN: 08966273. DOI: 10.1016/j.neuron.2013.12.022.

[146] A. Tosolini. 'Characterization of Multiple Bifurcation Scenarios during the Electrodissolution of p-Type Si in Fluoride Containing Electrolytes'. Master's Thesis. Technische Universität München, 2017.

[147] A. Tosolini, M. Patzauer and K. Krischer. 'Bichaoticity induced by inherent birhythmicity during the oscillatory electrodissolution of silicon'. In: *Chaos* 29.4 (Apr. 2019), p. 043127. ISSN: 1054-1500. DOI: 10.1063/1.5090118.

[148] D. R. Turner. 'Electropolishing Silicon in Hydrofluoric Acid Solutions'. In: *Journal of The Electrochemical Society* 105.7 (1958), p. 402. ISSN: 00134651. DOI: 10.1149/1.2428873.

[149] A. Uhlir. 'Electrolytic Shaping of Germanium and Silicon'. In: *Bell System Technical Journal* 35.2 (1956), pp. 333–347. ISSN: 15387305. DOI: 10.1002/j.1538-7305.1956.tb02385.x.

[150] M. Wickramasinghe and I. Z. Kiss. 'Spatially Organized Dynamical States in Chemical Oscillator Networks: Synchronization, Dynamical Differentiation, and Chimera Patterns'. In: *PLoS ONE* 8.11 (Nov. 2013). Ed. by B. Ermentrout, e80586. ISSN: 1932-6203. DOI: 10.1371/journal.pone.0080586.

[151] M. Wickramasinghe and I. Z. Kiss. 'Spatially organized partial synchronization through the chimera mechanism in a network of electrochemical reactions'. In: *Phys. Chem. Chem. Phys.* 16.34 (2014), pp. 18360–18369. ISSN: 1463-9076. DOI: 10.1039/C4CP02249A.

[152] J. Wiehl. 'Birhythmicity and Intrinsic Entrainment in a Diffusively Coupled Oscillatory System: An Experimental Study'. Master's Thesis. Technische Universität München, 2020.

[153] J. C. Wiehl, M. Patzauer and K. Krischer. 'Birhythmicity, intrinsic entrainment, and minimal chimeras in an electrochemical experiment'. In: *Chaos* 31.9 (Sept. 2021), p. 091102. ISSN: 1054-1500. DOI: 10.1063/5.0064266.

[154] K. Wiesenfeld, P. Colet and S. H. Strogatz. 'Frequency locking in Josephson arrays: Connection with the Kuramoto model'. In: *Physical Review E* 57.2 (Feb. 1998), pp. 1563–1569. ISSN: 1063-651X. DOI: 10.1103/PhysRevE.57.1563.

[155] J. Wojewoda, K. Czolczynski, Y. Maistrenko and T. Kapitaniak. 'The smallest chimera state for coupled pendula'. In: *Scientific Reports* 6.1 (Dec. 2016), p. 34329. ISSN: 2045-2322. DOI: 10.1038/srep34329.

[156] R. Yamapi, G. Filatrella and M. A. Aziz-Alaoui. 'Global stability analysis of birhythmicity in a self-sustained oscillator'. In: *Chaos* 20.1 (2010). ISSN: 10541500. DOI: 10.1063/1.3309014.

[157] A. Yeldesbay, A. Pikovsky and M. Rosenblum. 'Chimeralike States in an Ensemble of Globally Coupled Oscillators'. In: *Physical Review Letters* 112.14 (Apr. 2014), p. 144103. ISSN: 0031-9007. DOI: 10.1103/PhysRevLett.112.144103.

[158] M. Yukiteru. 'Controlling Patterns with a Spatial Light Modulator during Si Electrodissolution'. Master's Thesis. Technische Universität München, 2021.

[159] C. Zensen. 'Mechanism of Oscillation and Spatio-temporal Pattern Formation in a Semiconductor Electrochemical System'. Master's Thesis. Technische Universität München, 2013.

[160] X. G. Zhang. *Electrochemistry of Silicon and Its Oxide*. Boston: Kluwer Academic Publishers, 2004, p. 510. ISBN: 0-306-46541-8. DOI: 10.1007/b100331.

[161] J. Zimmermann. 'Plasmonic Catalysis of the Electrochemical Reduction of Carbon Dioxide on Gold Nanostructures through the Excitation of Molecular Vibration Modes'. Master's Thesis. Technische Universität München, 2017.